Phases and vacancy defects in methylammonium lead iodide perovskite : an ab initio study

Kajal Madaan

▶ To cite this version:

Kajal Madaan. Phases and vacancy defects in methylammonium lead iodide perovskite : an ab initio study. Materials Science [cond-mat.mtrl-sci]. Université Paris-Saclay, 2023. English. NNT : 2023UPASP183 . tel-04622577

HAL Id: tel-04622577
https://theses.hal.science/tel-04622577

Submitted on 24 Jun 2024

Phases and vacancy defects in methylammonium lead iodide perovskite : an ab initio study

Étude ab initio des phases et des défauts lacunaires dans la pérovskite hybride MAPbI$_3$

Thèse de doctorat de l'université Paris-Saclay

École doctorale n° 564 Physique en Ile-de-France (PIF)
Spécialité de doctorat : Physique
Graduate School : Physique
Référent : Faculté des sciences d'Orsay

Thèse préparée dans le **Service de recherche en Corrosion et Comportement des Matériaux** (Université Paris-Saclay, CEA), sous la direction de **Guido ROMA**, Directeur de recherche (CEA Paris-Saclay - SRMP), et la co-direction de **Pascal POCHET**, Directeur de recherche (CEA Grenoble - L_SIM)

Thèse soutenue à Paris-Saclay, le 12 décembre 2023, par

Kajal MADAAN

Composition du jury

Membres du jury avec voix délibérative

Marie-France BARTHE Directeur de recherche, CEMHTI, Université d'Orléans, France	Présidente
Flyura DJURABEKOVA Professeure, Departement of Physics, University of Helsinki, Finland	Rapporteure & Examinatrice
Mikaël KEPENEKIAN Chargé de recherche (HDR), Institut des Sciences Chimiques de Rennes,Université de Rennes, France	Rapporteur & Examinateur
Marjorie BERTOLUS Directeur de recherche, CEA Cadarache, Saint-Paul-lez-Durance, France	Examinatrice
Michele AMATO Maître de conférences, Laboratoire de Physique des Solides, Université Paris-Saclay, France	Examinateur

THESE DE DOCTORAT

NNT : 2020UPASAP183

ÉCOLE DOCTORALE
Physique en
Île-de-France (PIF)

Titre : Étude ab initio des phases et des défauts lacunaires dans la pérovskite hybride $MAPbI_3$

Mots clés : pérovskites halogénées, ab initio, défauts, photovoltaîque, annihilation de positons

Résumé : Le iodure de méthylammonium et de plomb ou, en abrégé, MAPbI3 est un matériau très prometteur dans le domaine des dispositifs photovoltaïques de la prochaine génération. Cela est dû à ses niveaux d'efficacité remarquables dépassant 22% et à son processus de fabrication peu coûteux. Néanmoins, des nombreuses recherches visent à améliorer les performances, la stabilité et de prévenir les processus de dégradation du matériaux en cours de fonctionnement. Pour atteindre ces objectifs, il est impératif de comprendre en profondeur la structure du matériau au niveau atomique et ses transformations de phase. En outre, à des températures élevées, supérieures à 300 K, l'augmentation soudaine de la concentration de défauts lors de la transition du matériau de la phase tétragonale à la phase cubique contribue potentiellement au processus de dégradation mentionnés précédemment.

Des études récentes sur la structure à haute température du MAPbI3 ont introduit le concept de "polymorphisme". Elles révèlent la présence de différents motifs structurels dans le $MAPbI_3$ qui ne peuvent être décrits que dans le cadre de la structure cristalline communément admise pour la phase cubique, ce qui rend nécessaire l'inclusion d'un certain dégré de désordre, introduit par des distorsions aléatoires dans une maille élémentaire de presque 400 atomes. Dans cette étude DFT computationnelle, à l'aide d'une nouvelle approche basée sur l'analyse des liaisons hydrogène, nous avons pu obtenir une phase cubique, que nous appelons pseudo-tétragonal-3D. Il est remarquable que ce système présente un niveau d'énergie inférieur d'environ 100 meV à celui de son homologue "monomorphe", même en l'absence de distorsions aléatoires et dont la maille élémentaire est de seulement 4 unités de formule (48 atomes). En outre, nous utilisons diverses techniques analytiques, notamment l'analyse de la fonction de distribution des paires et les diagrammes de densité de charge, pour caractériser ce système cubique. Nous avons aussi identifié une autre structure tétragonale qui respecte les critères du schéma de liaison des autres polymorphes tétragonaux déjà connus. En utilisant des calculs CI-NEB, nous prévoyons une barrière d'énergie d'activation exceptionnellement basse de 44 meV pour la transformation de cubique à tétragonal. Cette information est importante car la transition se produit à la température de fonctionnement du dispositif photovoltaïque.

Des études antérieures ont montré que pendant la transformation de phase de tétragonal à cubique, la densité de défauts dans le matériau augmente. Bien que la densité des défauts ait été déterminée expérimentalement, l'identification microscopique de ces défauts reste une question ouverte. Dans notre étude, nous relevons ce défi en utilisant la spectroscopie d'annihilation de positrons comme un outil puissant pour faire la lumière sur la nature précise de ces défauts. Le second volet de cette thèse est donc dédié à la simulation des temps de vie des positons dans le matériau en présence ou non de défauts lacunaires. La comparaison entre les temps de vie calculés avec quelques résultats expérimentaux disponibles en littérature, ainsi qu'une analyse de la densité du positon dans le matériau, sont ici présentées. Ces résultats permettent d'affiner la caractérisation des défauts lacunaires, en vue d'une prochaine comparaison avec des nouveaux résultats expérimentaux.

université
PARIS-SACLAY

ÉCOLE DOCTORALE
Physique en
Île-de-France (PIF)

Title : Phases and vacancy defects in methylammonium lead iodide perovskite : an ab initio study

Keywords : halide perovskites, ab initio, defects, photovoltaic, positron annihilation

Abstract : Methyl Ammonium Lead Iodide or in short, MAPbI3 has emerged as a promising frontier in the realm of next-generation photovoltaic devices. This is because of its remarkable efficiency levels exceeding 22% and facile fabrication processes. Nonetheless, the pursuit of enhanced performance, stability, and the prevention of material degradation during operation is currently in progress. To achieve these objectives, a profound understanding of the material's atomic-level structure and its phase transformations is imperative. Moreover, at elevated temperatures above 300 K, the sudden rise of defects as the material transitions from tetragonal to cubic phase potentially contributes to the reported degradation.

Recent investigations on the high temperature structure of MAPbI3 have delved into the concept of 'polymorphism'. They reveal the presence of different structural motifs in $MAPbI_3$ that can only be realized in larger than minimal supercells of 32 formula units (384 atoms) after applying a random distortion. In this computational DFT study, we present a novel approach based on the hydrogen bonding scheme, demonstrating the feasibility of creating a cubic system, which we term the pseudo-tetragonal-3D system. Remarkably, this system exhibits an energy level approximately 100 meV lower than the 'monomorphous' counterpart, even in the absence of random distortions and 4 formula units (48 atoms) unit cell. Furthermore, we employ various analytical techniques, including pair-distribution function analysis and charge density plots, to validate this cubic system. We have also identified another tetragonal structure that meets the bonding scheme criteria of other known tetragonal polymorphs. Employing CI-NEB calculations, we predict a low activation energy barrier of 44 meV for the cubic to tetragonal transformation. This is important because this transition occurs at the operating temperature of the photovoltaic device.

Furthermore, previous studies have shown that during phase transformation from tetragonal to cubic, the defect density within the material increases. Although experimental determination of defect density has been achieved, the microscopic identification of these defects remains an open question. In our investigation, we tackle this challenge utilizing positron annihilation spectroscopy as a powerful tool to shed light on the precise nature of these defects. The second part of this thesis is therefore dedicated to the simulation of positron lifetimes in the material in the presence or absence of vacancy defects. We present the comparison between the calculated lifetimes and some experimental results available in the literature, as well as an analysis of the positron density in the material. These results are used to refine the characterisation of vacancy defects, with a view to a future comparison with new experimental results.

To my parents

Résumé étendu en français

Cette thèse contribue à l'évolution globale vers l'énergie durable en se plongeant dans le domaine de la recherche sur les énergies renouvelables, en se concentrant spécifiquement sur l'analyse computationnelle des matériaux pérovskites pour la production d'énergie solaire. L'étude est centrée sur la pérovskite hybride iodure de plomb et de méthyl ammonium, $\mathrm{CH_3NH_3PbI_3}$ ou, en abrégé, $\mathrm{MAPbI_3}$, choisie pour ses caractéristiques favorables, notamment une faible énergie de liaison des excitons, une mobilité élevée des porteurs de charge, une grande longueur de diffusion des excitons, une tolérance aux défauts et une fabrication rentable. Les matériaux basés sur $\mathrm{MAPbI_3}$ sont très prometteurs dans le domaine des dispositifs photovoltaïques de la prochaine génération, avec des niveaux d'efficacité dépassant 22 %. Bien que ces matériaux présentent des caractéristiques prometteuses, leur stabilité reste une préoccupation urgente qui nécessite des recherches plus approfondies avant qu'ils ne soient commercialisés.

Les facteurs extrinsèques contribuant à la dégradation, tels que l'exposition à l'oxygène, à l'eau et à la lumière, sont signalés dans la littérature existante. Des stratégies visant à contrôler ces mécanismes extrinsèques de dégradation, telles que l'encapsulation, ont été explorées. Cependant, les limites intrinsèques de stabilité, y compris les transformations de phase et la dégradation induite par les défauts, constituent également des obstacles importants. Ils sont donc abordés dans cette thèse sous la forme de deux chapitres distincts.

Pour cette étude de simulation numérique, la théorie de la fonctionnelle de la densité (DFT), telle qu'elle est mise en œuvre dans Quantum Espresso, sert de cadre fondamental pour tous les calculs.

Tout d'abord, la DFT est abordée au chapitre 2, ainsi que les méthodes et approximations utilisées. Ceci permet d'expliquer le choix de la fonctionnelle d'échange-corrélation OptB86-vdw, bien connue pour sa prise en compte des interactions de van der Waals. La section suivante présente les fondements théoriques du calcul de la durée de vie des positons dans le matériau avant son annihilation, en tenant compte des aspects théoriques et de la mise en oeuvre des simulations. Elle comprend une discussion approfondie sur le traitement des structures électroniques et atomiques concernant les électrons et les positons. En outre, le chapitre aborde les principes fondamentaux de l'analyse structurelle, en utilisant les concepts des notations de Glazer et des fonctions de distribution des paires. L'application de la méthode de la bande élastique (NEB) est expliquée, en particulier pour étudier le mécanisme d'une transformations entre deux phases choisies de MAPbI$_3$. En outre, diverses facettes de la thermodynamique et de la caractérisation des défauts sont expliquées, notamment le diagramme stabilité thermodynamique, l'énergie de formation des défauts et le volume de Voronoï.

Le chapitre 3 se concentre sur les transformations structurelles de la pérovskite MAPbI$_3$, car elles sont mal comprises. Pour ce faire, il faut d'abord essayer de comprendre la structure et le schéma de liaison des différentes phases de MAPbI$_3$ au niveau atomique. On sait que MAPbI$_3$ existe en trois phases : Orthorhombique, Tétragonale et Cubique, par ordre croissant de température. Nous montrons que ces phases diffèrent non seulement par leurs notations de glazer, qui ne s'appliquent qu'à la cage inorganique, mais aussi par leur schéma de liaison hydrogène. La molécule organique dans la phase cubique est connue pour être en rotation continue en raison de la température élevée, donc il n'y a pas de schéma de liaison hydrogène particulier qui est suivi [1]. La phase tétragonale présente un schéma de liaison unique avec deux H$_N$ (on indique ainsi les hydrogènes liés à l'azote dans la molécule) se connectant uniquement à l'iode présent dans la couche MAI. Cela est vrai pour tous les polymorphes tétragonaux, qui sont proches en énergie avec une gamme d'énergie de seulement 6 meV. Au contraire, dans la phase orthorhombique, il existe un schéma de liaison hydrogène en trois dimensions. La liaison hydrogène s'établit entre les H$_N$ et les iodes présents dans la couche MAI et la couche PbI$_2$.

Des études récentes sur la structure à haute température du MAPbI$_3$ ont approfondi le concept de "polymorphisme". Elles révèlent la présence de différents motifs structurels dans le MAPbI$_3$ qui ne peuvent être réalisés que dans des supercellules contenant au moins 32 unités de formule (384 atomes) après application d'une distorsion aléatoire [2]. Ce système polymorphe est reproduit et analysé dans cette thèse. Nous expliquons ainsi l'observation de joints de mâcle dans la phase tétragonale lors du refroidissement du système MAPbI$_3$ à partir de la phase cubique.

En tenant compte du concept de polymorphisme et en gardant à l'esprit l'analyse du schéma de liaison hydrogène, nous introduisons deux nouveaux systèmes. Ces deux systèmes sont : le système pseudo-tétragonal-3D et une nouvelle forme tétragonale. Le système pseudo-tétragonal-3D présente une maille élémentaire de symétrie très proche de celle d'un système cubique avec un écart par rapport au cubique parfait de $\sim$ 2%; le réseau de liaisons hydrogène est tridimensionnel et sa fonction de distribution de paires correspond assez bien à la fonction de distribution de paires obtenue expérimentalement pour le système MAPbI$_3$ à haute température. Le nouveau système tétragonal est conçu conformément au système pseudo-cubique-3D, à l'exception de l'orientation de la molécule organique. Cette dernière a subi une rotation autour de son propre axe pour atteindre le nouveau système tétragonal, qui présente les caractéristiques d'un polymorphe tétragonal avec une liaison hydrogène bidimensionnelle entre H$_N$ et I dans la couche MAI. Cela permet d'éviter la rotation de l'axe moléculaire organique lui-même, qui donne une énergie d'activation plus élevée selon les tests NEB. Ainsi, avec ces deux systèmes représentant les systèmes cubique et tétragonale, notre calcul NEB donne une faible énergie d'activation de $\sim$ 44 meV. Dans ce chapitre nous présentons également un résumé des minima principaux du paysage énergétique, contenant toutes les structures calculées, ce qui suggère la nature vitreuse du paysage d'énergie potentielle.

En outre, des études antérieures ont montré que, pendant la transformation de phase de tétragonal à cubique, la densité de défauts dans le matériau augmente[3]. Bien que la détermination expérimentale de la densité des défauts ait été réalisée[4, 5], l'identification microscopique de ces défauts reste une question ouverte. Dans notre étude, nous relevons ce défi en utilisant la spectroscopie d'annihilation de positons comme un outil puissant pour éclaircir la nature précise de ces défauts. Le chapitre 4 de cette thèse est donc consacré à la simulation des temps de vie des positons dans le matériau en présence ou en l'absence de défauts lacunaires. Tout d'abord, des calculs d'énergie de formation de défauts (DFE) sont effectués dans le système pseudo-tétragonal-3D et dans les différents polymorphes de la forme tétragonale ayant une seule lacune V$_{MA}^{-}$ ou V$_{Pb}^{-2}$. Les tracés de l'énergie de formation dans les systèmes tétragonaux montrent une énergie de formation plus faible pour V$_{Pb}^{-2}$ dans des conditions intermédiaires de potentiel chimique de Pb.

Pour les calculs de temps de vie des positons, la DFT à deux composantes est utilisée. Les deux composantes sont le positron et l'électron. La densité électronique est d'abord calculée soit à l'aide de Quantum Espresso, qui le fait de manière autoconsistante, soit du logiciel ATSUP, qui utilise la superposition des densités atomiques. La densité de positons est supposée proche de zéro, afin d'éviter toute interférence avec la densité d'électrons (limite de faible densité de positons). Le temps de vie est une fonction monotone de l'inverse de la densité électronique. Des tests sont effectués sur le polymorphe tétragonal le plus stable pour vérifier la sensibilité du temps de vie au changement du paramètre α, un paramètre ajustable prenant pour contrôler l'interaction d'échange et corrélation électron-positron. Une valeur de 0,22 pour le paramètre α est choisie pour les calculs de la PAL sur les systèmes avec ou sans défauts.

Ainsi, pour les phases vierges de MAPbI$_3$, on observe que le temps de vie augmente avec l'accroissement du volume de la phase. Un graphique de la variation du temps de vie avec le volume de Voronoï est présenté avec des défauts lacunaires V$_{MA}^{-}$, V$_{Pb}^{-2}$, V$_{H}^{-}$, V$_{N}^{0}$ et V$_{C}^{0}$. Ces PAL dans les systèmes défectueux sont, comme prévu, légèrement plus élevés que dans le système vierge. Alors que cette augmentation est modeste pour le Pb, on observe une durée de vie très importante pour la défaut lacunaire du méthylammonium.

Nous comparons ensuite les temps de vie calculés et certains résultats expérimentaux disponibles dans la littérature et nous analysons la densité de positons dans le matériau. Ces résultats sont utilisés pour affiner la caractérisation des défauts lacunaires, en vue d'une comparaison future avec de nouveaux résultats expérimentaux.

En somme, cette thèse permet d'avancer dans la compréhension des phases et des défauts de la pérovskite MAPbI$_3$, contribuant ainsi au développement d'une énergie solaire durable. Les connaissances acquises constituent une base pour les recherches futures visant à améliorer la stabilité et la performance des dispositifs photovoltaïques basés sur ces matériaux.

Dans le contexte des perspectives futures, l'application de la dynamique moléculaire à l'aide de potentiels générés par l'apprentissage machine serait cruciale. Cette approche ouvrirait la voie à une modélisation plus précise des comportements complexes des pérovskites, permettant ainsi une meilleure compréhension de leur stabilité à long terme et des mécanismes de dégradation potentiels. Parallèlement, une autre perspective clé pourrait résider dans la simulation du Doppler broadening des positrons dans des matériaux pérovskites présentant des défauts lacunaires, offrant ainsi une compréhension de la densité de défauts à l'échelle microscopique. Cette approche, qui utiliserait la densité fonctionnelle à deux composantes, pourrait permettre d'analyser les variations du temps de vie des positons en présence de différents types de défauts. Ces résultats pourraient fournir des informations cruciales pour la caractérisation des défauts lacunaires, contribuant ainsi à la compréhension fondamentale des transformations de phase et de la stabilité des pérovskites.

REFERENCES

[1] Dominik J Kubicki, Daniel Prochowicz, Albert Hofstetter, Peter Pechy, Shaik M Zakeeruddin, Michael Gratzel, and Lyndon Emsley. Cation dynamics in mixed-cation MA$_x$FA$_{1-x}$PbI$_3$ hybrid perovskites from solid-state nmr. *Journal of the American Chemical Society*, 139(29):10055–10061, 2017. pages ii

[2] Xin-Gang Zhao, Gustavo M Dalpian, Zhi Wang, and Alex Zunger. Polymorphous nature of cubic halide perovskites. *Physical Review B*, 101(15):155137, 2020. pages iii

[3] Joydeep Dhar, Sayantan Sil, Arka Dey, Partha Pratim Ray, and Dirtha Sanyal. Positron annihilation spectroscopic investigation on the origin of temperature-dependent electrical response in methylammonium lead iodide perovskite. *The Journal of Physical Chemistry Letters*, 8(8):1745–1751, 2017. pages iii

[4] Daniele Meggiolaro, Silvia G Motti, Edoardo Mosconi, Alex J Barker, James Ball, Carlo Andrea Riccardo Perini, Felix Deschler, Annamaria Petrozza, and Filippo De Angelis. Iodine chemistry determines the defect tolerance of lead-halide perovskites. *Energy & Environmental Science*, 11(3):702–713, 2018. pages iii

[5] Valerio Adinolfi, Mingjian Yuan, Riccardo Comin, Emmanuel S Thibau, Dong Shi, Makhsud I Saidaminov, Pongsakorn Kanjanaboos, Damir Kopilovic, Sjoerd Hoogland, Zheng-Hong Lu, et al. The in-gap electronic state spectrum of methylammonium lead iodide single-crystal perovskites. *Advanced materials*, 28(17):3406–3410, 2016. pages iii

Acknowledgements

This manuscript is the conclusion of a three-year PhD thesis at the French Alternative Energies and Atomic Energy Commission (CEA). I am grateful to Le Commissariat à l'énergie atomique et aux énergies alternatives (CEA) for allowing me to carry out this project in the best conditions.

I would like to extend my sincerest gratitude to all those who have supported and assisted me during my PhD journey. First and foremost, I would like to express my sincere gratitute to my supervisors, Dr. Guido Roma and Dr. Pascal Pochet, who deserve special recognition for providing their complementary expertise, patient support, and valuable feedback at every stage that led to the completion of this thesis. Regular weekly meetings with them created a system for me to manage my goal of attaining a PhD, despite the difficulties of covid in the initial days. Their meticulous attention to detail and methodical approach have greatly contributed to the success of our project. Their guidance was instrumental in shaping my research and I am forever grateful to them.

Over the course of my PhD, I had the opportunity to work in two departments of CEA: one physically and the other primarily remotely. Having an office at SRMP, I received support and encouragement from all the people in the lab, permanent and non-permanent, during the challenging times of my research. I had Guido here, whose door I could knock anytime for any problem. I have received tremendous support and assistance from my colleagues: Dr. Yunho, Guilhem, Anruo, Dr. Savneet, Dr. Océane, Dr. Martin, Dr. Charbel, Dr. Daphné, Gabrielle and all others. Special thanks to Dr. Jean-Luc, head of the lab, for always treating me as a member of his lab, even though I was officially dependent on the IRIG department. Despite being at SRMP, I was always connected to people in Grenoble, especially Pascal in our weekly online-meetings and on slack. I also had insightful scientific exchanges with Sameer and Samuel, who were at a similar stage in their thesis. I thank them for providing me moral support throughout my journey.

I am also thankful to the ANR project TRAPPER for their financial support, as well as the collaboration and contribution of all the scientists I worked with during my PhD. I thank the ANR project members Dr. Catherine Corbel, Dr. Marie-France Barthe, Dr. Bernard Geoffroy, and others for sharing their experimental expertise. I thank my Ph.D. committee members: Dr. Fabien Bruneval and Dr. Frédéric Oswald for their constructive feedbacks during the annual meetings. I would like to extend my sincere thanks also to Dr. Ilja Makkonen for helping me with the ATSUP software.

I am deeply grateful to my thesis committee members: Pr. Flyura Djurabekova, Dr. Mikaël Kepenekian, Dr. Marie-France Barthe, Dr. Marjorie Bertolus and Dr. Michele Amato for their invaluable time and effort in reviewing my work and providing constructive feedback. Their suggestions have helped me to improve the quality of my research and I thank them for their contribution.

I would like to extend my gratitute to my Master's project supervisor, Dr. T.J. Dhilip Kumar, as well as my teachers at IIT Ropar, Dr. Manoj Kumar Pandey and Dr. Sudipta Sinha, for igniting my passion in this field of science.

I would also like to thank the non-scientific people who were there for me. My parents (Rakesh and Anju Madaan) and sister Payal, have been my source of unwavering support and love. I am forever thankful for their wise counsel and encouragement. Next, my life in Paris would not have been the same without my dear friends (Dr. Harshit, Dr. Arshjot, Vaishnavi, Aravind) and I am grateful for their constant support. Finally, I would like to thank Harkamal for always inspiring me to be my best self. Thank you for being by my side.

Contents

List of Tables

List of Figures

Chapter 1

Introduction

> Energy cannot be created or destroyed; it can only be changed from one form to another.
>
> Albert Einstein

In the 21st century, the ramifications of global warming have become increasingly evident. This alarming shift in climate patterns has galvanized humanity towards a collective commitment to forging a sustainable future. Amid this pressing need for action, the transition to cleaner sources of energy has emerged as the most practical solution to mitigate our carbon footprint on our planet. This thesis is dedicated to making a modest but valuable contribution to the ongoing research in the realm of renewable energy, focusing specifically on perovskites materials for generation of solar power. By exploring and advancing our understanding of this material, we aim to accelerate the transition to a more sustainable and environmentally friendly energy production.

1.1 Alternative sources of energy

According to the law of conservation of energy, a fundamental principle in physics, energy can neither be created not be destroyed; instead, it can only be changed from one form to another. This principle has had a profound impact on our world, especially in the context of energy production and its consequences.

Historically, our reliance on conventional fossil fuels such as coal and natural gas for electricity generation and meeting our energy needs stemmed from the conversion of their stored energy into electricity. However, this practice came at a considerable cost, contributing significantly to global warming and its associated adverse effects on our planet's climate. [1, 2, 3]

As a result, humans are now making a significant shift towards more sustainable and environmentally friendly production of energy. This shift is being driven by the imperative to mitigate the detrimental impacts of conventional energy sources and address the degradation of our environment. Various innovative methods are being employed to transform energy from conventional to unconventional sources, each with its unique benefits. These alternative energy sources encompass a diverse array of methods, including the use of hydrogen, biogas, wind, thermal, hydro, solar and more [4, 5, 6, 7, 8]. These unconventional methods play a pivotal role in our transition towards alternative and renewable energy sources. These diverse methods not only offer a more sustainable and eco-friendly means of satisfying our energy demands but also represent a vital step in mitigating the environmental challenges posed by conventional fossil fuels. [9, 10, 11, 8, 10, 6, 7, 12]

The increasing demand for and supply of renewable energy sources are substantiated by data from the International Energy Agency (IEA), which illustrates the growth in renewable energy installations over the past few years [13]. According to the figure, the data reveals a significant shift: from a mere 203 GW of added renewable energy capacity between 2002 and 2007, there was a substantial surge to 1288 GW between 2017 and 2022.

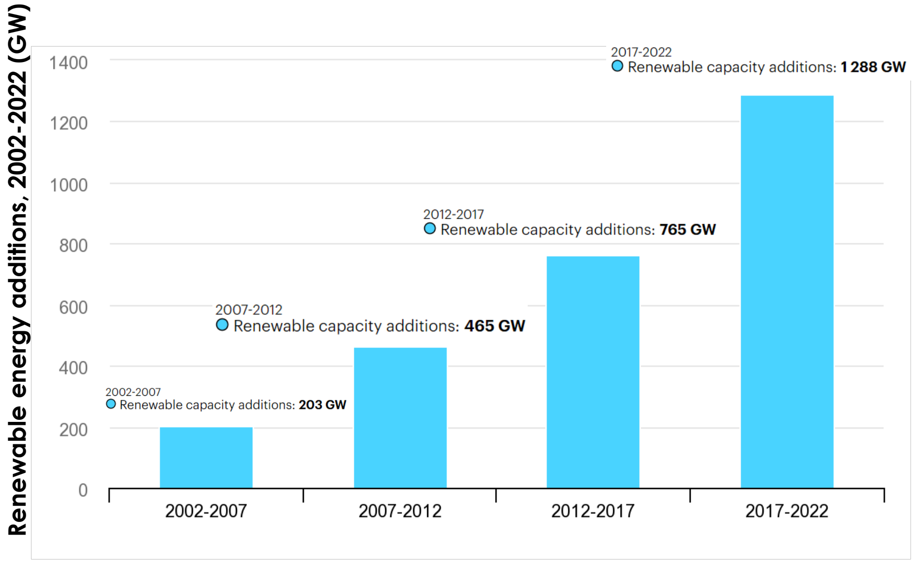

Figure 1.1: A bar chart for the renewable energy additions over the years 2002-2022. The data is taken from [13].

The transition to renewable energy sources is further underscored by the pie charts provided in Figure 1.2. These charts offer a comparative analysis of global energy supply in 1973 and 2019. As the global energy demand has expanded, there has been a noticeable shift away from non-renewable sources such as coal, oil, and natural gas in order to meet the increasing energy needs with alternative, renewable sources. There has been a notable rise in the contribution of renewable energy sources, including nuclear, hydro, as well as other emerging sources like solar and wind power.

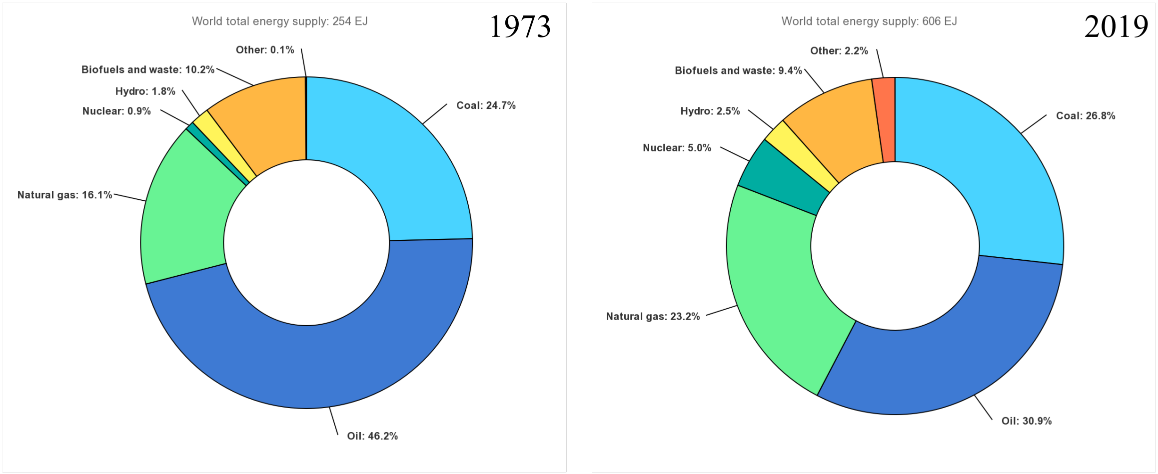

Figure 1.2: Comparison of the total energy supply in the world in the years 1973 (left) and 2019 (right) with pie charts. The data is taken from [14] and [15].

According to the "Renewables 2022" report by the International Energy Agency (IEA), renewable energy sources are on track to emerge as the predominant source of global electricity generation, surpassing coal by early 2025 [16]. Furthermore, the solar energy sector individually is expected to surpass that of coal by 2027 for electricity production by 2027. The year-wise changing trend in the electricity production and the projections for the future trends are given in Figure 1.3.

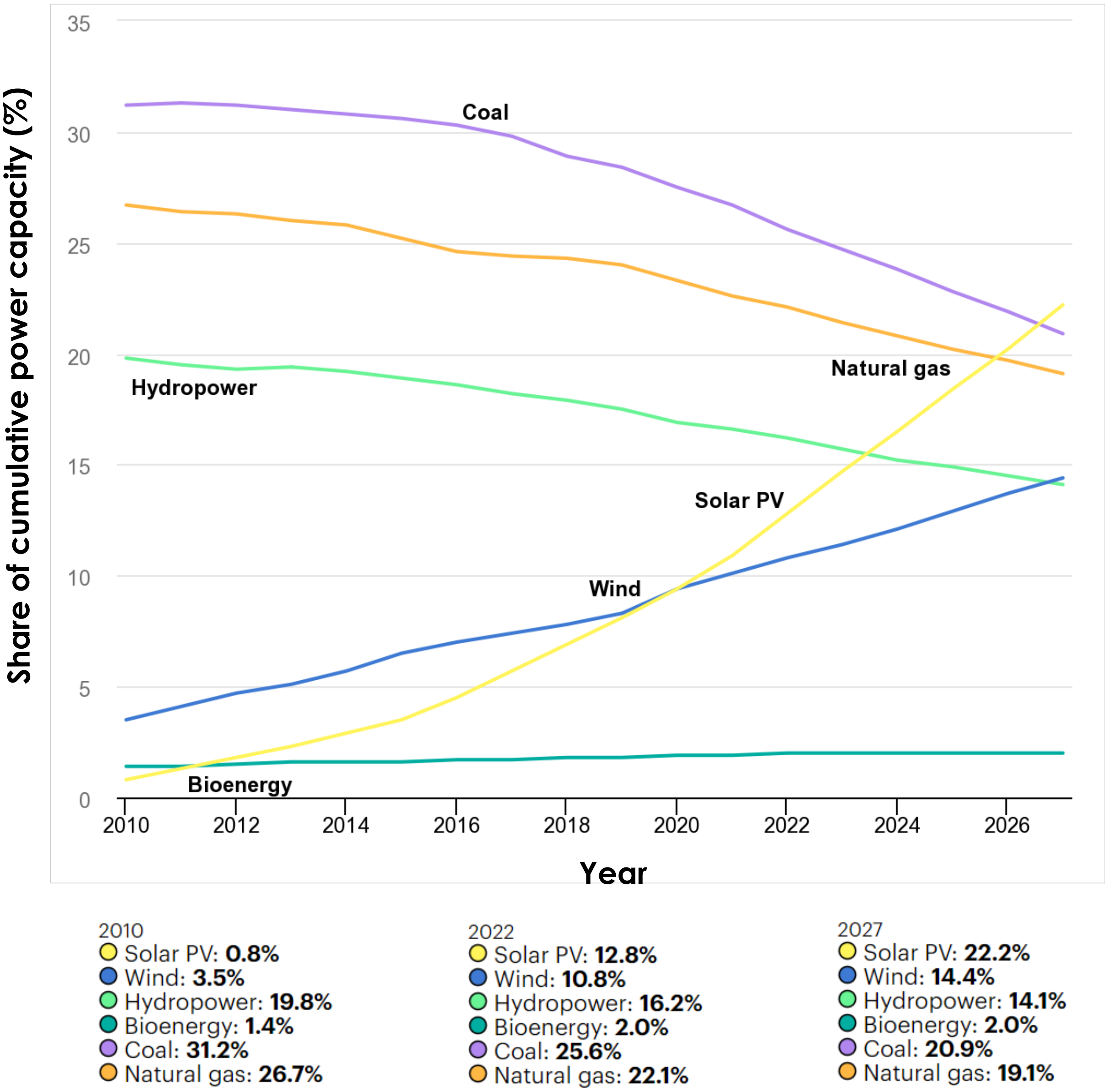

Figure 1.3: Plot for the percentage of cumulative power capacity of different energy sectors in the world with real data between 2010 to 2022. The projections for the upcoming years upto 2026 are shown. The data is taken from [16].

The projections in Figure 1.3 are based on the data collected for previous years. These trends are given in Figure 1.4. An increase in the net renewable capacity additions are reported for all the sectors: mainly wind, solar and hydro energy sectors. Of particular significance is the remarkable surge in net renewable capacity additions within the photovoltaic (PV) sector, surpassing other sectors by a considerable margin. In the year 2022, PV accounted for a staggering two-thirds of all renewable electricity technologies. This remarkable dominance can be attributed to its favorable cost-effectiveness, impressive performance metrics, and widespread accessibility.

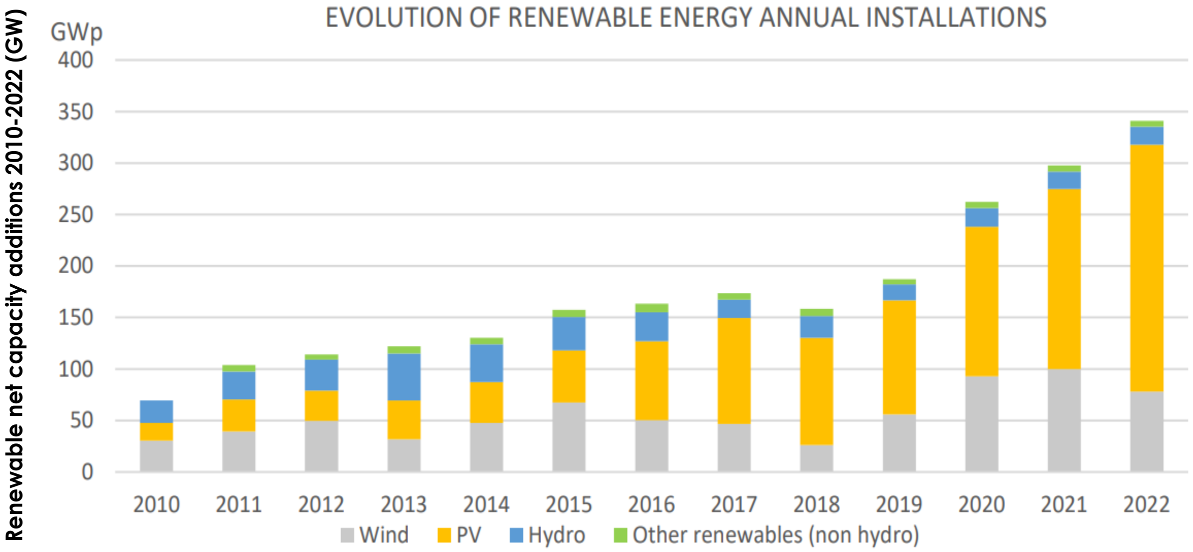

Figure 1.4: The addition to the world's renewable net capacity for the years between 2010 to 2022. The data is taken from [17].

1.2 The photovoltaic world

The sun serves as the ultimate source of energy, providing an astonishing amount of power to earth every day. Approximately 17,300 terawatts (TW) of energy radiates onto the Earth's surface from the Sun [18]. Solar photovoltaic systems help in harnessing this abundant energy source effectively. This technology allows us to capture and convert solar energy into electricity and heat for various applications, including electricity generation, heating, and cooling. Solar power has gained increasing significance as a sustainable and environmentally friendly energy solution [11].

The evolution of the renewable energy sector is reported in Figure 1.4. To focus specifically on the solar segment, the global solar capacity and the annual additions are reported in the Figure 1.5. The plot shows the growth of the solar energy sector in the world with the latest installations of 243 GW added in 2022 alone, which is 61 GW greater than those added in 2021 [19] [17]. This milestone achievement catapulted the solar industry past the 1 TW mark. It represented two-thirds of all the new renewable electricity added in 2022 because of the consistent costs, technical performance and accessibility, and generally faster permitting procedures than wind or hydro. Furthermore, in 2022, solar energy played a pivotal role in global electricity generation, contributing approximately 12.8% of the world's total electricity output [16] [20].

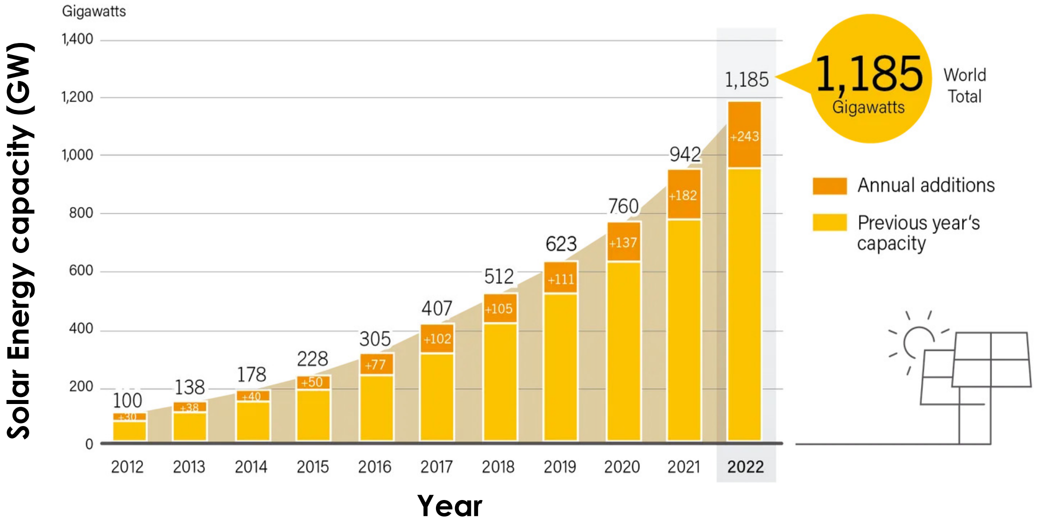

Figure 1.5: Plot for evolution of the global capacity of solar PV and its annual additions for each year between 2012 and 2022. The plot highlights the bright future of solar PV sector. The data is taken from [19] and [17].

1.2.1 Powering the Future: Solar Energy Materials

Since the advent of solar cell technology for energy production, a multitude of materials have been developed and continue to evolve for use in solar cell applications. These materials are at the forefront of the renewable energy revolution, driving innovations in photovoltaic technology. Solar cell materials can be broadly categorized into three generations:

First generation:

- This category includes Monocrystalline and Polycrystalline Silicon. They can have moderate to high efficiencies. But, they are brittle and crack under bending stress. Also, they are expensive materials. Currently, approximately 95% of the solar cells in the current photovoltaic market are made of Silicon [21].

Second generation:

- These include thin-film technologies like CIGS and CdTe, and amorphous Si. Though they are flexible and low-cost, they have lower efficiencies than first generation solar cells [22].

Third generation:

- The 3rd generation of solar cell materials represents the latest frontiers in photovoltaic technology and includes materials that have shown exceptional potential for high efficiency. These include perovskites, dye-sensitized solar cells, organic photovoltaics and more. They are generally easy to manufacture, low-cost and flexible without compromising on the efficiency of the photovoltaic system [23].

A comparison of these three different generations of solar cell materials is presented in Figure 1.6.

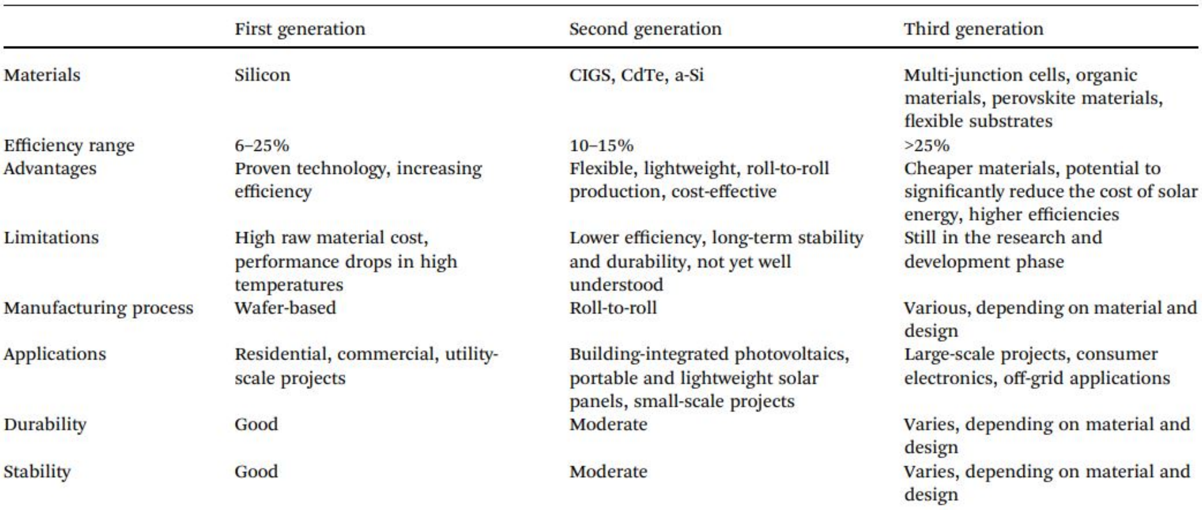

	First generation	Second generation	Third generation
Materials	Silicon	CIGS, CdTe, a-Si	Multi-junction cells, organic materials, perovskite materials, flexible substrates
Efficiency range	6–25%	10–15%	>25%
Advantages	Proven technology, increasing efficiency	Flexible, lightweight, roll-to-roll production, cost-effective	Cheaper materials, potential to significantly reduce the cost of solar energy, higher efficiencies
Limitations	High raw material cost, performance drops in high temperatures	Lower efficiency, long-term stability and durability, not yet well understood	Still in the research and development phase
Manufacturing process	Wafer-based	Roll-to-roll	Various, depending on material and design
Applications	Residential, commercial, utility-scale projects	Building-integrated photovoltaics, portable and lightweight solar panels, small-scale projects	Large-scale projects, consumer electronics, off-grid applications
Durability	Good	Moderate	Varies, depending on material and design
Stability	Good	Moderate	Varies, depending on material and design

Figure 1.6: Comparison between the first, the second, and the third-generation of solar cell materials. The image is taken from [23].

The most recent data on the efficiencies of perovskite solar cells, as reported by the National Renewable Energy Laboratory (NREL) are depicted in Figure 1.7. The chart reveals a remarkable trend for the increase in efficiencies for all the solar cell materials. Notably, just over the past decade, perovskite solar cells have witnessed a substantial increase in efficiency, surpassing the rate of progress that silicon solar cells achieved over the course of nearly five decades. This development underscores the rapid advancements in perovskite technology, making it a front-runner in the field of renewable energy.

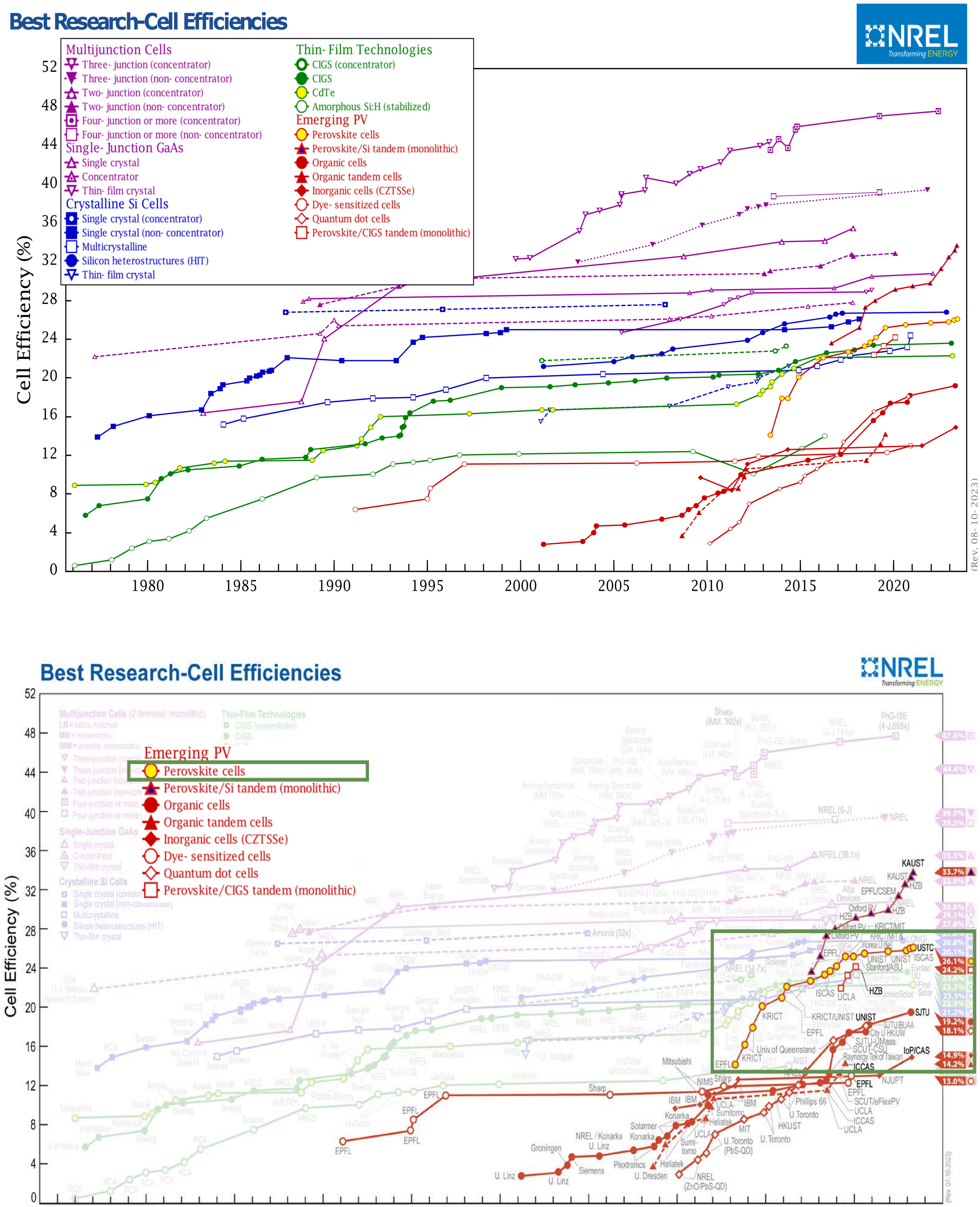

Figure 1.7: Above: A chart displaying the record research cell efficiencies for crystalline silicon cells, single-junction gallium arsenide cells, multijunction cells, thin films, and emerging photovoltaic (PV) technologies from its beginning upto mid 2023. Below: A highlight of the emerging PV technologies including the perovskite cells respresenting in red circles filled with yellow. Ref. [24].

1.2.2 The new-age material: Halide Perovskites

Perovskites represent a class of materials characterized by the formula ABX_3, wherein 'A' typically denotes a larger cation, either organic or inorganic in nature, 'B' refers to a smaller cation, and 'X' signifies an anion. This distinctive family of materials features an unconventional structural arrangement, encapsulating either an organic molecule or an inorganic atom 'A' within an inorganic cage. The structure is given in Figure 1.8 along with the potential atomic constituents for 'A,' 'B,' and 'X.'

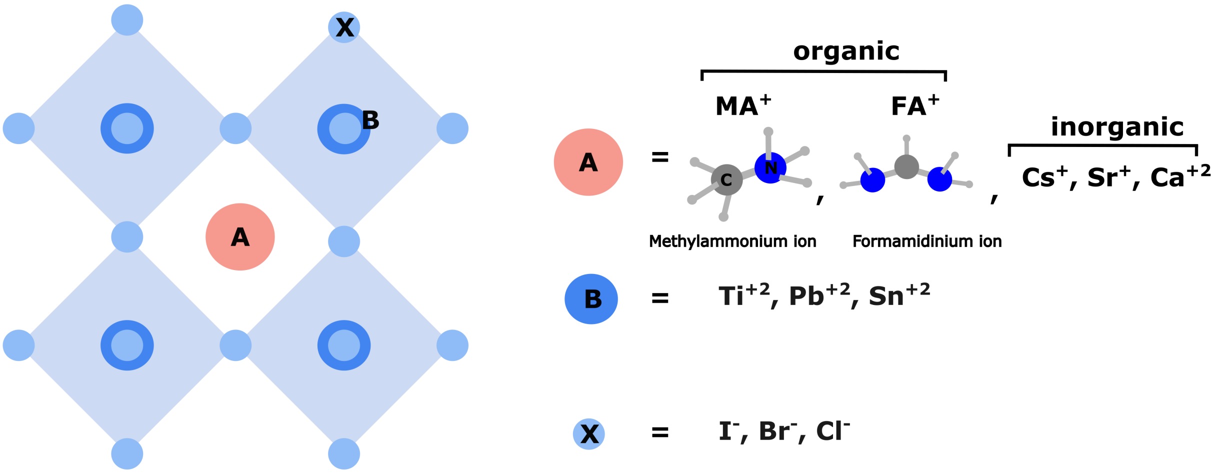

Figure 1.8: A sketch for the general structure of a halide perovskite with potential atomic constituents for the A, B and X atoms.

A plethora of permutations and combinations involving the potential A, B, and X atoms can be accommodated within the perovskite structure, leading to a diverse range of properties and applications [25]. The specific choice of these atoms can significantly impact the material's characteristics.

One critical parameter used to assess the compatibility of A, B, and X atoms in a perovskite structure is known as the "Goldschmidt tolerance factor." This factor, denoted as 't,' is calculated using the equation 1.1 [26]:

$$t = \frac{(r_A + r_X)}{\sqrt{2}(r_B + r_X)} \tag{1.1}$$

where $r_{J(J=A,B,X)}$ represents the ionic radius of atom J.

The tolerance factor 't' helps determine whether a given combination of A, B, and X atoms is suitable for forming a stable perovskite structure. A value falling within the range of 0.8 to 1.0 is considered advantageous for the formation of a cubic perovskite structure. But if its value exceeds 1.0 or falls below 0.8 typically non-perovskite structures are formed. The flexibility in choosing A, B, and X atoms in perovskite materials, combined with the evaluation of the tolerance factor, plays a crucial role in tailoring their properties for various applications. However, it's important to note that while the tolerance factor is a significant consideration, it's not the sole determinant of suitability.

1.2.3 The hybrid organic-inorganic perovskite (HOIP): MAPbI$_3$

Methylammonium lead iodide, often referred to as MAPbI$_3$, represents a notable perovskite system wherein the A-site is occupied by the MA$^+$ organic molecular ion methylammonium (CH$_3$NH$_3{}^+$). The core structural framework consists of inorganic BX$_6^{4-}$ octahedral units as PbI$_6^{4-}$, forming an interconnected three-dimensional network linked via corner halides. This arrangement adheres to the geometric constraints required for the perovskite crystal structure, as defined by the Goldschmidt tolerance factor. The value of the tolerance factor for MAPbI$_3$ is calculated to be 0.921 [27] which is close to the ideal value. Furthermore, the band gap of MAPbI$_3$ at 1.57 eV is near to the optimum band gap that provides the maximum efficiency according to the Shockley-Queisser limit, which is around 1.34 eV [28, 29].

MAPbI$_3$ has gained considerable prominence in scientific research due to its numerous advantages. It has achieved an efficiency of greater than 20% in the last decade because of the unique qualities [30]:

- Low-exciton binding energy ($\sim$ 2-50 meV) [31]
- High charge carrier mobility (>100 cm^2 V^{-1} s^{-1}) [32]
- Large exciton diffusion length (>175 μm) [32]
- Defect-tolerance [33, 34, 35, 36]
- Easy, low-cost synthesis [37]

1.3 Open issues with MAPbI$_3$

Efficiency, lifespan, and cost are often referred to as the "golden triangle" when it comes to the commercialization of photovoltaic technologies [38, 39]. As elucidated in the preceding Section 1.2.3, perovskite materials exhibit a plethora of advantageous properties, making them exceptionally promising for photovoltaic applications. They are low-cost and the efficiency of HOIP photovoltaics has surpassed the competitive benchmark of 26% power conversion efficiency [24].

However, before the perovskites can successfully penetrate the market, several critical questions must be addressed. One prominent concern revolves around the structural integrity of the MAPbI$_3$ system when exposed to external factors, including light, humidity, temperature, and electric bias. This system is prone to undergoing structural degradation, resulting in the formation of separate components such as MAI, PbI$_2$, HI, and other constituents. Conings et al. reported that MAPbI$_3$ is intrinsically unstable at higher range of operational temperatures [40]. It decomposes into its binary halide MAI and PbI$_2$ even without the presence of external stimuli. Several mechanisms have been proposed to explain this degradation, as documented in previous research [41, 42, 43, 44, 45]. These mechanisms exploit the inherent softness of the crystal lattice and the presence of crystallographic defects within the perovskite systems.

Peng et al. conducted a study that sheds light on the significance of iodine vacancies in facilitating the degradation of MAPbI$_3$ when exposed to both light and moisture [41]. Their research elucidates a proposed mechanism for this degradation process, which is represented in Figure 1.9.

Aristidou et al. delved into the investigation of oxygen diffusion and its pivotal role in mediating the degradation process through I$^-$, MA$^+$ and Pb^{+2} vacancies [45]. Their findings indicated that among these, I$^-$ vacancy sites had the most detrimental effect on the stability of the MAPbI$_3$ system.

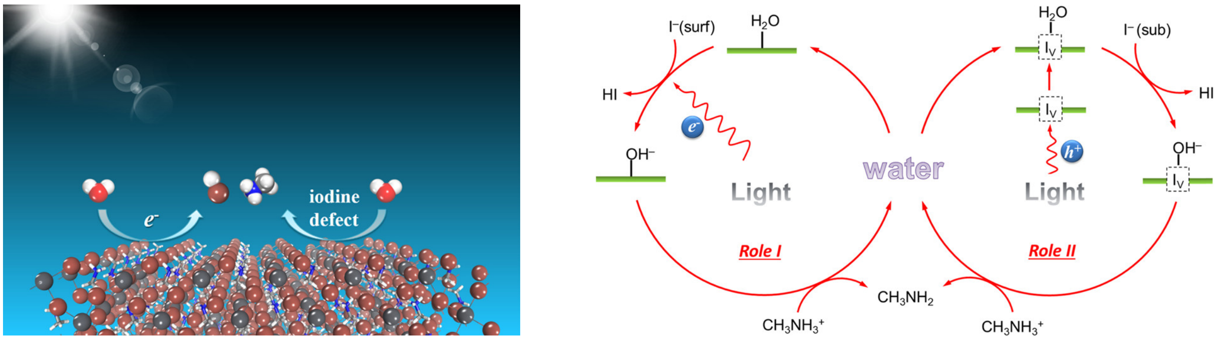

Figure 1.9: Scheme of the degradation mechanism of MAPbI$_3$ in the presence of water and light. The photogenerated carriers lower the barrier for I^- vacancy formation which leads to water dissociation, opening the way for the formation of methylamine. Ref. [41].

Overall, degradation can arise because of instability in the structure of the perovskite system or the presence of defects. This thesis focuses on addressing this issue of degradation by:

- Studying the structure of the MAPbI$_3$ system at the atomic level along with the underlying phase transitions
- Examining the defects in different phases of the MAPbI$_3$ perovskite system

By delving into these aspects, this thesis endeavors to surmount the existing challenges, propel the advancement of HOIP photovoltaics, and catalyze their integration into mainstream renewable energy solutions.

1.3.1 Lattice structure

The lattice structure of the MAPbI$_3$ system is intricate due to the coexistence of both organic and inorganic components. Li et al. explored the mutual influence of these components and discovered a synergistic relationship between the two. Specifically, they observed that the low-symmetry cation has a significant impact on the deformation of the inorganic framework, contributing to the overall stability of the hybrid perovskite structure [46]. Their computational study has also underscored the pivotal role of van der Waals (vdW) interactions in these systems [47, 48].

But still, the presence and influence of hydrogen bonding between the organic molecule and the inorganic counterpart has been under extensive study. Ibaceta-Jana et al. dismiss the existence of hydrogen bonding between the organic and inorganic components of MAPbI$_3$, referring to it as a weak ionic connection and explaining it with raman spectral data [49]. Svance et al. calculated the hydrogen bond strength of several perovskite structures to find a value of 0.09 eV for MAPbI$_3$ [50]. This small value hints at weak hydrogen bonding strength. Lee et al. also predicted a strong hydrogen bonding to influence the structure of the PbI$_6$ octahedra using an energetics profile as a function of hydrogen bonding in a system with and without octahedral tiltings [51, 52].

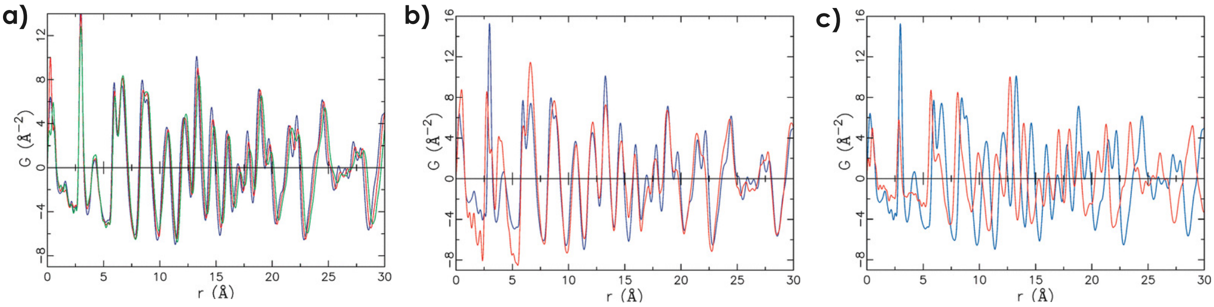

Figure 1.10: Variation of the pair-distribution function of the octahedra showing local disorder in the perovskite system as a function of varying a) organic cation: MAPbBr$_3$ (blue), FA$_{0.5}$MA$_{0.5}$PbBr$_3$ (red), and FAPbBr$_3$ (green) b) B-site composition: MAPbBr$_3$ (blue) and MASnBr$_3$ (red) c) with different halides: MAPbBr$_3$ (blue) and MAPbCl$_3$ (red). Ref. [53].

Worhatch et al. first observed the local structure in the high temperature phase of HOIPs experimentally [53]. They reported the variation of pair-distribution function of the octahedra with change in A, B and X atom. This is shown in Figure 1.10. Beecher et al. followed this approach to reveal large-amplitude rotational instabilities in the $\mathrm{PbI_6}$ octahedra of cubic $\mathrm{MAPbI_3}$ that persist to room temperature after structural phase transition [54]. For the computational modelling of this local structure, Zhao et al. recentlly reported the concept of polymorphism using which this local structure with low-symmetry local motifs, including tilting, rotations and B-atom displacements, can be reproduced via DFT [48]. Zacharias et al. further concluded that cubic perovskites with local distortion is the best possible approximation for the high temperature perovskite systems, as this allows electrons to see the nuclei fixed in their disordered ground state [55].

Jinnouchi et al. used Machine-Learning force fields to simulate phase transitions in $\mathrm{MAPbI_3}$ [56]. They studied the evolution of lattice parameters, orientaions of the organic molecule and tiltings in the inorganic cage between the three observed phases: orthorhombic, tetragonal and cubic. They conclude that the transition between the orthorhombic and tetragonal phase follows first order transition because of unfreezing of the organic molecules.

Overall, the structure and the phase transformations in $\mathrm{MAPbI_3}$ are poorly understood and further research needs to be conducted to understand them.

1.3.2 Defects in MAPbI$_3$

Defects can emerge in perovskite materials during both their synthesis and operational phases [57, 58]. Interestingly, when comparing defect densities between silicon and MAPbI$_3$ single crystals, a remarkable difference becomes evident. Silicon single crystals typically exhibit a relatively low defect density of approximately 10^8cm^{-3} [33], whereas MAPbI$_3$ single crystals display a much higher defect density, on the order of 10^{11}cm^{-3} [33, 59]. Generally, such defects have deleterious effects on the performance of semiconductor materials.

Surprisingly, despite the substantially greater defect density observed in MAPbI$_3$ compared to silicon, the resultant reduction in efficiency is not as pronounced as one might anticipate. Therefore, perovskite materials are often characterized as "defect-tolerant" [33, 34, 35, 36]. They exhibit a remarkable resilience to the adverse effects of defects on their electronic properties.

The underlying mechanisms that confer this defect tolerance in perovskites continue to be a subject of active research. Meggiolaro et al. conducted a notable investigation into this phenomenon, by examining the various charge states of iodine [33]. They reported a kinetic deactivation of the electron traps to explain the defect tolerance observed in MAPbI$_3$. On the contrary, Zhang et al. report iodine interstitials as the most important non-radiative recombination centers in hybrid perovskites using configuration coordinate diagrams [60]. With this, they also rule out the probability of Iodine vacancies to cause non-radiative recombination in hybrid or halide perovskites [61, 62, 60].

Defects, though they may be less pronounced in their impact, remain a significant concern in perovskite materials. These imperfections can trigger undesirable phenomena such as ion migration, aging and non-radiative recombination which can compromise the performance of these devices [63, 64, 65]. Though several experimental studies report the presence of defects [66, 59, 67, 68], they still lack in their microscopic identification [69]. This is where positron annihilation techniques comes into picture, but its potential for defect identification has not been explored much in the field of halide perovskites until recently.

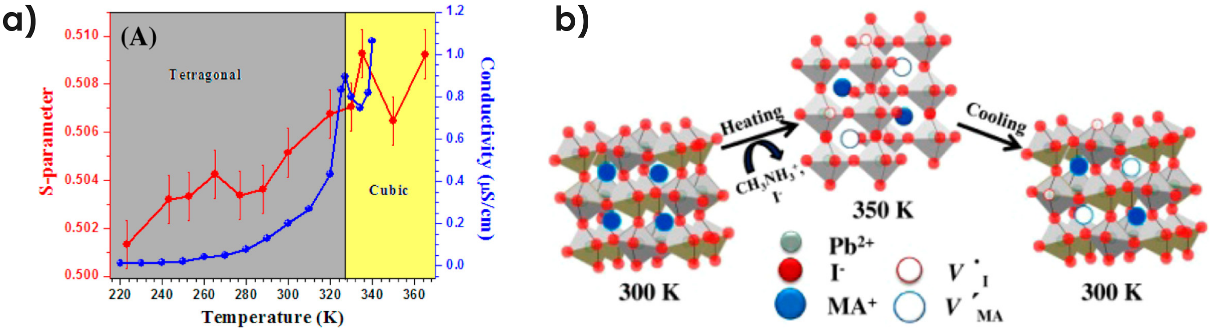

Figure 1.11: a) Temperature-dependent positron annihilation spectroscopy and conductivity plot for $MAPbI_3$. S-parameter is an indication of the number of defects as it measures the ratio of the positron annihilating with low and high momentum electrons present in defective sites and in the bulk respectively. b) The schematic representation of structural change bringing about a change in the number of defects in $MAPbI_3$. Ref. [63].

Positron annihilation spectroscopy is generally used to study vacancy defects in semiconductors. Dhar et al. employed this methodology to show the existence of MA^+ defects within the crystal lattice of $MAPbI_3$ [70]. Additionally, they conducted a temperature-dependent positron annihilation spectroscopic analysis, demonstrating the development of vacancies as temperature rose [63]. This observed rise in vacancy concentrations is closely correlated with the increasing conductivity, implying the involvement of ionic currents in the electrical response. This is depicted in Figure 1.11.

Contrasting with the findings in the case of $MAPbI_3$, the research conducted by Moshat et al. concerning $MAPbBr_3$ reveals a distinct pattern. In their investigation, they did not observe a gradual rise in defects with increasing temperature. Instead, their study found a sudden surge in defects occurring during the structural phase transition from tetragonal to cubic phase, as documented in their recent work [71]. This distinctive observation highlights the sensitivity of perovskite materials to structural changes and underscores the importance of phase transitions in influencing their defect dynamics.

Sil et al. published another experimental positron annihilation spectroscopic measurement investigation of applied bias on $MAPbI_3$ [58]. They reported the formation of irreversible lattice defects on the application of bias voltage beyond the threshold value of 1.2 V. This is shown in Figure 1.12.

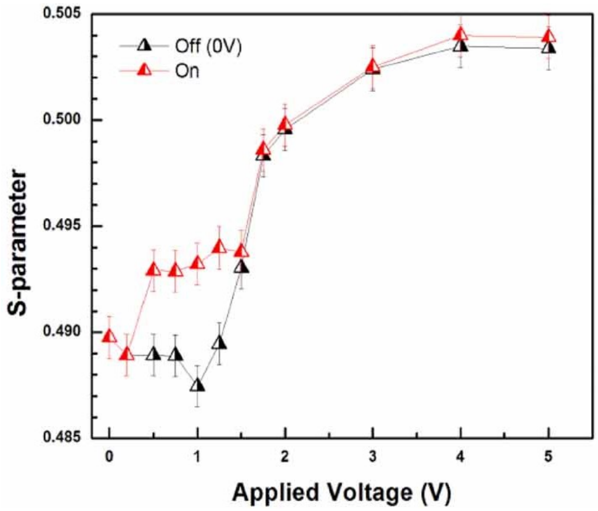

Figure 1.12: Variation of positron annihilation S-parameter with applied bias (on) and the same after withdrawing voltage (off). S-parameter is an indication of the number of defects as it measures the ratio of the positron annihilating with low and high momentum electrons present in defective sites and in the bulk respectively. Ref. [58].

There are not many computational studies available for the study of defects in MAPbI$_3$ using positron annihilation spectroscopy. This is needed in order to provide positron annihilation spectroscopic experiments a theoretical perspective that can aid in the interpretation of experimental data. This would allow a better understanding of vacancy defects, because the characterization of these defects is challenging. Computations can help in correlating the lifetimes to a specific defect or a set of defects and avoid their misinterpretation [72]. As per our knowledge, there is only one study in literature of MAPbI$_3$ using DFT. Keeble et al. report the positron annihilation lifetime of tetragonal MAPbI$_3$ in the perfect state as well as in presence of cationic defects using MIKA and ABINIT softwares [69]. Their finding are given in Figure 1.13. After comparison of the theoretical and experimental positron annihilation lifetimes, they report the V_{Pb}^{-2} as the most stable vacancy defect in MAPbI$_3$.

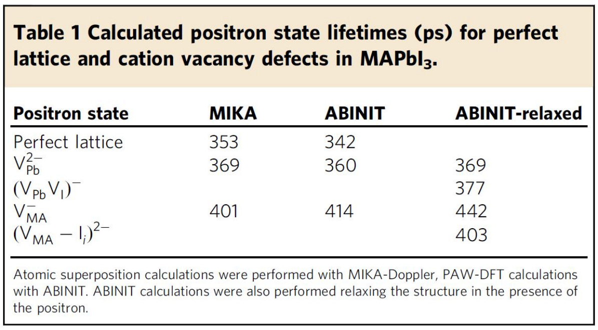

Table 1 Calculated positron state lifetimes (ps) for perfect lattice and cation vacancy defects in MAPbI$_3$.

Positron state	MIKA	ABINIT	ABINIT-relaxed
Perfect lattice	353	342	
V_{Pb}^{2-}	369	360	369
$(V_{Pb}V_{I})^{-}$			377
V_{MA}^{-}	401	414	442
$(V_{MA} - I_{i})^{2-}$			403

Atomic superposition calculations were performed with MIKA-Doppler, PAW-DFT calculations with ABINIT. ABINIT calculations were also performed relaxing the structure in the presence of the positron.

Figure 1.13: Table for the positron annihilation lifetimes for MAPbI$_3$. The image is taken from [69].

REFERENCES

[1] James Hansen, Pushker Kharecha, Makiko Sato, Valerie Masson-Delmotte, Frank Ackerman, David J Beerling, Paul J Hearty, Ove Hoegh-Guldberg, Shi-Ling Hsu, Camille Parmesan, et al. Assessing "dangerous climate change": Required reduction of carbon emissions to protect young people, future generations and nature. *PloS one*, 8(12):e81648, 2013. pages 13

[2] Meyer Steinberg. Fossil fuel decarbonization technology for mitigating global warming. *International Journal of Hydrogen Energy*, 24(8):771–777, 1999. pages 13

[3] Charles W Garrett. On global climate change, carbon dioxide, and fossil fuel combustion. *Progress in Energy and Combustion Science*, 18(5):369–407, 1992. pages 13

[4] Charles Simeons. *Hydro-power: the use of water as an alternative source of energy*. Elsevier, 2014. pages 13

[5] A Boudghene Stambouli and Enrico Traversa. Fuel cells, an alternative to standard sources of energy. *Renewable and sustainable energy reviews*, 6(3):295–304, 2002. pages 13

[6] Richard H Taylor. Alternative energy sources for the centralised generation of electricity. 1983. pages 13

[7] Mariano Martín Martín and IE Grossmann. *Alternative energy sources and technologies*, volume 10. Springer, 2016. pages 13

[8] Mildred Spiewak Dresselhaus and IL Thomas. Alternative energy technologies. *Nature*, 414(6861): 332–337, 2001. pages 13

[9] Hrvoje Mikulčić, Jiří Jaromír Klemeš, Milan Vujanović, Krzysztof Urbaniec, and Neven Duić. Reducing greenhouse gasses emissions by fostering the deployment of alternative raw materials and energy sources in the cleaner cement manufacturing process. *Journal of cleaner production*, 136:119–132, 2016. pages 13

[10] Siang Fui Tie and Chee Wei Tan. A review of energy sources and energy management system in electric vehicles. *Renewable and sustainable energy reviews*, 20:82–102, 2013. pages 13

[11] Vijay Devabhaktuni, Mansoor Alam, Soma Shekara Sreenadh Reddy Depuru, Robert C Green II, Douglas Nims, and Craig Near. Solar energy: Trends and enabling technologies. *Renewable and Sustainable Energy Reviews*, 19:555–564, 2013. pages 13, 17

[12] Phebe Asantewaa Owusu and Samuel Asumadu-Sarkodie. A review of renewable energy sources, sustainability issues and climate change mitigation. *Cogent Engineering*, 3(1):1167990, 2016. pages 13

[13] International Energy Agency (IEA). Total renewable capacity additions, 2002-2022, 2022. URL `https://www.iea.org/data-and-statistics/charts/total-renewable-capacity-additions-2002-2022`. Licensed under CC BY 4.0. pages 6, 13, 14

[14] International Energy Agency (IEA). Global share of total energy supply by source, 1973, 1973. URL `https://www.iea.org/data-and-statistics/charts/global-share-of-total-energy-supply-by-source-1973-2`. Licensed under CC BY 4.0. pages 6, 14

[15] International Energy Agency (IEA). Global share of total energy supply by source, 2019, 2019. URL `https://www.iea.org/data-and-statistics/charts/global-share-of-total-energy-supply-by-source-2019`. Licensed under CC BY 4.0. pages 6, 14

[16] Renewable energy market update june 2023. URL `https://www.iea.org/reports/renewable-energy-market-update-june-2023/executive-summary`. pages 6, 15, 17

[17] International Energy Agency (IEA) Photovoltaic Power Systems Programme (PVPS). Snapshot of global pv markets 2023, 2023. URL `https://iea-pvps.org/wp-content/uploads/2023/04/IEA_PVPS_Snapshot_2023.pdf`. pages 6, 16, 17

[18] Vinayak H Deokar, Rupa S Bindu, and SS Potdar. Active cooling system for efficiency improvement of pv panel and utilization of waste-recovered heat for hygienic drying of onion flakes. *Journal of Materials Science: Materials in Electronics*, 32(2):2088–2102, 2021. pages 17

[19] REN21. Renewables 2023 global status report, 2023. URL `https://www.ren21.net/gsr-2023/modules/energy_supply/02_market_developments/07_solarpv/`. pages 6, 17

[20] Oguz Ozan Yolcan. World energy outlook and state of renewable energy: 10-year evaluation. *Innovation and Green Development*, 2(4):100070, 2023. pages 17

[21] Wenzhu Liu, Yujing Liu, Ziqiang Yang, Changqing Xu, Xiaodong Li, Shenglei Huang, Jianhua Shi, Junling Du, Anjun Han, Yuhao Yang, et al. Flexible solar cells based on foldable silicon wafers with blunted edges. *Nature*, 617(7962):717–723, 2023. pages 18

[22] Sudesna Roy, Mriganka Sekhar Baruah, Sasmita Sahu, and Bijaya Bijeta Nayak. Computational analysis on the thermal and mechanical properties of thin film solar cells. *Materials Today: Proceedings*, 44:1207–1213, 2021. pages 18

[23] Ebru Kondolot Solak and Erdal Irmak. Advances in organic photovoltaic cells: a comprehensive review of materials, technologies, and performance. *RSC advances*, 13(18):12244–12269, 2023. pages 6, 18, 19

[24] National Renewable Energy Laboratory (NREL). Cell efficiency | photovoltaic research | nrel, 2023. URL `https://www.nrel.gov/pv/cell-efficiency.html`. pages 6, 20, 23

[25] Jin-Wook Lee, Shaun Tan, Sang Il Seok, Yang Yang, and Nam-Gyu Park. Rethinking the a cation in halide perovskites. *Science*, 375(6583):eabj1186, 2022. pages 21

[26] Victor Moritz Goldschmidt. Die gesetze der krystallochemie. *Naturwissenschaften*, 14(21):477–485, 1926. pages 21

[27] Song Jin. Can we find the perfect A-cations for halide perovskites?, 2021. pages 22

[28] William Shockley and Hans Queisser. Detailed balance limit of efficiency of p-n junction solar cells. In *Renewable Energy*, volume 2, pages 35–54. Routledge, 2018. pages 22

[29] Giles E Eperon, Samuel D Stranks, Christopher Menelaou, Michael B Johnston, Laura M Herz, and Henry J Snaith. Formamidinium lead trihalide: a broadly tunable perovskite for efficient planar heterojunction solar cells. *Energy & Environmental Science*, 7(3):982–988, 2014. pages 22

[30] Yehui Xu, Shaobing Xiong, Sheng Jiang, Jianming Yang, Dong Li, Hongbo Wu, Xiaomeng You, Yefan Zhang, Zaifei Ma, Jianhua Xu, et al. Synchronous modulation of defects and buried interfaces for highly efficient inverted perovskite solar cells. *Advanced Energy Materials*, 13(3):2203505, 2023. pages 22

[31] Tze Chien Sum, Shi Chen, Guichuan Xing, Xinfeng Liu, and Bo Wu. Energetics and dynamics in organic–inorganic halide perovskite photovoltaics and light emitters. *Nanotechnology*, 26(34): 342001, 2015. pages 22

[32] Qingfeng Dong, Yanjun Fang, Yuchuan Shao, Padhraic Mulligan, Jie Qiu, Lei Cao, and Jinsong Huang. Electron-hole diffusion lengths> 175 μm in solution-grown $CH_3NH_3PbI_3$ single crystals. *Science*, 347 (6225):967–970, 2015. pages 22

[33] Daniele Meggiolaro, Silvia G Motti, Edoardo Mosconi, Alex J Barker, James Ball, Carlo Andrea Riccardo Perini, Felix Deschler, Annamaria Petrozza, and Filippo De Angelis. Iodine chemistry determines the defect tolerance of lead-halide perovskites. *Energy & Environmental Science*, 11(3):702–713, 2018. pages 22, 27

[34] Xie Zhang, Mark E Turiansky, Jimmy-Xuan Shen, and Chris G Van de Walle. Defect tolerance in halide perovskites: A first-principles perspective. *Journal of Applied Physics*, 131(9), 2022. pages 22, 27

[35] Basita Das, Zhifa Liu, Irene Aguilera, Uwe Rau, and Thomas Kirchartz. Defect tolerant device geometries for lead-halide perovskites. *Materials advances*, 2(11):3655–3670, 2021. pages 22, 27

[36] K Xerxes Steirer, Philip Schulz, Glenn Teeter, Vladan Stevanovic, Mengjin Yang, Kai Zhu, and Joseph J Berry. Defect tolerance in methylammonium lead triiodide perovskite. *ACS Energy Letters*, 1(2):360–366, 2016. pages 22, 27

[37] Yangning Zhang, Timothy D Siegler, Cherrelle J Thomas, Michael K Abney, Tushti Shah, Anastacia De Gorostiza, Randalynn M Greene, and Brian A Korgel. A "tips and tricks" practical guide to the synthesis of metal halide perovskite nanocrystals. *Chemistry of Materials*, 32(13):5410–5423, 2020. pages 22

[38] Xiaobin Gu, Yanan Wei, Guanyu Lu, Ziyang Han, Di Zheng, Guanghao Lu, Jianqi Zhang, Zhixiang Wei, Yunhao Cai, Xin Zhang, et al. Insight into the efficiency-stability-cost balanced organic solar cell based on a polymerized nonfused-ring electron acceptor. *Aggregate*, page e388, 2023. pages 23

[39] Lei Meng, Jingbi You, and Yang Yang. Addressing the stability issue of perovskite solar cells for commercial applications. *Nature communications*, 9(1):5265, 2018. pages 23

[40] Bert Conings, Jeroen Drijkoningen, Nicolas Gauquelin, Aslihan Babayigit, Jan D'Haen, Lien D'Olieslaeger, Anitha Ethirajan, Jo Verbeeck, Jean Manca, Edoardo Mosconi, et al. Intrinsic thermal

instability of methylammonium lead trihalide perovskite. *Advanced Energy Materials*, 5(15):1500477, 2015. pages 23

[41] Chao Peng, Jianfu Chen, Haifeng Wang, and Peijun Hu. First-principles insight into the degradation mechanism of $CH_3NH_3PbI_3$ perovskite: light-induced defect formation and water dissociation. *The Journal of Physical Chemistry C*, 122(48):27340–27349, 2018. pages 7, 23, 24

[42] Panteha Toloueinia, Hamidreza Khassaf, Alireza Shirazi Amin, Zachary M Tobin, S Pamir Alpay, and Steven L Suib. Moisture-induced structural degradation in methylammonium lead iodide perovskite thin films. *ACS Applied Energy Materials*, 3(9):8240–8248, 2020. pages 23

[43] Aleksei Yu Grishko, Maria A Komkova, Ekaterina I Marchenko, Alexandra V Chumakova, Alexey B Tarasov, Eugene A Goodilin, and Andrei A Eliseev. Evidence for polarization-induced phase transformations and degradation in $CH_3NH_3PbI_3$. *Nano Research*, pages 1–8, 2023. pages 23

[44] Philip Schulz, David Cahen, and Antoine Kahn. Halide perovskites: is it all about the interfaces? *Chemical reviews*, 119(5):3349–3417, 2019. pages 23

[45] Nicholas Aristidou, Christopher Eames, Irene Sanchez-Molina, Xiangnan Bu, Jan Kosco, M Saiful Islam, and Saif A Haque. Fast oxygen diffusion and iodide defects mediate oxygen-induced degradation of perovskite solar cells. *Nature communications*, 8(1):15218, 2017. pages 23

[46] Jingrui Li and Patrick Rinke. Atomic structure of metal-halide perovskites from first principles: The chicken-and-egg paradox of the organic-inorganic interaction. *Physical Review B*, 94(4):045201, July 2016. ISSN 2469-9950, 2469-9969. doi: 10.1103/PhysRevB.94.045201. pages 25

[47] Miguel A Perez-Osorio, Aurelie Champagne, Marios Zacharias, Gian-Marco Rignanese, and Feliciano Giustino. Van der waals interactions and anharmonicity in the lattice vibrations, dielectric constants, effective charges, and infrared spectra of the organic–inorganic halide perovskite $CH_3NH_3PbI_3$. *The Journal of Physical Chemistry C*, 121(34):18459–18471, 2017. pages 25

[48] Xin-Gang Zhao, Gustavo M Dalpian, Zhi Wang, and Alex Zunger. Polymorphous nature of cubic halide perovskites. *Physical Review B*, 101(15):155137, 2020. pages 25, 26

[49] Josefa Ibaceta-Jaña, Manjusha Chugh, Alexander S Novikov, Hossein Mirhosseini, Thomas D Kuhne, Bernd Szyszka, Markus R Wagner, and Ruslan Muydinov. Do lead halide hybrid perovskites have hydrogen bonds? *The Journal of Physical Chemistry C*, 126(38):16215–16226, 2022. pages 25

[50] Katrine L Svane, Alexander C Forse, Clare P Grey, Gregor Kieslich, Anthony K Cheetham, Aron Walsh, and Keith T Butler. How strong is the hydrogen bond in hybrid perovskites? *The journal of physical chemistry letters*, 8(24):6154–6159, 2017. pages 25

[51] Jung-Hoon Lee, Nicholas C Bristowe, Paul D Bristowe, and Anthony K Cheetham. Role of hydrogen-bonding and its interplay with octahedral tilting in $CH_3NH_3PbI_3$. *Chemical Communications*, 51(29): 6434–6437, 2015. pages 25

[52] Jung-Hoon Lee, Nicholas C Bristowe, June Ho Lee, Sung-Hoon Lee, Paul D Bristowe, Anthony K Cheetham, and Hyun Myung Jang. Resolving the physical origin of octahedral tilting in halide perovskites. *Chemistry of Materials*, 28(12):4259–4266, 2016. pages 25

[53] Richard J Worhatch, HyunJeong Kim, Ian P Swainson, André L Yonkeu, and Simon JL Billinge. Study of local structure in selected organic-inorganic perovskites in the $Pm\bar{3}m$ phase. *Chemistry of Materials*, 20(4):1272–1277, 2008. pages 7, 25, 26

[54] Alexander N. Beecher, Octavi E. Semonin, Jonathan M. Skelton, Jarvist M. Frost, Maxwell W. Terban, Haowei Zhai, Ahmet Alatas, Jonathan S. Owen, Aron Walsh, and Simon J. L. Billinge. Direct Observation of Dynamic Symmetry Breaking above Room Temperature in Methylammonium Lead Iodide Perovskite. *ACS Energy Letters*, 1(4):880–887, October 2016. ISSN 2380-8195, 2380-8195. doi: 10.1021/acsenergylett.6b00381. arXiv: 1606.09267. pages 26

[55] Marios Zacharias, George Volonakis, Feliciano Giustino, and Jacky Even. Anharmonic electron-phonon coupling in ultrasoft and locally disordered perovskites. *arXiv preprint arXiv:2302.09625*, 2023. pages 26

[56] Ryosuke Jinnouchi, Jonathan Lahnsteiner, Ferenc Karsai, Georg Kresse, and Menno Bokdam. Phase transitions of hybrid perovskites simulated by machine-learning force fields trained on the fly with bayesian inference. *Physical review letters*, 122(22):225701, 2019. pages 26

[57] Gerardo Gordillo, Oscar G Torres, Maria Camila Abella, Julian C Pena, and Ophyr Virguez. Improving the stability of $MAPbI_3$ films by using a new synthesis route. *Journal of Materials Research and Technology*, 9(6):13759–13769, 2020. pages 27

[58] Sayantan Sil, Sudipta Moshat, Partha Pratim Ray, Joydeep Dhar, and Dirtha Sanyal. Investigating the effect of applied bias on methylammonium lead iodide perovskite by electrical and positron

annihilation spectroscopic studies. *Journal of Physics D: Applied Physics*, 54(46):465502, 2021. pages 7, 27, 28, 29

[59] Valerio Adinolfi, Mingjian Yuan, Riccardo Comin, Emmanuel S Thibau, Dong Shi, Makhsud I Saidaminov, Pongsakorn Kanjanaboos, Damir Kopilovic, Sjoerd Hoogland, Zheng-Hong Lu, et al. The in-gap electronic state spectrum of methylammonium lead iodide single-crystal perovskites. *Advanced materials*, 28(17):3406–3410, 2016. pages 27

[60] Xie Zhang, Mark E Turiansky, Jimmy-Xuan Shen, and Chris G Van de Walle. Iodine interstitials as a cause of nonradiative recombination in hybrid perovskites. *Physical Review B*, 101(14):140101, 2020. pages 27

[61] Jingda Zhang, Xie Zhang, Mark E Turiansky, and Chris G Van de Walle. Iodine vacancies do not cause nonradiative recombination in halide perovskites. *PRX Energy*, 2(1):013008, 2023. pages 27

[62] Xie Zhang, Jimmy-Xuan Shen, Mark E Turiansky, and Chris G Van de Walle. Minimizing hydrogen vacancies to enable highly efficient hybrid perovskites. *Nature Materials*, 20(7):971–976, 2021. pages 27

[63] Joydeep Dhar, Sayantan Sil, Arka Dey, Partha Pratim Ray, and Dirtha Sanyal. Positron annihilation spectroscopic investigation on the origin of temperature-dependent electrical response in methylammonium lead iodide perovskite. *The Journal of Physical Chemistry Letters*, 8(8):1745–1751, 2017. pages 7, 27, 28

[64] Lijian Zuo, Zexin Li, and Hongzheng Chen. Ion migration and accumulation in halide perovskite solar cells. *Chinese Journal of Chemistry*, 41(7):861–876, 2023. pages 27

[65] Kostiantyn Sakhatskyi, Rohit Abraham John, Antonio Guerrero, Sergey Tsarev, Sebastian Sabisch, Tisita Das, Gebhard J Matt, Sergii Yakunin, Ihor Cherniukh, Martin Kotyrba, et al. Assessing the drawbacks and benefits of ion migration in lead halide perovskites. *ACS Energy Letters*, 7(10):3401–3414, 2022. pages 27

[66] DW de Quilettes, SM Vorpahl, SD Stranks, H Nagaoka, GE Eperon, ME Ziffer, HJ Snaith, and DS Ginger. Impact of microstructure on local carrier lifetime in perovskite solar cells. *Science*, 348(6235):683–686, 2015. pages 27

[67] Yin Chen, HT Yi, X Wu, R Haroldson, YN Gartstein, YI Rodionov, KS Tikhonov, A Zakhidov, X-Y Zhu, and V Podzorov. Extended carrier lifetimes and diffusion in hybrid perovskites revealed by hall effect and photoconductivity measurements. *Nature communications*, 7(1):12253, 2016. pages 27

[68] Tomas Leijtens, Giles E Eperon, Alex J Barker, Giulia Grancini, Wei Zhang, James M Ball, Ajay Ram Srimath Kandada, Henry J Snaith, and Annamaria Petrozza. Carrier trapping and recombination: the role of defect physics in enhancing the open circuit voltage of metal halide perovskite solar cells. *Energy & Environmental Science*, 9(11):3472–3481, 2016. pages 27

[69] David J Keeble, Julia Wiktor, Sandeep K Pathak, Laurie J Phillips, Marcel Dickmann, Ken Durose, Henry J Snaith, and Werner Egger. Identification of lead vacancy defects in lead halide perovskites. *Nature Communications*, 12(1):5566, 2021. pages 7, 27, 29

[70] Joydeep Dhar, Sayantan Sil, Arka Dey, Dirtha Sanyal, and Partha Pratim Ray. Investigation of ion-mediated charge transport in methylammonium lead iodide perovskite. *The Journal of Physical Chemistry C*, 121(10):5515–5522, 2017. pages 28

[71] Sudipta Moshat, Partha Pratim Ray, Sayantan Sil, Joydeep Dhar, and Dirtha Sanyal. Positron annihilation studies of methylammonium lead bromide perovskite. *Physica Scripta*, 98(3):035822, 2023. pages 28

[72] PA Sterne and JH Kaiser. First-principles calculation of positron lifetimes in solids. *Physical Review B*, 43(17):13892, 1991. pages 29

Chapter 2

Theoretical Framework and Computational Methodology

> The steady progress of physics requires for its theoretical formulation a mathematics that gets continually more advanced.
>
> Paul Adrien Maurice Dirac

In this chapter, we delve into the theoretical framework and computational methodology employed to investigate the structure and vacancy defects in MAPbI$_3$ perovskite.

Section 2.1 focuses on the handling of the sub-atomic species- electrons and positrons, which should be described quantum-mechanically. In subsection 2.1.1, we provide an exploration of the Density Functional Theory (DFT) utilized for atomic-level analysis of the system. We elucidate the key steps of the algorithm implemented by the Quantum espresso software, accompanied by informative flowcharts. Moving forward, subsection 2.1.2 delves into the theory behind positron annihilation spectroscopy, an approach employed to study vacancy defects in materials. We further elucidate the algorithm employed by the ATSUP software through descriptive flowcharts.

In Section 2.2, we shift our attention to the structural intricacies governing the tiltings within the octahedral cage and the orientations of organic molecules in different phases of the MAPbI$_3$ perovskite. To investigate these aspects, we employ techniques such as pair distribution function and the Nudged Elastic Band (NEB) method.

Section 2.3 delves into the realm of defect thermodynamics, encompassing discussions on chemical potentials, defect formation energies, and the characterization of vacancy defects through voronoi volumes.

2.1 Electronic and atomic structure for electrons and positrons

2.1.1 Density Functional Theory: Basics and Application

Density Functional theory, commonly referred to as ab initio or from first principles, is a computational material modelling method to calculate the electronic structure of materials. This approach is founded on the solution of the time-independent Schrödinger equation (TISE), providing a reliable and efficient means to model and analyze various materials. TISE is given in equations 2.1 and 2.2.

$$H\Psi\left(\mathbf{x}_1, \mathbf{x}_2, \ldots, \mathbf{x}_N\right) = E\Psi\left(\mathbf{x}_1, \mathbf{x}_2, \ldots, \mathbf{x}_N\right) \tag{2.1}$$

where H is the Hamiltonian, E is the energy eigenvalue and ψ(x$_1$, x$_2$..., x$_N$) is the wave-function eigenstate with space-spin coordinates x$_i$=(r$_i$, σ_i) and r$_i \in$ R^3.

$$H_e = -\frac{1}{2}\sum_{i=1}^{N}\nabla_{\mathbf{r}_i}^2 + \frac{1}{2}\sum_{i=1}^{N}\sum_{\substack{j=1\\ i\neq j}}^{N}\frac{1}{\left|\mathbf{r}_i - \mathbf{r}_j\right|} + \sum_{i=1}^{N} v_{\mathrm{ne}}\left(\mathbf{r}_i\right) \tag{2.2}$$

where H$_e$ is the electronic Hamiltonian within the Born-Oppenheimer approximation [1], first segment is the kinetic energy interaction part, second segment is the electron-electron interaction part and last one with v$_{ne}$ is the electron-nuclei interaction term. The energy is in Hartrees, distances are in Bohr and mass in atomic units for simplification.

DFT incorporates the concept of electron density, which simplifies the complex many-body problem of interacting electrons. By focusing on the electron density rather than the wave function of each electron, DFT reduces the computational complexity from a 3N-dimensional problem (where N is the number of electrons) to a 3-dimensional problem. This reduction significantly improves the computational efficiency, enabling the study of larger systems and longer timescales.

DFT is built upon two fundamental theorems:

1. Hohenberg-Kohn theorem:

   It states that the electron density uniquely determines the ground-state wave-function and, therefore, all observable properties of the system. According to this theorem, the density that minimizes the total energy is the exact ground state density (Equation 2.3).

   $$E_0 = \min \in \langle \Psi | \hat{H} | \Psi \rangle \tag{2.3}$$

   It lays the groundwork for reducing the dependency from 3N spatial coordinates to 3 spatial coordinates via functionals of electron density [2].

2. Kohn-Sham theorem:

   According to the Kohn-Sham theorem, the electronic structure can be described by a set of non-interacting electrons in an effective potential (Equation 2.4) [3, 4]. This effective potential is often referred to as the Kohn-Sham potential. The total electron density is expressed as a sum of densities of individual electrons, each moving in an effective potential. The effective potential includes four contributions: the external potential, which arises from the interaction of electrons with the atomic nuclei, kinetic energy of the electrons, Hartree potential and the exchange-correlation potential, which account for the remaining part of the electron-electron interaction. By solving the Kohn-Sham equations self-consistently, one can obtain the electronic structure of the system.

$$E = \overbrace{\underbrace{\int d\mathbf{r} n(\mathbf{r}) V_{\mathrm{n}}(\mathbf{r})}_{\text{External potential}} - \underbrace{\sum_i \int d\mathbf{r} \phi_i^*(\mathbf{r}) \frac{\nabla^2}{2} \phi_i(\mathbf{r})}_{\text{Kinetic energy}} + \underbrace{\frac{1}{2} \iint d\mathbf{r} d\mathbf{r}' \frac{n(\mathbf{r}) n(\mathbf{r}')}{|\mathbf{r} - \mathbf{r}'|}}_{\text{Hartree energy}}}^{\text{Total energy in the independent electrons approximation}} + \underbrace{E_{xc}[n]}_{\text{XC energy}} . \tag{2.4}$$

2.1.1.1 eXchange Correlation (XC) functionals

DFT employs exchange-correlation functionals, in addition to the Hartree potential, to account for the electron-electron interactions that are not explicitly considered in the Kohn-Sham non-interacting system. These functionals capture the effects of electron-electron correlation and exchange, essential for accurately describing the electronic structure and energetics of materials. This part of the total energy functional remains unknown and need to be approximated.

There are several approximations known for this purpose. These include:

- **Local-density approximation (LDA)**

  This exchange-correlation functional depends only on the density at the coordinate where the function is evaluated.

  $$E_{xc}^{LDA}[n] = \int \epsilon_{xc}(n)n(r)dr \tag{2.5}$$

  where ϵ_{xc}(n) is the exchange-correlation energy density.

  It treats all systems as homogeneous. It is valid only for slowly varying densities but become problematic for weakly bonded systems, such as van-der-Waals (vdW) and H-bonded systems. It underestimates the H-bonding interactions and completely neglects the long-range vdW interactions.

- **Generalized Gradient approximation (GGA)**

  In contrast to LDA, GGA takes into account the inhomogeneity of systems by including the information about the derivative of density into the exchange-correlation functionals [5].

  $$E_{xc}^{GGA}[n] = \int f(n(r), \nabla n(r))dr \tag{2.6}$$

  They are called 'semi-local' functionals due to their dependence on density gradient ∇n(r). In general, they are better than LDA especially for covalent and weakly bonded systems. Because of the flexibility of the choice of PBE, PBEsol and optB86 are some examples of GGA exchange-correlation functionals.

  For the majority of calculations in this thesis, we employ optB86-vdw XC functional [6]. It is a GGA functional which includes an additional van-der-Waals component for capturing the weak interaction in hybrid organic-inorganic perovskites. Specifically, it takes into account the weak linkage between the hydrogens attached to the nitrogen head in methylammonium molecule, henceforth refereed to as H$_N$, and iodine. It has previously been used for similar studies [7].

2.1.1.2 Achieving self-consistent ground state

The self-consistency procedure to achieve the convergence of the charge density based on the concepts given above is schematically represented in Figure 2.1 [4].

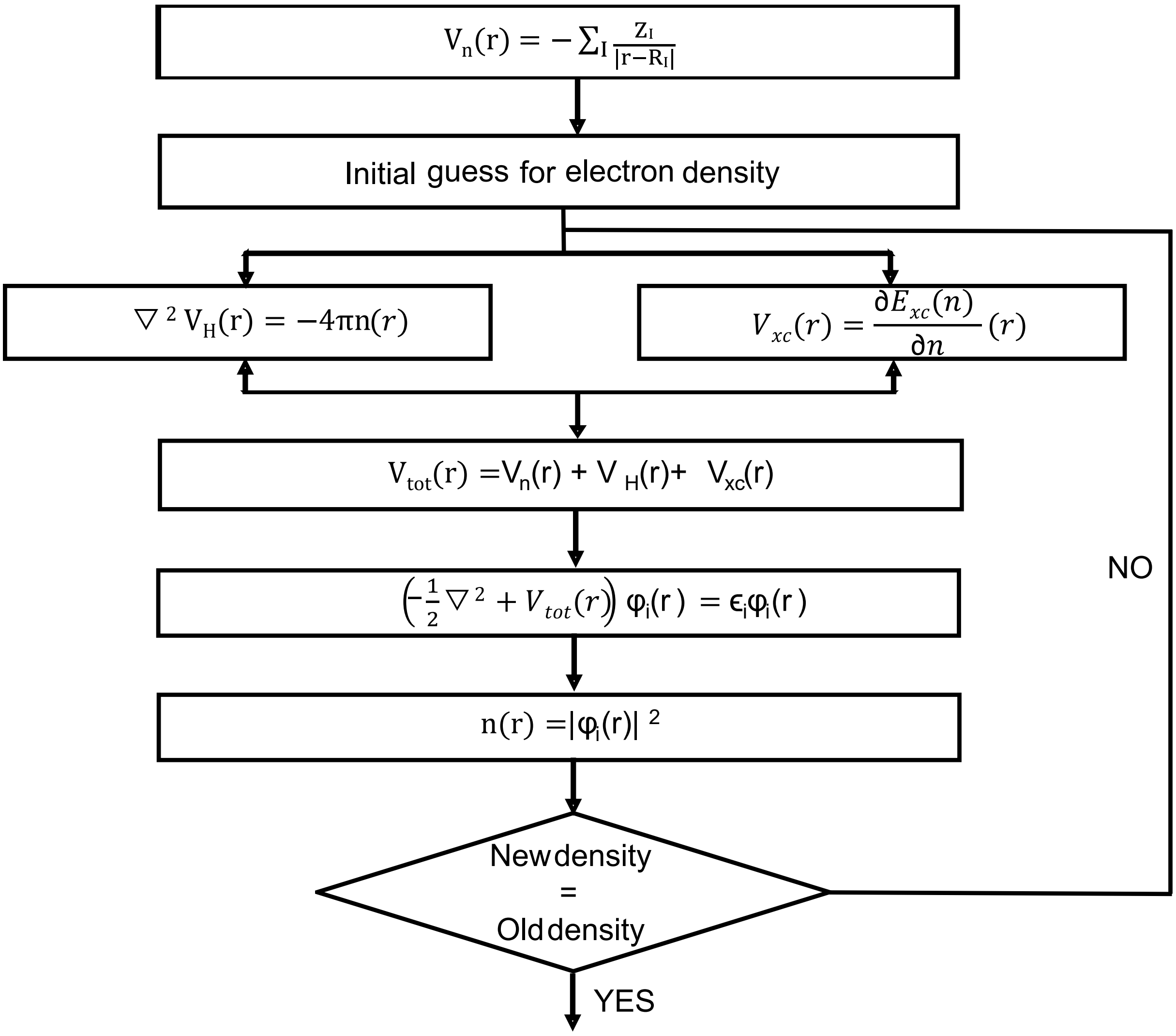

Figure 2.1: Mapping the Iterative Path for Self-Consistent Field algorithm in Density Functional Theory (DFT) [4].

2.1.1.3 About Quantum Espresso

Quantum Espresso is an open source package for research in electronic structure, Simulation and Optimization distributed under the GNU General Public License [8]. It utilizes density functional theory to calculate the ground-state properties of materials within the plane wave based PWscf(Plane-Wave Self-Consistent Field) component. The optimization algorithm used by Quantum Espresso is presented in a flowchart format in Figure 2.2. All calculations presented in this thesis were conducted using Quantum Espresso, unless otherwise specified.

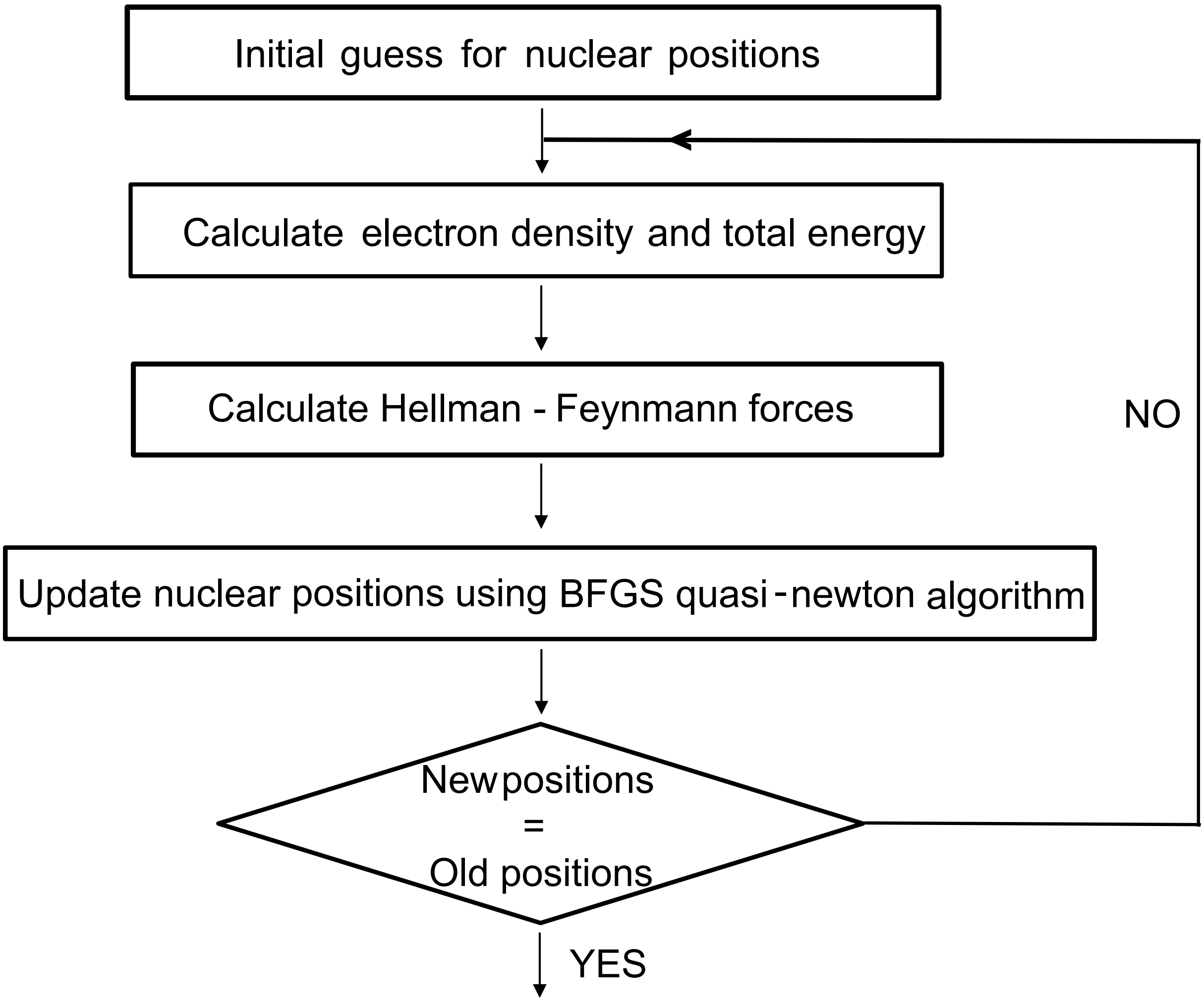

Figure 2.2: Navigating the Path to Equilibrium Structure in Quantum Espresso adapted from [4].

Note that within Density Functional Theory (DFT) the calculations are done at 0 Kelvin, meaning it does not explicitly account for temperature effects.

2.1.1.4 Pseudo-potentials and plane-wave basis set

A pseudo-potential is a mathematical approximation used in Density Functional Theory (DFT) to describe the interaction between valence electrons and the other (core) electrons in a solid or molecule. It is an effective potential that simplifies the computations while retaining the fundamental physics, rather than a real depiction of the electron-ion interaction. This reduces the overall computational cost. There are different types of pseudo-potentials, such as norm-conserving (NC), projector augmented-wave (PAW) and ultrasoft (US) [9].

In solids, the periodicity of the atomic arrangements is dealt with using the Bloch theorem where a plane-wave basis set is used instead of a gaussian basis set [10]. The maximum energy above which these plane-waves are truncated in the expansion of the electronic wave functions is known as the cutoff energy. It is a trade-off between the accuracy of the exchange-correlation and the number of plane-waves necessary for the total energy calculation.

To optimize the cutoff energy, test calculations were conducted on the cubic $MAPbI_3$. The optimization graphs are given in Figure 2.3.

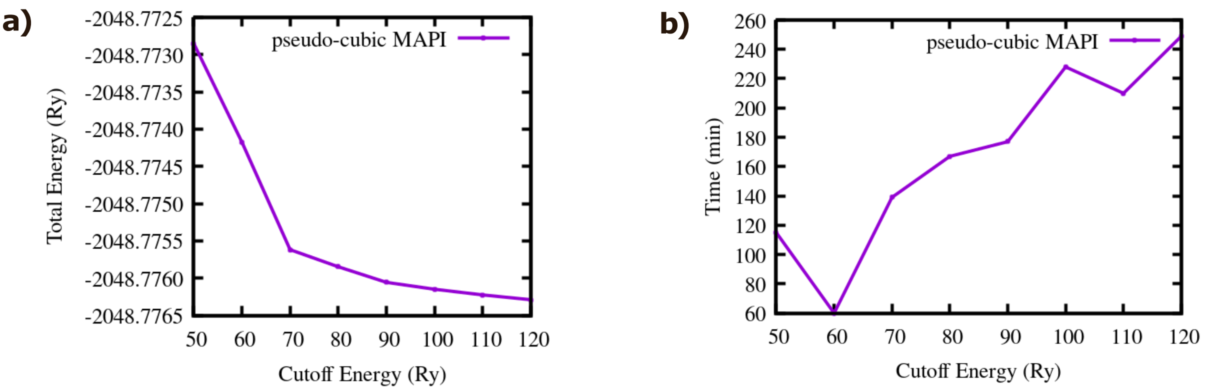

Figure 2.3: Test for convergence of the cutoff energy with PAW pseudo-potentials for N, Pb, I and NC ones for C and H. These tests are with OptB86-vdw functional. a) Total energy vs. Cutoff energy and b) Time vs. Cutoff energy graphs for the cubic $MAPbI_3$. Here, time is the wall time with same parallelisation parameters.

A cutoff of 70 Ry with US pseudo-potentials with I [$5s^2 5p^5$] and Pb [$5d^{10} 6s^2 6p^2$] electrons treated as valence states were used for all subsequent calculations on $MAPbI_3$ phases.

2.1.1.5 Brillouin-zone sampling

A Monkhorst-Pack k-point mesh is a specific type of discretization scheme used to sample the Brillouin zone. It maintains the symmetry of the lattice and preserves important high-symmetry points in the Brillouin zone. The method aims to strike a balance between computational efficiency and accuracy by providing sufficient k-points for an accurate representation of electronic properties while minimizing computational cost [11].

Convergence tests were performed to determine the appropriate k-point mesh for calculations using LDA, GGA and OptB86-vdw. The results indicated that an 8 × 8 × 8 Monkhorst-Pack k-point mesh was sufficient for achieving convergence with the LDA functional. For the GGA and OptB86-vdw functionals, a slightly less denser 6 × 6 × 6 Monkhorst-Pack K-point mesh was sufficient.

A K-point mesh of 6 × 6 × 6 was used for all further calculations on $MAPbI_3$ phases using OptB86-vdw functional according the the Figure 2.4.

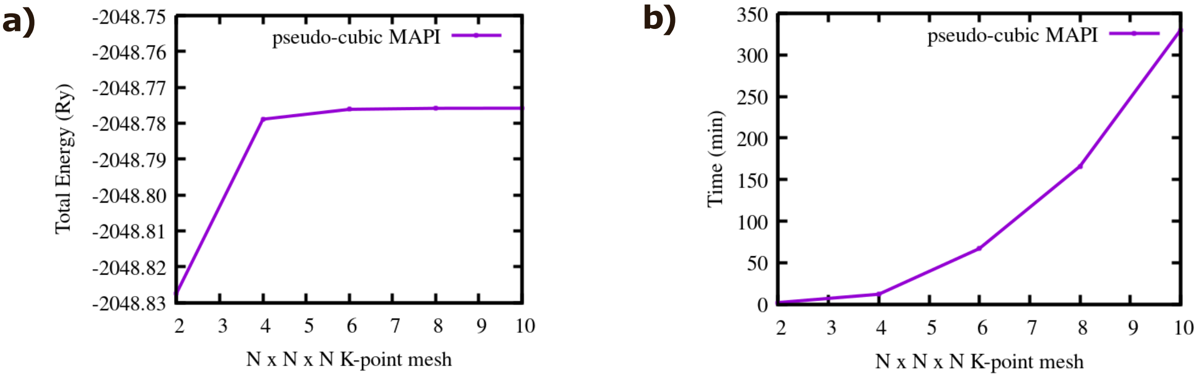

Figure 2.4: Test for convergence of the Monkhorst pack K-point mesh used using OptB86-vdw functional. a) Total energy vs. K-point and b) Time vs. K-point graphs for the cubic $MAPbI_3$. Here, time is the wall time with same parallelisation parameters.

In this thesis, K-points grids for supercells were chosen in order to be as close as possible to the density of k-points corresponding to the 6x6x6 grid for the cubic MAPI unit-cell. A K-point offset or shift is implemented when necessary.

2.1.2 Theory of Positron and its annihilation for the study of vacancy defects

The concept of a positron was mathematically predicted by Dirac in 1928 [12, 13]. It comes from the term 'positive-electron' and refers to the elementary sub-atomic anti-particle of an electron. It has an mass equal to that of an electron, and an electrical charge that is equal in magnitude to the charge of an electron, but with opposite sign. These properties have been summarized in Table 2.1 to differentiate between the particles.

Table 2.1: Properties of an electron, a positron and a proton.

Particle	Symbol	Charge	Mass (kg)
Electron	e$^-$ β^-	-	9.1*10^{-31}
Positron	e$^+$ β^+	+	9.1*10^{-31}
Proton	p	+	1.67*10^{-27}

It was only after this theoretical prediction that the existence of a positron was experimentally confirmed in 1932 [14]. Positrons can be formed by a process called pair-production. In this process, a high energy photon such as a γ ray or a cosmic ray, interacts with matter to produce an electron-positron pair. The reverse of this pair-production or creation process is called annihilation. This mutual destruction of the electron with the positron occurs when they interact with each other, resulting in the release of energy in form of photons. These processes are represented using Feynman diagrams in Figure 2.5.

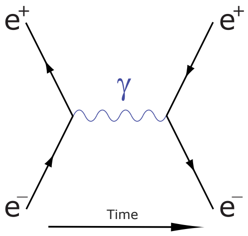

Figure 2.5: The Feynman diagram depicting the pair-production and annihilation process with time.

Positron annihilation spectroscopy (PAS) is an experimental, non-destructive nuclear technique used to study vacancy defects in materials. It can probe materials on the atomic scale to identify open volume or vacancy defects, determine their size, detect their concentration and identify their chemical environments. The process of positron generation and interaction with the solid material can be understood with the help of the Figure 2.6. First, the positron is generated by the beta decay of Na^{22} source according to the Equation 2.7. A γ ray of energy 1274 keV is also produced alongside. The positron sources generate and release positrons one at a time in a controlled manner and the time of observance of the γ ray, signaling the positron generation, is noted.

$$^{22}\mathrm{Na} \rightarrow {}^{22}\mathrm{Ne} + \mathrm{e}^{+} + \nu_{\mathrm{e}} + \gamma \tag{2.7}$$

The positron is then allowed to probe inside the material, where it thermalizes. Now there are two possibilities, 1) the positron could annihilate with an e^{-} in the bulk of the perfect lattice 2) the e^{+} could get trapped in a neutral or a negatively-charged vacancy defect and annihilate inside it. This e^{-}-e^{+} annihilation results in the emission of a pair of γ rays of energy 511 keV in the opposite direction following the laws of conservation. Finally, the time difference between the observation of the two γ rays of energy 1274 keV and 511 keV is recorded and called the Positron Annihilation Lifetime (PAL). It is assumed that the time taken for thermalization process is short compared to the positron lifetime. Now, the lifetime only depends on the overlap of the positron wavefunction with the surrounding electrons. This lifetime, denoted by τ, is recorded and used to deduce the properties of the positrons and the corresponding annihilated electrons of the material.

Given that the bulk of the material has a high electron density, the positron can annihilate more quickly and have a shorter lifetime. The positron, however, being positively charged, is drawn to a negatively charged vacancy and repelled by the atomic nuclei in the bulk. The trapped positron takes longer to annihilate at this site where the electrons are less abundant. As a result, the positron acts as a 'defect-seeker' [15].

There is another type of Positron annihilation spectroscopy, the Doppler Broadening PAS, which analyzes the broadening of the annihilation peak due to the Doppler shift caused by the momentum distribution of the annihilating electrons. This broadening provides information about the distribution of electron momenta, which in turn can reveal more details about the electronic structure and defects in materials. The line-shape parameter or the S-parameter is an important output of this technique. It is the ratio of the positrons annihilating with low-momentum electrons to the total number of annihilating electrons. Hence it has a direct proportional relation with the material's defect density.

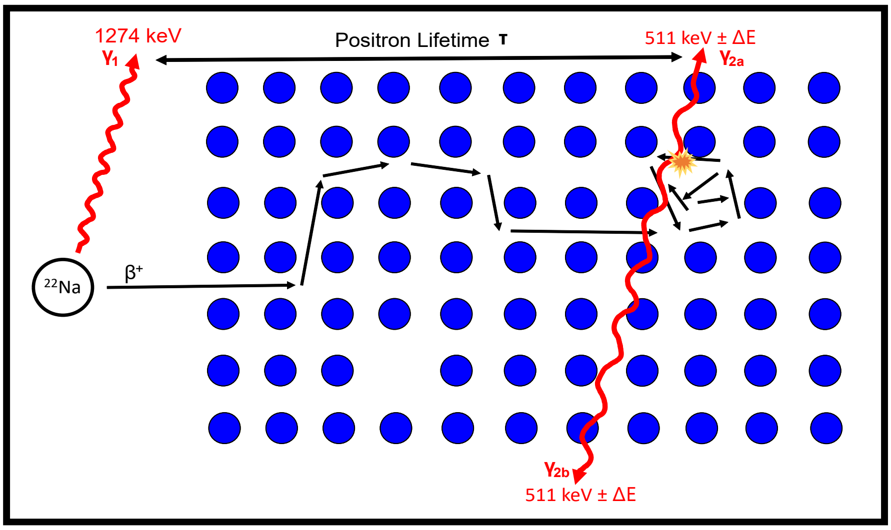

Figure 2.6: An illustration of the positron-solid interaction during the positron annihilation technique.

2.1.2.1 Theoretical aspects of PAL calculation

Here are some concepts needed for the calculation of positron annihilation lifetime.

- **Positron Potential:**

  The positron's potential is computed as the sum of Coulomb potentials due to the superimposed free atoms according to the Equation 2.8.

$$V_{+}(\mathbf{r}) \approx \sum_{\mathbf{R}} V_{\text{Coul}}^{\text{at}}\left(|\mathbf{r}-\mathbf{R}|\right)+V_{\text{corr}}\left(n_{-}(\mathbf{r})\right) \tag{2.8}$$

  where V_{corr} is the electron-positron correlation term calculated using local density approximation (LDA).

- **Positron annihilation rate:**

  The positron annihilation rate is given by the Equation 2.9 [16]

$$\lambda=\frac{1}{\tau}=\frac{\pi r_0^2 c}{e^2} \int d^3\mathbf{r} n^{+}(\mathbf{r}) n(\mathbf{r}) \gamma(n(\mathbf{r})) \tag{2.9}$$

  where λ is the positron annihilation rate and the inverse of the lifetime τ, r_0 is the classical electron radius, n and n^+ are the electronic and positronic charge densities respectively, c is the speed of light, and γ is the enhancement factor with the condition of zero positron density limit [17].

The positron's positive charge attracts electrons, increasing the mutual overlap and ultimately the annihilation rate between the two. This is taken into account by the enhancement factor. It is given by another Equation 2.10 [18, 16, 19]

$$\gamma = \frac{\lambda}{\lambda^{IPM}} \tag{2.10}$$

where IPM refers to an independent particle model that assumes the absence of correlation between the positron and the electron.

- **Positron binding energy:**

  The binding energy of a positron with a material provides information about the interaction between the positron and the surrounding electrons in the material. It is calculated by the Equation 2.11

$$\mathbf{E}_b = \mathbf{E}_+(bulk) - \mathbf{E}_+(defect) \tag{2.11}$$

  where E_b is the binding energy and E_+ represents the positron energy in the bulk and in the defective site respectively in the equation.

2.1.2.2 Practical aspects of calculations

For computation of the PAL, a software called ATSUP, formerly known as MIKA-DOPPLER, is used in conjunction with Quantum Espresso [20, 21, 22, 19, 8]. The flowchart in Figure 2.7 provides a comprehensive breakdown of the process. It is followed by a detailed step-wise explanation.

1. First, the input files containing the structural information about the system are prepared in the Quantum Espresso format.

2. Using the DFT approach as described in the previous section, a self-consistent electronic-structure calculation is done and the electronic charge density is obtained via post-processing.

   Alternatively, the electron density could be approximated as a superposition of densities of neutral free atoms according to the Equation 2.12 using ATSUP. A comparison of these two methods has also been done in this thesis.

$$n_-(\mathbf{r}) \approx \sum_{\mathbf{R}} n_-^{\mathrm{at}}(|\mathbf{r} - \mathbf{R}|) \tag{2.12}$$

3. After the electronic charge density, the positronic charge density needs to be evaluated. This is done via ATSUP using two-component DFT [23, 20]. This is done according to Equation 2.8.

4. The rate of positron annihilation can be determined by considering the electronic and positronic charge densities calculated henceforth, using the Equation 2.9.

   The enhancement factor is generally treated as a function of electron density in LDA, which underestimates the positron lifetime [16]. To tackle this, we use α=0.22 to interpolate the enhancement factor as derived by [24] using the results from Arponen and Pajanne [24, 25]. Alpha parameter is an adjustable parameter that takes into account the electron-positron exchange correlation. It is obtained by fitting the positron annihilation lifetime with a sum of exponential decay functions according to the Equation 2.13 [24, 25].

   $$\gamma_{GGA} - 1 = (\gamma_{LDA} - 1)e^{(-\alpha\epsilon)} \tag{2.13}$$

   where γ_{GGA} and γ_{LDA} are the GGA and LDA enhancement factors, respectively. ϵ describes the effects of non-uniform electron density and is calculated by Equation 2.14. Here, n is the electron density and q$_{TF}$ is local Thomas-Fermi screening length [26].

   $$\varepsilon = \left| \frac{\nabla n(r)}{n(r) q_{\mathrm{TF}}(r)} \right|^2 \tag{2.14}$$

5. In the final step, the positron annihilation rate which is inverse of the positron annihilation lifetime, is calculated according to the Equation 2.9. It is important to note that the positron annihilation lifetime is typically measured in picoseconds, and the same unit of measurement has been employed consistently throughout this thesis.

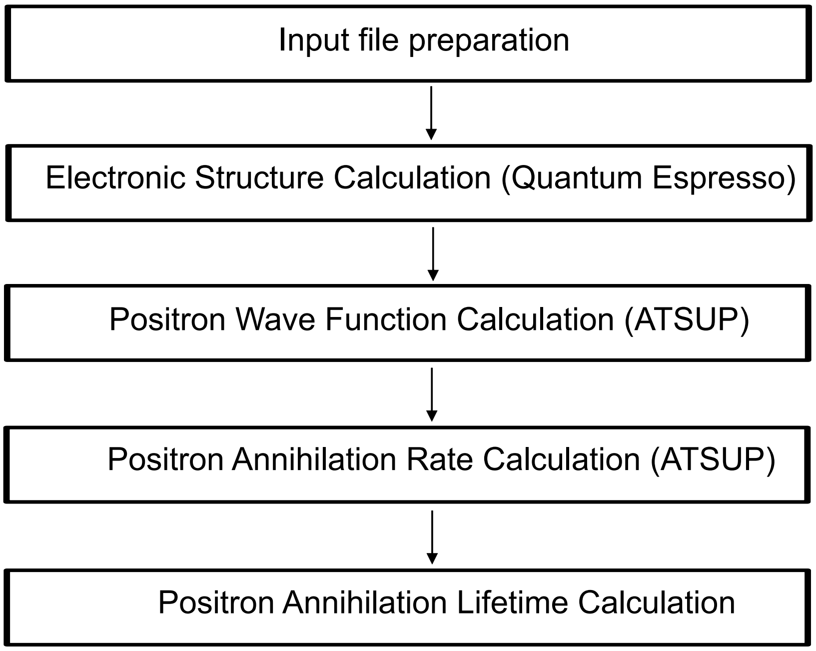

Figure 2.7: A comprehensive outline of the positron annihilation lifetime calculation procedure, using ATSUP and Quantum Espresso, in a flowchart.

2.2 Structural analysis

In this section, we will discuss the concepts required for the structural analysis and vacancy defect characterization.

2.2.1 Glazer notations

Glazer studied the tiltings in the inorganic octahedra of perovskites in general [27, 28]. These are represented by the so-called Glazer notations. A crystallographic system can have different tiltings and hence different Glazer notations. The rules for these notations are:

- It is denoted using 3 characters (a, b ,c) corresponding to each of the crystallographic directions.
- If the amplitude of tilting is same in any two directions, the same character is used for both the directions.
- Each character has a superscript (0,+,-) that indicates whether or not the tilt is present and, if so, what type. The superscript 0 represents that no tilting is present, while +/- point towards tilting. A '+' tilt means an in-phase tilting in which the one octahedral layer appears to eclipse the other in that direction. Whereas, a - tilt means out-of-phase or anti-phase tilting where no octahedral layer appears to be eclipsed by the other.

There are overall 23 possible tilt systems [27]. Some of these are depicted in Figure 2.8 and Table 2.2 with the corresponding Glazer notations.

Table 2.2: : Table for the Glazer notations of some common tilting systems in perovskites. The crystal systems referred in table are **C**ubic, **T**etragonal and **O**rthorhombic. These tiltings can only be realized in larger than minimal cells as described in the subsequent table. The systems are pictorially represented in the subsequent Figure 2.8.

	Glazer Notation	Crystal System	Unit Cell
a	$a^0a^0a^0$	C	111
b	$a^0a^0c^+$	T	$\sqrt{2}\,\sqrt{2}\,1$
c	$a^0a^0c^-$	T	$\sqrt{2}\,\sqrt{2}\,2$
d	$a^+a^+a^+$	C	2 2 2
e	$a^+b^-b^-$	O	$\sqrt{2}\,\sqrt{2}\,2$

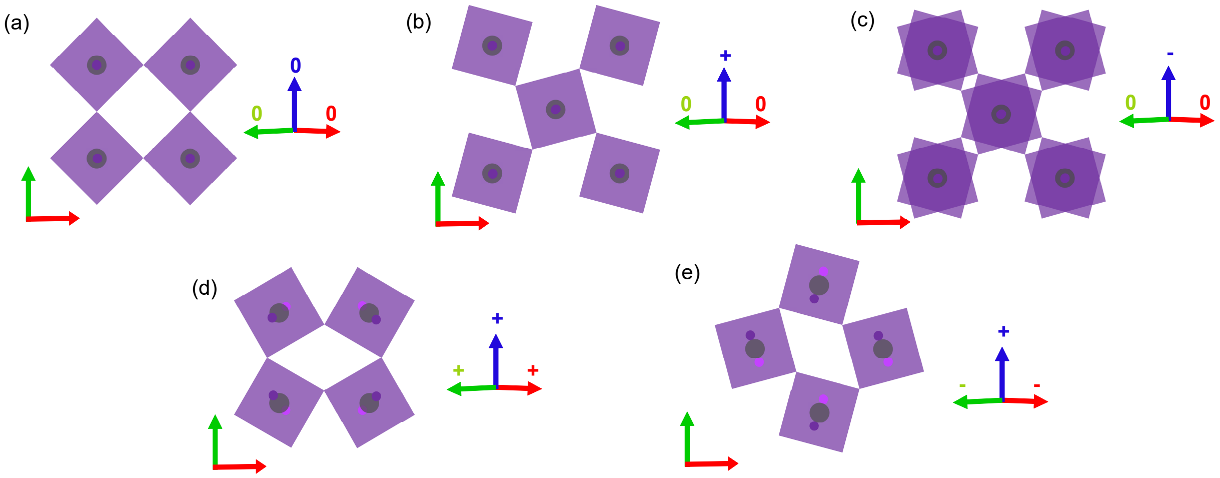

Figure 2.8: Perovskite systems with different tiltings in the inorganic octahedra with Glazer Notation corresponding to the Table 2.2. The inorganic octahedra of iodine is represented in shades of pink, Pb in Grey and the A cation is omitted for convenience. The x, y, z axis are represented in red, green and blue, respectively along with '+' and '-' for tiltings.

Although these notations are useful for describing tiltings in perovskites and differentiating the various phases, they have certain drawbacks.

- They give no information about the magnitude of tilting.
- Glazer Notations were devised for perovskites in general. Hence, only the inorganic cage was taken into consideration in these notations, leaving out the A cation which could be either organic or inorganic. When the A cation is multi-atomic, it could have multiple orientations inside the octahedral cage. Also, it is believed to have an influence on the tilting in the inorganic cage [29, 30, 31].
- It cannot distinguish between the different polytypes of hybrid organic-inorganic perovskites, for instance between different polytypes of the tetragonal form of MAPbI$_3$ reported previously [31]. Here, the term polytype is used in a broader context to describe a different orientation of the organic molecule within the same crystallographic system.

In the thesis, Glazer Notations corresponding to the 8 formula unit systems is provided unless otherwise indicated.

2.2.2 Pair Distribution Function

The pair-distribution function (PDF) is an analytical tool used to determine the local structure of materials on an atomic scale. It is a measure of the probability of finding two atoms separated by a certain distance in a particular crystal structure. In a perfect crystal system, the distance between different atom types remains constant (except for the small variations due to lattice vibrations), resulting in clear and sharp vertical lines in the pair distribution function plot. In contrast, in an amorphous material, the arrangement of atoms lacks long-range order, and the distance between atomic pairs have a wider range. As a result, the peak in the pair correlation function plot is broad and continuous without well-defined peaks or valleys, indicating a distribution of distances to the nearest neighbors. Therefore, the PDF analysis can help in characterizing the degree of order or disorder in a material. It can be experimentally obtained using X-ray diffraction techniques to reveal information about long/short-range ordering and local-disorder in a crystal system. This kind of analysis has already been used previously for studying perovskites computationally as well as experimentally [7, 32, 33].

The experimental PDF is obtained by the fourier transformation of the total scattering structure function S(Q). This is given by the Equation 2.15:

$$G(r) = \frac{2}{\pi} \int_{Q_{min}}^{Q_{max}} Q[S(Q) - 1] \sin(Qr) dQ \tag{2.15}$$

where Q_{min} and Q_{max} are integration limits depending on the experimental setup.

The PDFgui software is employed for static PDF analysis in this work [34]. It uses the provided atomic coordinates of the model structures and plots the PDF according to the Equation 2.16.

$$G(r) = \frac{1}{rN} \sum_{i,j\neq i}^{N} \frac{f_i^* f_j}{\langle f \rangle^2} \delta\left(r - r_{ij}\right) - 4\pi r \rho_0 \tag{2.16}$$

where N is the number of atoms, ρ_0 is the average atomic-pair density of the material, r is the radial distance, and f_i is the scattering factor of atom i [35, 34].

The experimental resolution parameters for plot refining were taken from [7, 32]. Q$_{damp}$ refers to the Gaussian dampening envelope due to limited Q-resolution and Q$_{broad}$ is the peak broadening from increased intensity noise at high Q. The peak width is calculated as given in Equation 2.17:

$$\sigma_{ij} = \sigma'_{ij}\sqrt{1 - \frac{\delta_1}{r_{ij}} - \frac{\delta_2}{r_{ij}^2} + Q_{broad}^2 r_{ij}^2} \tag{2.17}$$

where σ is the final width and σ' is the width without correlation computed using U_{ii} which describe atomic displacements due to thermal effect. The values of Q$_{damp}$ and Q$_{broad}$ are 0.0434148 and 0.0164506, respectively, obtained by experimental calibration [32, 34]. A uniform isotropic parameter U_{ii} = 0.01 Å^2 is used for all the atoms.

2.2.3 Minimum Energy Paths for transitions

The activation energies for phase transformation were calculated using Nudged Elastic Band (NEB) method in conjunction with the climbing image method in Quantum Espresso [36, 8]. This method finds the saddle points in the potential energy surface between a given initial and final configuration and a set of intermediate configurations (images) connecting them. It requires the calculation of only the first gradient of energy and it can achieve a good computational efficiency by taking advantage of image parallelization.

The NEB method requires the energy-optimized initial and final configurations to be specified. Intermediate configurations to direct the minimum-energy-path are usually optional but sometimes required to enforce the valley of the potential energy surface in which to search the minimum energy path. Using linear interpolation, multiple equidistant intermediate images are generated that are connected by springs to simulate an elastic band. After that, the band is optimized to minimize the forces acting on each image. This is done in such a way that the spring forces do not interfere with elastic band convergence and the potential force does not affect image distribution along the minimum energy path, thus avoiding the corner cutting and sliding down problems seen in other elastic band methods [37, 36, 38]. During minimization, the potential and spring forces are decomposed, and only the component parallel to the direction of the spring force with the perpendicular component of the potential force are included to the calculated of the force projection, which is known as nudging. This decouples the forces to achieve the minimum energy path easier. The spacing between images is then only controlled by the spring forces while the potential forces drive the images towards the minima. Hence, the total force acting on an image i is given by the sum of spring forces along the local tangent and potential forces perpendicular to it as given in Equation 2.18

$$\mathbf{F}_i = \mathbf{F}_i^{p,\perp} + \left(\mathbf{F}_i^{\mathrm{s}} \cdot \hat{\tau}_i\right)\hat{\tau}_i \tag{2.18}$$

Here, τ_i is the normalized local tangent, $\mathbf{F}_i^{p,\perp}$ denotes the perpendicular potential forces acting along the path. The last term $\mathbf{F}_i^{\mathrm{s},\|}$ denotes the spring forces acting parallel to the path τ_i. For such an elastic band with N+1 images denoted by [R_0, R_1, R_2...R_N] and connected by a springs with a spring constant k, these forces minimize the energy of the intermediate images. The potential force is calculated as the gradient of energy with respect to the atomic coordinates of image i. Then its perpendicular component can be obtained by subtracting out the parallel component. The spring force can be evaluated by using the Equation 2.19:

$$\mathbf{F}_i^{\mathrm{s},\|} = \left(k_i^{\mathrm{s}} \left|\mathbf{R}_{i+1} - \mathbf{R}_i\right| - k_{i-1}^{\mathrm{s}} \left|\mathbf{R}_i - \mathbf{R}_{i-1}\right|\right) \hat{\boldsymbol{\tau}}_i \tag{2.19}$$

When the number of images are not enough to describe the energy profile along the path, the saddle point obtained may be lower than the actual one due to poor resolution [39]. So, to locate it accurately, the climbing-image NEB (CI-NEB) method is used in which the highest image, also called the climbing image, takes a distinctive jump. The forces acting on this particular image are given by Equation (2.20) where the total force is the potential force, with the spring forces on either side on the climbing images excluded from it. The parallel component of this potential force $\mathbf{F}_{i_{max}}^{p}$ shifts the climbing image uphill while the perpendicular force pushes it downhill along the path.

$$\mathbf{F}_{i_{max}} = \mathbf{F}_{i_{max}}^{p} - 2\left(\mathbf{F}_{i_{max}}^{p} \cdot \hat{\tau}_{i_{max}}\right) \hat{\tau}_{i_{max}} \tag{2.20}$$

The CI is independent of the spring forces, allowing different spacing with the adjacent images. Generally, it is turned on only after converging a normal NEB calculation to avoid highest image identification problems.

This rule for CI was followed for the calculations done using neb.x program within quantum espresso. The number of images were chosen to keep the inter-image distance less than 2 Bohr and intermediate images were specified when necessary to direct the path. Default values for the spring constants were used. The path_thr keyword for the convergence threshold on forces was given the value of 0.1 eV/Å.

2.3 Defect Thermodynamics and characterization

In this section, we will discuss the concepts required to understand the vacancy defects at the atomic level using DFT.

2.3.1 Chemical potentials

The thermodynamic stability of MAPbI$_3$ can be judged from an ab-initio perspective using the thermodynamic stability diagrams which take into account the chemical potentials of the involved species. The formation enthalpies are calculated as the difference of total energy of individual components when they come together to form a compound. This is based on the constraints given in equations 2.21 to 2.23. The total energy calculations are done with LDA, GGA (PAW) and GGA(US) pseudopotentials as described in the previous chapter. The chemical potential of constitutive elements is referenced to their respective most stable phase which are: orthorhombic I$_2$ molecular crystal [40], hexagonal PbI$_2$ [41] and Pb bulk metal in fcc crystal structure. A cutoff of 80 Ry was chosen for LDA and GGA (PAW) and 70 Ry for OptB86-vdw (US) after convergence tests. The following inequality equations are followed:

$$\mu_{\mathrm{CH_3NH_3}} + \mu_{\mathrm{Pb}} + 3\mu_I = \Delta H\left(\mathrm{CH_3NH_3PbI_3}\right) \tag{2.21}$$

$$\mu_{\mathrm{CH_3NH_3}} + \mu_I < \Delta H\left(\mathrm{CH_3NH_3I}\right) \tag{2.22}$$

$$\mu_{Pb} + 2\mu_I < \Delta H\left(PbI_2\right) \tag{2.23}$$

where the chemical potentials of I and Pb have been referenced to that of I$_2$ molecule and Pb bulk metal, respectively. These are plotted in Figure 2.9 and the corresponding formation enthalpy values calculated are given in Table 2.3.

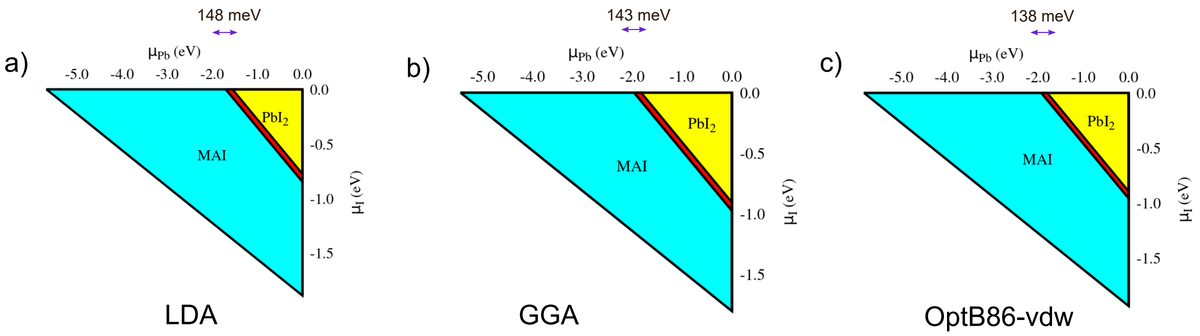

Figure 2.9: Thermodynamic Stability Diagrams of the cubic unit cell of $MAPbI_3$ using LDA, GGA and OptB86-vdw functionals. The stability region of $MAPbI_3$ is represented by the narrow red stripe.

Table 2.3: Table for the formation enthalpy of the different inequality equations 2.21-2.23 using LDA, GGA and OptB86-vdw. Besides, GGA and LDA calculated values from references are taken for comparison.

Reactions	Formation enthalpies				
	LDA	GGA	OptB86-vdw	LDA Ref. [42]	GGA Ref. [43]
$Pb+I_2 \rightleftharpoons PbI_2$	-1.7	-1.96	-1.92	-1.84	-2.11
$MA + \frac{1}{2} I_2 \rightleftharpoons MAI$	-4.13	-4.02	-4.03	-3.05	-2.87
$MA+Pb+ \frac{3}{2} I_2 \rightleftharpoons MAPbI_3$	-5.68	-5.84	-5.82		-5.26
$MAI+PbI_2 \rightleftharpoons MAPbI_3$	-0.15	-0.14	-0.14	-0.014	-0.27

2.3.2 Defect Formation Energies

To study the vacancy defects in MAPbI$_3$, defect formation energy is calculated. Defect Formation Energy (DFE) refers to the amount of energy required to create a vacancy defect in a perfect crystal. The defect formation energy of a defect X having a charge q, at a chemical potential μ is given by the formula in Equation 2.24 [44].

$$\mathrm{DFE}(X^q,\mu) = E\left(X^q\right) - E_{perf} - \sum_i n_i\mu_i + q\left(E_\mathrm{F} + VBM + \Delta V\right) \quad + E^q_{corr} \tag{2.24}$$

where

E(X^q) = Energy of the defected system with charge q

E$_{perf}$ = Energy of the perfect system

n$_i$=number of vacancies of species i in the defected cell

E$_F$ = Fermi energy

V = Electrostatic potential referred to valence band minimum

E$^q{}_{corr}$ = correlation energy between defects

The first and second terms represent the energy of the defected and pristine system, respectively. The third term accounts for the change in chemical potential of the system, with n being negative for a vacancy. The fourth term accounts for the exchange of electrons with the Fermi level and correction for the electrostatic potential due to the defect charge. The last term E$^q{}_{corr}$ is image-charge correction term that accounts for the spurious long-range electrostatic interactions between the periodic defects images [45, 43, 46, 47]. This last term has not been included in the calculation of defect formation energy values provided in this thesis. These are represented in Figure 2.10.

$$\text{DFE}\,(X^q, \mu) \quad = \quad E\,(X^q) \; - \; E_{perf} \quad - \quad \Sigma\, n_i \mu_i \quad + \quad q(E_F + V + \Delta V) \quad + \quad E_{corr}$$

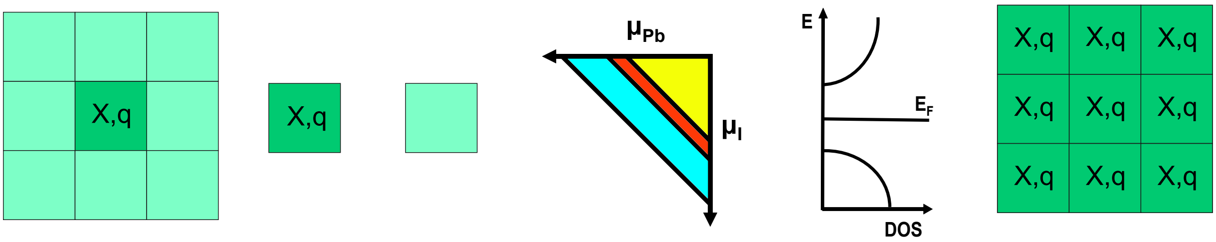

Figure 2.10: A pictorial representation of the defect formation energy calculation in a defective system. The defect formation energy equation above correlates with the picture below.

2.3.3 Voronoi volumes

Positron annihilation spectroscopy is governed by interactions between the positron and the surrounding electronic system. The overlap between the electronic and positronic wave-functions at a vacancy defect site is smaller compared to the bulk. This increases the positron annihilation lifetime. The larger is the size of defect site, the smaller will be the electron-positron overlap and the larger will be the lifetime. Hence, the positron lifetime is a measure of the size of the vacancy [48]. To study this size, that gives an indication of the positron annihilation lifetime, we use the concept of Voronoi volumes. Voronoi Volume encloses the region around a lattice site where every point that belongs to this region is closer to that particular lattice site than to any other site. If we consider a set of particles p (p$_i$, p$_j$ $\in$ p), then any point P lies in the voronoi region of p$_i$ if its distance from point p$_i$ is less than its distance from any other point p$_j$. This is represented in Equation 2.25.

$$\mathbf{P} \in \mathbf{R}^3, \qquad \mathbf{V}(\mathbf{p_i}) = \mathbf{P}|\mathbf{d}(\mathbf{p_i}, \mathbf{P}) \leq \mathbf{d}(\mathbf{p_j}, \mathbf{P}) \qquad \forall \mathbf{p_j} \in \mathbf{p} \tag{2.25}$$

The computation of this volume in three-dimensions is done using the Voro++ library incorporated in Ovito [49, 50]. Based on the particle positions, this library divides the system into several polyhedrons for the voronoi region. This is done by taking the perpendicular bisector of the line connecting the neighbouring atoms. The volume of each of these polyhedrons gives the voronoi volume associated with each particle. It can also be used to compute and produce the voronoi cell associated with a specific particle as shown in Figure 2.11. For finding the voronoi volume associated with a vacancy defect, the system is relaxed before adding a dummy atom in the defect cavity to calculate the Voronoi Volume. It is then maximized by utilizing a grid based approach that involves shifting of the dummy atom by 0.1 Å in each direction.

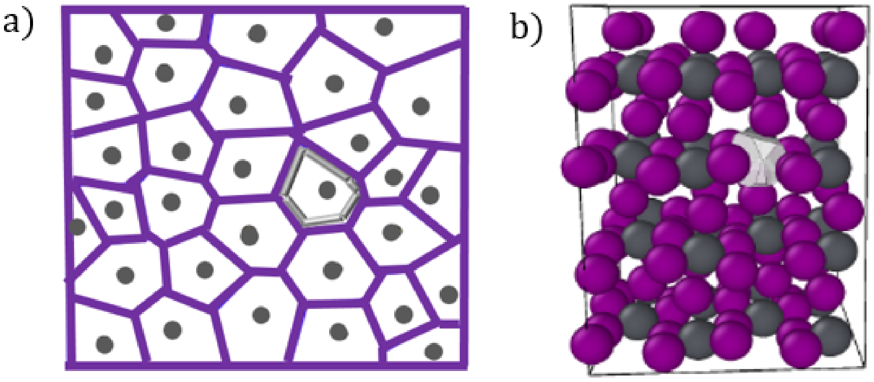

Figure 2.11: A representation of Voronoi Volumes in a) a simplistic 2D model. The grey circles represent a set of particles. These are divided by the purple network into polygonal regions and the volume of these polygons is the Voronoi Volume. b) 3D diagram of $MAPbI_3$ containing a Pb vacancy. The Voronoi Volume for Pb vacancy is highlighted by a polygon. The colors grey and purple represent Pb and I respectively. MA^+ are hidden for visual convenience.

REFERENCES

[1] Jean-Michel Combes, Pierre Duclos, and Ruedi Seiler. The born-oppenheimer approximation. *Rigorous atomic and molecular physics*, pages 185–213, 1981. pages 41

[2] Pierre Hohenberg and Walter Kohn. Inhomogeneous electron gas. *Physical review*, 136(3B):B864, 1964. pages 42

[3] Walter Kohn and Lu Jeu Sham. Self-consistent equations including exchange and correlation effects. *Physical review*, 140(4A):A1133, 1965. pages 42

[4] Feliciano Giustino. *Materials modelling using density functional theory: properties and predictions*. Oxford University Press, 2014. pages 7, 42, 44, 45

[5] Julien Toulouse. Review of approximations for the exchange-correlation energy in density-functional theory. *arXiv preprint arXiv:2103.02645*, 2021. pages 43

[6] Jiří Klimeš, David R Bowler, and Angelos Michaelides. Van der waals density functionals applied to solids. *Physical Review B*, 83(19):195131, 2011. pages 43

[7] Xin-Gang Zhao, Gustavo M Dalpian, Zhi Wang, and Alex Zunger. Polymorphous nature of cubic halide perovskites. *Physical Review B*, 101(15):155137, 2020. pages 43, 56, 57

[8] Paolo Giannozzi, Stefano Baroni, Nicola Bonini, Matteo Calandra, Roberto Car, Carlo Cavazzoni, Davide Ceresoli, Guido L Chiarotti, Matteo Cococcioni, Ismaila Dabo, et al. Quantum espresso: a modular and open-source software project for quantum simulations of materials. *Journal of physics: Condensed matter*, 21(39):395502, 2009. pages 45, 51, 58

[9] Andrea Dal Corso. *Density-functional theory beyond the pseudopotential local density approach: a few cases studies*. PhD thesis, SCUOLA INTERNAZIONALE SUPERIORE DI STUDI AVANZATI, 1993. pages 46

[10] Shigeji Fujita, Kei Ito, Shigeji Fujita, and Kei Ito. Bloch theorem. *Quantum Theory of Conducting Matter: Newtonian Equations of Motion for a Bloch Electron*, pages 85–95, 2007. pages 46

[11] Hendrik J Monkhorst and James D Pack. Special points for brillouin-zone integrations. *Physical review B*, 13(12):5188, 1976. pages 47

[12] Paul Adrien Maurice Dirac. The quantum theory of the electron. *Proceedings of the Royal Society of London. Series A, Containing Papers of a Mathematical and Physical Character*, 117(778):610–624, 1928. pages 48

[13] Paul Adrien Maurice Dirac. The quantum theory of the electron. part ii. *Proceedings of the Royal Society of London. Series A, Containing Papers of a Mathematical and Physical Character*, 118(779):351–361, 1928. pages 48

[14] Carl D Anderson. Energies of cosmic-ray particles. *Physical Review*, 41(4):405, 1932. pages 48

[15] Julia Wiktor. *Identification of equilibrium and irradiation-induced defects in nuclear ceramics: electronic structure calculations of defect properties and positron annihilation characteristics*. PhD thesis, Aix-Marseille Université, 2015. pages 49

[16] Bernardo Barbiellini. Positron states in materials: DFT and QMC studies. *New Directions in Antimatter Chemistry and Physics*, pages 127–150, 2001. pages 50, 51, 52

[17] Martti J Puska and Risto M Nieminen. Theory of positrons in solids and on solid surfaces. *Reviews of modern Physics*, 66(3):841, 1994. pages 50

[18] PA Sterne and JH Kaiser. First-principles calculation of positron lifetimes in solids. *Physical Review B*, 43(17):13892, 1991. pages 51

[19] Ilja Makkonen, M Hakala, and Martti J Puska. Modeling the momentum distributions of annihilating electron-positron pairs in solids. *Physical Review B*, 73(3):035103, 2006. pages 51

[20] MJ Puska and RM Nieminen. Defect spectroscopy with positrons: a general calculational method. *Journal of Physics F: Metal Physics*, 13(2):333, 1983. pages 51, 52

[21] Tuomas Torsti, M Heiskanen, MJ Puska, and RM Nieminen. Mika: Multigrid-based program package for electronic structure calculations. *International journal of quantum chemistry*, 91(2):171–176, 2003. pages 51

[22] Filip Tuomisto and Ilja Makkonen. Defect identification in semiconductors with positron annihilation: Experiment and theory. *Reviews of Modern Physics*, 85(4):1583, 2013. pages 51

[23] E Boroński and RM Nieminen. Electron-positron density-functional theory. *Physical Review B*, 34(6):3820, 1986. pages 52

[24] B Barbiellini, Martti J Puska, T Korhonen, A Harju, T Torsti, and Risto M Nieminen. Calculation of positron states and annihilation in solids: A density-gradient-correction scheme. *Physical Review B*, 53(24):16201, 1996. pages 52

[25] J Arponen and E Pajanne. Electron liquid in collective description. iii. positron annihilation. *Annals of Physics*, 121(1-2):343–389, 1979. pages 52

[26] Edward Boroński. Positron lifetime calculations for some elements on the base of the ggaphnc approximation. *Nukleonika*, 55:9–12, 2010. pages 52

[27] Anthony M Glazer. The classification of tilted octahedra in perovskites. *Acta Crystallographica Section B: Structural Crystallography and Crystal Chemistry*, 28(11):3384–3392, 1972. pages 54

[28] Fazel Shojaei and Wan-Jian Yin. Stability trend of tilted perovskites. *The Journal of Physical Chemistry C*, 122(27):15214–15219, 2018. pages 54

[29] Jingrui Li and Patrick Rinke. Atomic structure of metal-halide perovskites from first principles: The chicken-and-egg paradox of the organic-inorganic interaction. *Physical Review B*, 94(4):045201, 2016. pages 55

[30] Jonathan Lahnsteiner, Georg Kresse, Abhinav Kumar, DD Sarma, Cesare Franchini, and Menno Bokdam. Room-temperature dynamic correlation between methylammonium molecules in lead-iodine based perovskites: An ab initio molecular dynamics perspective. *Physical Review B*, 94(21):214114, 2016. pages 55

[31] Wen-Yi Tong, Jin-Zhu Zhao, and Philippe Ghosez. Missed ferroelectricity in methylammonium lead iodide. *npj Computational Materials*, 8(1):165, 2022. pages 55

[32] Alexander N Beecher, Octavi E Semonin, Jonathan M Skelton, Jarvist M Frost, Maxwell W Terban, Haowei Zhai, Ahmet Alatas, Jonathan S Owen, Aron Walsh, and Simon JL Billinge. Direct observation of dynamic symmetry breaking above room temperature in methylammonium lead iodide perovskite. *ACS energy Letters*, 1(4):880–887, 2016. pages 56, 57

[33] Xiangzhou Zhu, Sebastián Caicedo-Dávila, Christian Gehrmann, and David A Egger. Probing the disorder inside the cubic unit cell of halide perovskites from first-principles. *ACS Applied Materials & Interfaces*, 14(20):22973–22981, 2022. pages 56

[34] CL Farrow, P Juhas, JW Liu, D Bryndin, ES Božin, J Bloch, Th Proffen, and SJL Billinge. Pdffit2 and pdfgui: computer programs for studying nanostructure in crystals. *Journal of Physics: Condensed Matter*, 19(33):335219, 2007. pages 56, 57

[35] João Batista Souza Junior, Gabriel Ravanhani Schleder, Jefferson Bettini, Icamira Costa Nogueira, Adalberto Fazzio, and Edson Roberto Leite. Pair distribution function obtained from electron diffraction: an advanced real-space structural characterization tool. *Matter*, 4(2):441–460, 2021. pages 56

[36] Graeme Henkelman, Blas P Uberuaga, and Hannes Jónsson. A climbing image nudged elastic band method for finding saddle points and minimum energy paths. *The Journal of chemical physics*, 113(22):9901–9904, 2000. pages 58

[37] Hannes Jónsson, Greg Mills, and Karsten W Jacobsen. Nudged elastic band method for finding minimum energy paths of transitions. In *Classical and quantum dynamics in condensed phase simulations*, pages 385–404. World Scientific, 1998. pages 58

[38] Daniel Sheppard and Graeme Henkelman. Paths to which the nudged elastic band converges. *Journal of computational chemistry*, 32(8):1769–1771, 2011. pages 58

[39] Vilhjálmur Ásgeirsson, Benedikt Orri Birgisson, Ragnar Bjornsson, Ute Becker, Frank Neese, Christoph Riplinger, and Hannes Jónsson. Nudged elastic band method for molecular reactions using energy-weighted springs combined with eigenvector following. *Journal of Chemical Theory and Computation*, 17(8):4929–4945, 2021. pages 59

[40] Federica Bertolotti, Anastasia V Shishkina, Alessandra Forni, Giuliana Gervasio, Adam I Stash, and Vladimir G Tsirelson. Intermolecular bonding features in solid iodine. *Crystal growth & design*, 14(7):3587–3595, 2014. pages 60

[41] B Pałosz and E Salje. Lattice parameters and spontaneous strain in ax2 polytypes: Cdi2, pbi2 sns2 and snse2. *Journal of Applied Crystallography*, 22(6):622–623, 1989. pages 60

[42] Arthur Marronnier. *Anharmonicity and Instabilities in Halide Perovskites for Last Generation Solar Cells*. PhD thesis, Université Paris-Saclay (ComUE), 2018. pages 61

[43] Wan-Jian Yin, Tingting Shi, and Yanfa Yan. Unusual defect physics in ch3nh3pbi3 perovskite solar cell absorber. *Applied Physics Letters*, 104(6):063903, 2014. pages 61, 62

[44] Christoph Freysoldt, Blazej Grabowski, Tilmann Hickel, Jörg Neugebauer, Georg Kresse, Anderson Janotti, and Chris G Van de Walle. First-principles calculations for point defects in solids. *Reviews of modern physics*, 86(1):253, 2014. pages 62

[45] Daniele Meggiolaro, Silvia G Motti, Edoardo Mosconi, Alex J Barker, James Ball, Carlo Andrea Riccardo Perini, Felix Deschler, Annamaria Petrozza, and Filippo De Angelis. Iodine chemistry determines the defect tolerance of lead-halide perovskites. *Energy & Environmental Science*, 11(3):702–713, 2018. pages 62

[46] Xie Zhang, Jimmy-Xuan Shen, Mark E Turiansky, and Chris G Van de Walle. Minimizing hydrogen vacancies to enable highly efficient hybrid perovskites. *Nature Materials*, 20(7):971–976, 2021. pages 62

[47] Anuj Goyal, Prashun Gorai, Haowei Peng, Stephan Lany, and Vladan Stevanović. A computational framework for automation of point defect calculations. *Computational Materials Science*, 130:1–9, 2017. pages 62

[48] J de Vries. *Positron lifetime technique with applications in materials science*. PhD thesis, Technische Univ. Delft, 1987. pages 64

[49] Alexander Stukowski. Visualization and analysis of atomistic simulation data with ovito–the open visualization tool. *Modelling and simulation in materials science and engineering*, 18(1):015012, 2009. pages 64

[50] Chris Rycroft. Voro++: A three-dimensional voronoi cell library in c++. Technical report, Lawrence Berkeley National Lab.(LBNL), Berkeley, CA (United States), 2009. pages 64

Chapter 3

On phase stability and structural transformations in MAPbI$_3$ perovskite

> If you want to find the secrets of the universe, think in terms of energy.
>
> Nikola Tesla

Within the confines of this chapter, we contribute to the understanding of the detailed analysis of the structural and bonding characteristics inherent to distinct phases of MAPbI$_3$. By introducing a fresh array of potential configurations previously unexplored, we present the complex energy landscape underlying this material. Subsequent to this, we make an attempt to understand the atomic scale mechanisms driving the transition between the tetragonal and cubic phases, which happens at the operating temperature of the material, using NEB calculations between the new proposed configurations.

3.1 Structural overview of pristine perovskites

Several hybrid organic/inorganic perovskite-structured solar cells are based on methylammonium lead iodide (CH$_3$NH$_3$PbI$_3$, or MAPbI$_3$), which exists in three phases depending on the temperature: Orthorhombic (O), Tetragonal (T) and Cubic (C), each arising sequentially with ascending temperatures. These phases unveil their individual symphonies of structural configurations, each accompanied by a unique set of characteristics that contribute to the overall performance and behavior of the solar cell.

3.1.1 Orthorhombic phase

Below a temperature of 160 K [1, 2], MAPbI$_3$ adopts an orthorhombic crystal structure with space group Pnma. It is classified by the Glazer notation $a^-b^-c^+$ [3] using the 8 formula unit system (96 atoms). In this phase, octahedral rotations exhibit an intriguing pattern: they occur in-phase about the c-axis and out-of-phase along the a and b axes. Notably, this orthorhombic configuration represents the most thermodynamically stable state of the material at this temperature range.

A distinguishing feature of this phase is the restricted molecular rotations, which predominantly manifest along the [101] and [10$\bar{1}$] directions in the unit cell (4 formula units or 48 atoms) [4].

3.1.2 Tetragonal phase and its Polymorphs

Increasing the temperature of MAPbI$_3$ perovskite above 160K induces a transformation into its tetragonal phase [1, 2]. In this state, the tilting of the inorganic cage subsides along only two directions, leading to the Glazer notation $a^0a^0c^-$ [3] to describe its structural arrangement. The orientation of the organic molecules remains fixed along the <101> directions.

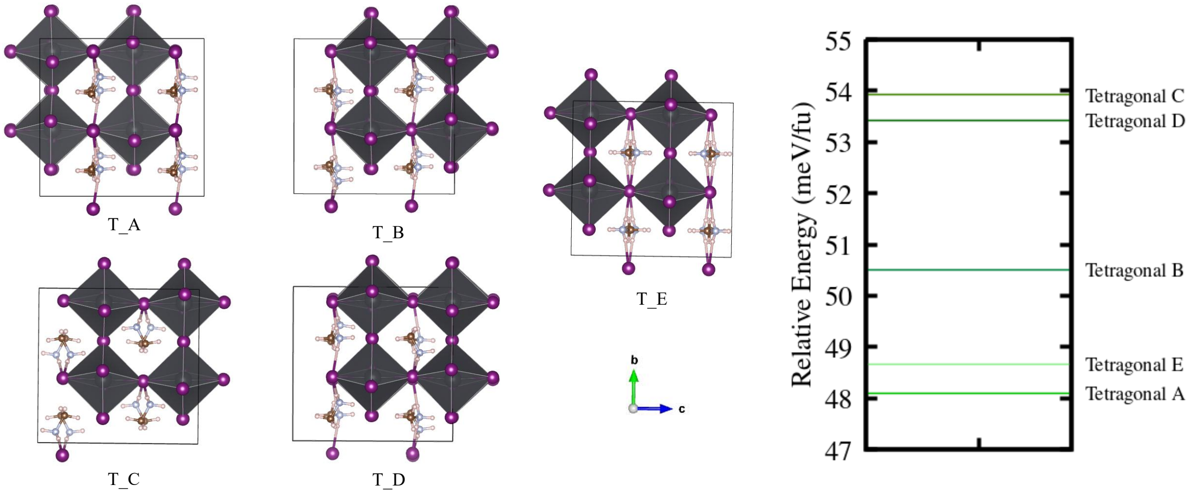

Figure 3.1: On the left, various configurations of the tetragonal polymorphs in the $MAPbI_3$ perovskite structure are depicted. The right side illustrates the relative energy plot in meV per formula unit with respect to the orthorhombic phase, showcasing the energy differences. Hydrogen bond interactions are depicted using a visualization tool- Vesta, with a cutoff distance of 2.8 Å considered for bond formation.

Recent research conducted by the Ghosez group [5] has unveiled numerous polymorphs of this phase. These variations manifest in the positioning of the organic molecules while maintaining a consistent connection pattern between the organic and inorganic components. The polymorphs are depicted in Figure 3.1 along with the energy landscape plot. The orientations of the organic molecule are all in <101> directions [5]. Despite sharing a common energy range of approximately 6 meV/formula unit, these polymorphs exhibit diverse features. These distinctions encompass discrepancies in organic molecular orientation and the coupled extent of tiltings within the inorganic cage. As a result, the possibility of spontaneous inter-conversion among these polymorphs through thermal fluctuations might be limited.

The Hydrogen atoms connected to Nitrogen (H_N) are oriented towards the Iodine atoms in the (100) plane, establishing a weak bonding interaction that serves as a connection bridging the inorganic and organic constituents. This arrangement imparts a distinct character to the system, resembling a two-dimensional layered structure. Within this structure, consecutive layers consist of alternating MAI and PbI_6 octahedral arrangements are present in the (100) plane, as illustrated in Figure 3.1. Hence we can say that, in the tetragonal system, only the Iodines in the MAI layer are connected to H_N via Hydrogen bonding.

3.1.3 Cubic unit cell

When raising the temperature above 327 K [1, 2], MAPbI$_3$ adopts the cubic phase. In a perfect perovskite cubic structure, centrosymmetry prevails, characterized by a Glazer notation a^{0}a^{0}a^0 that signifies an absence of distortion in the PbI$_6$ octahedra. However, the presence of organic molecules disrupts this pristine symmetry. The polar nature of the organic molecule, possessing a non-zero dipole moment, introduces noncentrosymmetric domains within the system, making it pseudo-cubic [6].

The initial step involves optimizing the cubic unit cell to ascertain accurate lattice parameters and organic molecular orientations. The lattice parameters obtained are 6.320, 6.315, and 6.349 Å for the three dimensions. The variations in the second and third dimensions, relative to the first lattice parameter, stand at approximately -0.08 % and 0.46 %, respectively. These values are close to the experimenal values [6].

Within the optimized cubic unit cell of MAPbI$_3$, an exploration of diverse organic molecule orientations was undertaken. This investigation involved systematic rotations of the organic molecule within the optimized system, executed around the X, Y, and Z axes. Each rotation was carried out at 15° intervals. The resulting graphical representations of these rotations are displayed in Figure 3.2. The figure effectively illustrates that the rotation of the organic molecule induces energy changes. Notably, these changes can reach up to an energy barrier of about 250 meV. Although this energy values are 10 times kT at room temperature, rotations are still possible, in particular at elevated temperatures. This insight underscores the potential for molecular reorientation at higher temperatures, a phenomenon enabled by the relatively low energy barriers involved. Previously, Chem et al. have calculated an activation energy of 94 meV for molecular rotation in the cubic system using the Arrhenius law [2].

The significance of this phenomenon is further substantiated through experimental validation. The oldest report dates back to 1985 by Wasylishen et al. [7]. Recently, solid state NMR studies conducted by the research group led by Kubicki et al. [8] have convincingly demonstrated the actual rotation of the organic molecule within the lattice. This experimental evidence aligns well with the theoretical insights gained from the energy barrier analysis and supports the notion of dynamic organic molecule rotation occurring within the perovskite lattice.

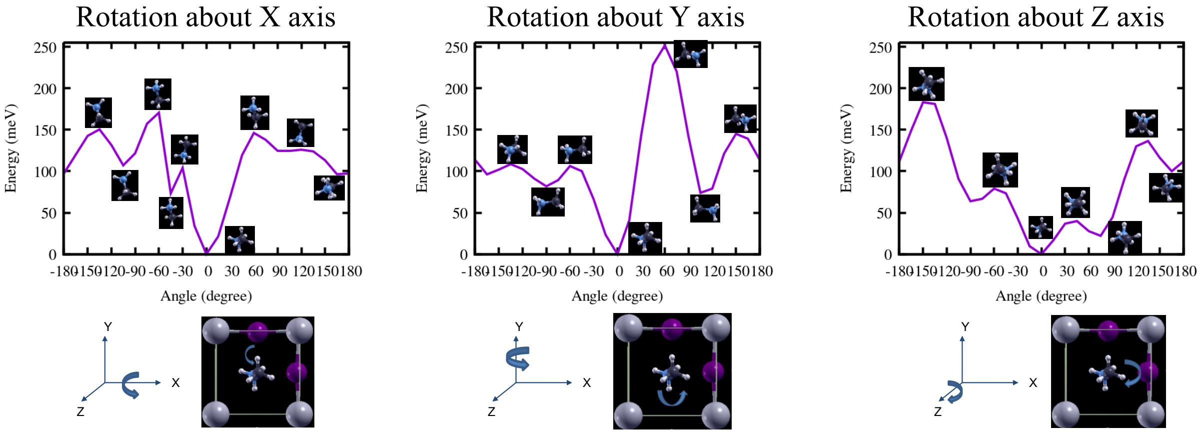

Figure 3.2: The changes in energy brought by the rotation of the MA molecule about the X, Y and Z axis respectively at intervals of 15° inside the inorganic cage.

In terms of the Glazer notation, the average configuration is $a^0a^0a^0$, with the organic molecules establishing three weak bonding links. Specifically, the H_N atoms form weak bonds with the iodine atoms present in the $\{100\}$ planes. This connectivity pattern resembles a three-dimensional network. Operating within the high-temperature phase, the molecules possess sufficient thermal energy to reorient themselves on a picosecond timescale [8] [9]. These thermal fluctuations effectively increase the effective radius of the cation, subsequently reducing the necessity for octahedral tilting to maintain a high tolerance factor [10].

An intriguing counterpoint to the aforementioned average configuration was reported by Beecher et al., who identified rotational instabilities within the lead iodide framework of the PbI_6 octahedra in cubic $MAPbI_3$. This observation was elucidated through high-energy resolution inelastic X-ray (HERIX) scattering [11]. Their study pointed towards the persistence of these rotational instabilities in the cubic perovskite structure at elevated temperatures, thus presenting a contrasting perspective to the assumption of stability in the high-temperature cubic phase. This local symmetry disruption, along with the existence of an instantaneous local structural variation within the cubic perovskite lattice, will be explored further in subsequent sections. The complexities arising from such dynamic behavior add an additional layer of intricacy to the understanding of perovskite materials and their behavior under varying temperature conditions.

3.1.4 Hydrogen Bonding Scheme

To differentiate between the various phases of MAPbI$_3$ and uncover similarities among the polymorphic states of the tetragonal form, our investigation centered on the H$_N$-I bonding patterns. By scrutinizing the bonding arrangements in different phases, we discerned distinctive features. A fundamental analysis of these bonding patterns was conducted for the three known phases: cubic, tetragonal, and orthorhombic. The dissimilarities are visually outlined in Figure 3.3, providing a comprehensive overview of the variations.

For the determination of hydrogen bonding interactions, a cutoff distance of 2.8 Å was employed. This criterion helps to identify the significant hydrogen bond formations and contributes to a clearer depiction of the bonding scheme disparities across the phases.

In the context of the cubic crystal system, the organic molecules within the structure exhibit continuous rotation within the central cavity due to the elevated temperatures (>327 K) [1, 2, 7]. This free rotational motion results in the absence of any discernible ordering of the H$_N$-I bonds.

Transitioning to the tetragonal phase, a distinct pattern emerges: only two H$_N$ atoms participate in the formation of hydrogen bonds. This intriguing arrangement, elaborated upon in Section 3.1.2, links these specific H$_N$ atoms exclusively to the iodine atoms situated within the MAI layer. This peculiar bonding scheme pattern exists in all the polymorphs of the tetragonal form reported previously [12]. We can thus ascertain the possibility of other existing polymorphs of the same bonding pattern. One of these is suggested as T$_n$, which will be discussed in further details in Sections 3.6 and 3.7.4. The difference in energy for this system is about 18 meV/fu with respect to the most stable tetragonal polymorph T$_A$.

In contrast, the orthorhombic crystal system presents a more complex hydrogen bonding network. All three H$_N$ atoms actively engage in hydrogen bonding, propagating along three distinct directions. Importantly, the iodine atoms they connect to are distributed across both the MAI and PbI$_2$ layers, highlighting the unique connectivity and interactions within this phase.

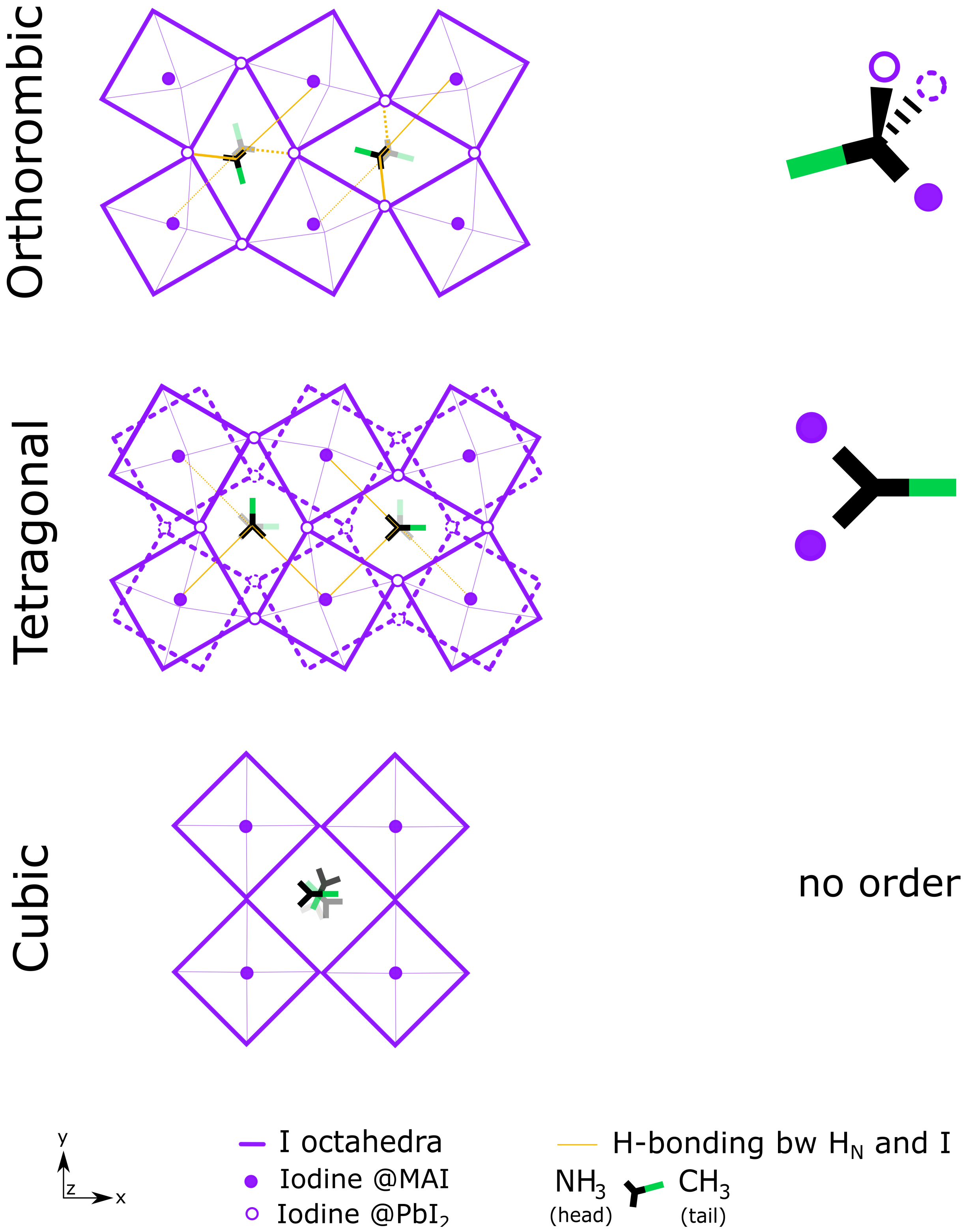

Figure 3.3: The hydrogen-bonding scheme in the structures of the cubic, tetragonal and orthorhombic MAPb$_3$ perovskite.

3.2 Study of polymorphism

As a general practice, crystalline materials are modelled by a periodically repeated unit cell containing the smallest number of atoms representing the space group symmetry determined from experiment; it is referred to as a monomorphous structure, with a single local environment and local symmetry. For MAPbI$_3$, this approach works well for the tetragonal and orthorhombic phase, since the organic molecules are all aligned. At higher temperatures, for cubic phase, one expects structural fluctuations induced by thermal effects. However, the concept of polymorphism in cubic MAPbI$_3$ was recently introduced [13]. It conveys the fact that, even without including the thermally induced vibrational and configurational free energy, the materials ground state structure presents long range structural distortions. Thus, the accepted perovskite structure is only an average one, allowing some orientational freedom for the organic moiety and distortions of the inorganic cage. This introduces into the model a fluctuating local environment, while retaining the average global symmetry, making it polymorphous. These changes persist even at low temperatures [11]. The evolution is sketched in Figure 3.4. Computationally, it is reported that features can be found only in large enough supercells, optimally 32 formula units for hybrid organic-inorganic perovskites [13].

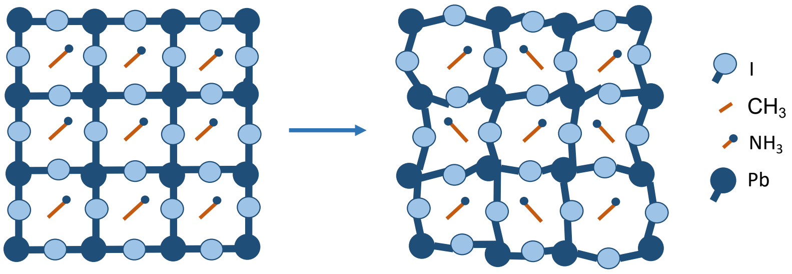

Figure 3.4: Evolution of the averaged monomorphous structure of cubic MAPb$_I$ to the polymorphous structure with different structural motifs.

Following this study, the polymorphous MAPbI$_3$ system was reproduced. An initial disorder on the 32 formula unit cubic system was achieved by random displacements of the atoms up to 0.20 Å from their ideal positions. The system was then relaxed at fixed volume.

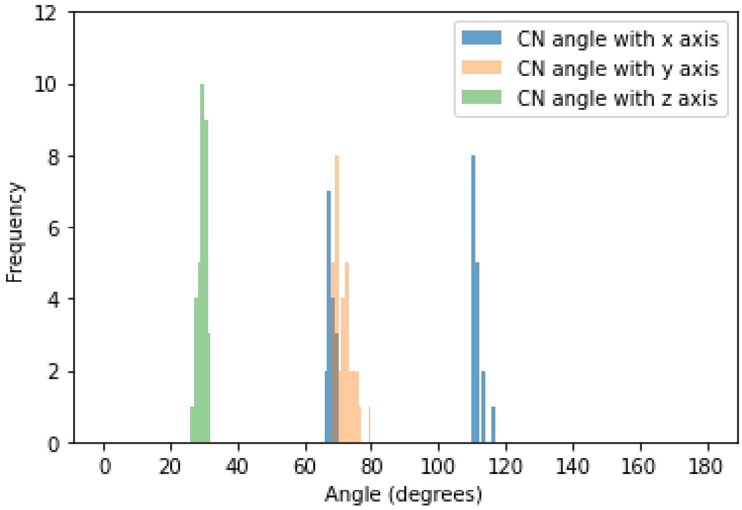

Figure 3.5: Orientation of the organic molecules in the 32 formula unit cell. The blue, saffron and green colours depict the C-N angle with respect to the x, y and z-axis, respectively.

It is well known that the organic molecules keep rotating inside the inorganic cage at high temperature in the cubic phase. The optimized monomorphous structure shows a single orientation with an angle of 77.2, 82.4, 15.0 along the x, y, z axis, respectively. However, in the 0 K polymorphous structure, we find a bimodal distribution of angular orientations as presented in Figure 3.5. The average angles of the C-N bond with respect to the y and z axes are 71.5 and 29.4 respectively. But along the x axis two average angles are obtained at 67.9 and 111.6 with half of the organic molecules oriented in each direction. This means that the constraints forcing the organic molecules in a particular orientation are overcome in the polymorphous structure by the energetic advantage of a complex arrangement of molecular orientations and inorganic cage distortions. Thus, a bimodal distribution of the angular orientations of MA in this phase is revealed.

We predict a Glazer Notation of $a^0b^-b^-$ for this polymorphous system. This is discussed in more detail in 3.3.

In terms of energy, the energy gain of the polymorphous structure with respect to the monomorphous one is calculated as:

$$\Delta E_{tot} = \frac{E_{tot_N}}{N} - E_{tot_{N=1}}$$

where Δ E$_{tot}$ is the total energy and N is the number of formula units. The gain in energy was only obtained when all the atoms including the organic molecules were subject to this randomization.

The relaxed cubic polymorphous structure is found to be at lower energy than the monomorphous one as shown in the Table 3.1. The same was done for tetragonal and orthorhombic systems. However, for these systems, we could not find a polymorphous structure whose energy was clearly lower than the monomorphous ones discussed in Sections 3.1.1 and 3.1.2.

Table 3.1: Change in energy per formula unit between the large supercell (32 fu) network for cubic, tetragonal and orthorhombic phases and the corresponding minimal cell structure, to indicate polymorphism in the systems. For the Pseudo-Tetragonal-3D, the difference w.r.t. the monomorphous cubic system is provided.

System (384 atoms)	ΔE_{tot} (meV/fu)	Ref. [13]
Cubic	-67, -68	-72
Tetragonal	0	2
Orthorhombic	8	4
Pseudo-Tetragonal-3D	-100	-

Another system, which we call the Pseudo-Tetragonal-3D system, was subjected to this study. This system is discussed in detail in the next Section 3.4.

3.3 A possible explanation to Twin-Domains

The cubic to tetragonal transformation in $MAPbI_3$ is of particular interest for the scientific community since this transformation takes place within the working temperature of the solar cell. On decreasing the temperature from 340K to attain room temperature (RT), Medjahed et al. observed the presence of twin domains at RT using experimental techniques of X-ray diffraction and synchrotron full-field diffraction X-ray microscopy [14]. This twinning has also been observed and reported in other publications [15] [16] [17] [18]. The threefold axis present in the average cubic phase can be lost with an increase of cell dimension in any of the three directions. However, the observation of only two domains out of three necessitates a justification.

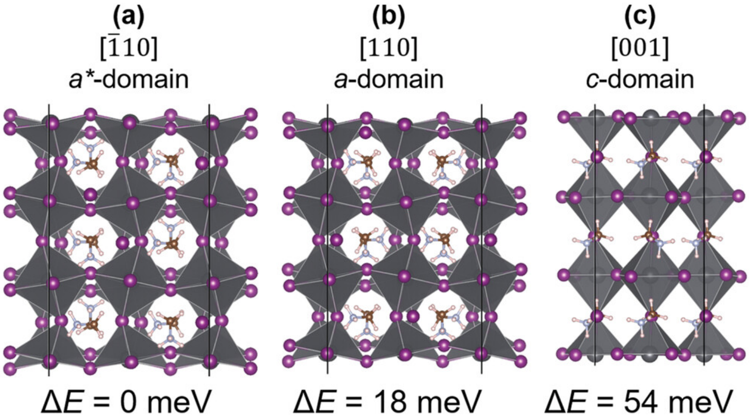

Figure 3.6: The three PbI_2 terminated surface configurations of tetragonal $MAPbI_3$ corresponding to a) $[\bar{1}10]$ b) [110] and c) [001] orientations. The total energy is normalized by the number of MA molecules for comparison. The image is taken from [14].

The domains observed are [hh0] (a-domain) and [001] (c-domain), out of which [001] domain is reported to be scarce. Medjahed and coworkers support this observation by a thermodynamic explanation based on surface calculations for MAI and PbI_2 terminated surfaces. For a PbI_2 terminated surface, they find a lower energy for the a-domain compared to the c-domain. An equal stability for both the domains is found for a MAI terminated surface. Furthermore, the mixed surface termination showed a reverted stability as summarized in Table 3.2. The opposite trend for PbI_2 and MAI terminated surface in the c-domain can be explained by the presence of surface corrugation in the MAI terminated surface, compared to a levelled one for PbI_2 terminated surface.

Table 3.2: Summary of the relative energy calculated for surface with different terminations.

Surface Termination	Relative energy of domain
PbI_2	$E_{a-domain} < E_{c-domain}$
MAI	$E_{a-domain} \approx E_{c-domain}$
Mixed	$E_{a-domain} > E_{c-domain}$

A kinetic explanation for this result is also possible. Different phases of $MAPbI_3$ can be differentiated using Glazer notations based on the type of tiltings in the inorganic cage [3]. These are given in table 2. We predict a Glazer Notation of $a^0b^-c^-$, with two tiltings, in the 32 formula unit polymorphous system. This is consistent with the observation of a bimodal distribution of molecular orientations in a large supercell of $MAPbI_3$ as depicted in Figure 3.5. Since this observation of twin domains is obtained when cooling down from the cubic phase, it can be expected that the polymorphous structure, can be driven to two tetragonal domains because of tiltings in two directions and bimodal molecular orientation. Moreover, this structure contains the hydrogen bonding characteristics of both the tetragonal and orthorhombic phases, connecting two types of Iodine.

Table 3.3: Glazer notations corresponding to the different phases in $MAPbI_3$.

Phase	Glazer Notation	No. of Tiltings
Cubic	$a^0a^0a^0$	0
Tetragonal	$a^0a^0c^-$	1
Orthorhombic	$a^-b^+c^-$	3
Polymorphous	$a^0b^-c^-$	2

3.4 Pseudo-Tetragonal-3D system

Building upon the thorough exploration of the hydrogen bonding scheme discussed in Section 3.1.4, a new system was investigated featuring a distinctive bonding arrangement. This system was deliberately designed with an inverted bonding scheme from that observed in the tetragonal phase, to display a contrasting configuration.

3.4.1 Hydrogen bonding scheme

The Pseudo-Tetragonal-3D system exhibits a markedly distinct bonding pattern. In this configuration, a unique and discernible bonding arrangement emerges. Specifically, the H_N atoms form hydrogen bonds exclusively with the iodine atoms located within the PbI_2 layer. This selective interaction pattern represents a contrast from the hydrogen bonding configuration observed in the tetragonal phase. Also, the H_N atoms establish connections between iodine atoms positioned within different PbI_2 layers in the (001) plane, resulting in the formation of a closed-loop motif. The visual representation of these intricate connections is shown in Figure 3.7. The various layers of iodine atoms, stacked atop each other, are depicted using different patterns given in label- Iodine @PbI_2 layer. This is different from the tetragonal bonding scheme where the H_N connections are with Iodine in the MAI layer. Additionaly, the bonding scheme is different from the orthorhombic for the same reason, although the number of hydrogen bonds is the same.

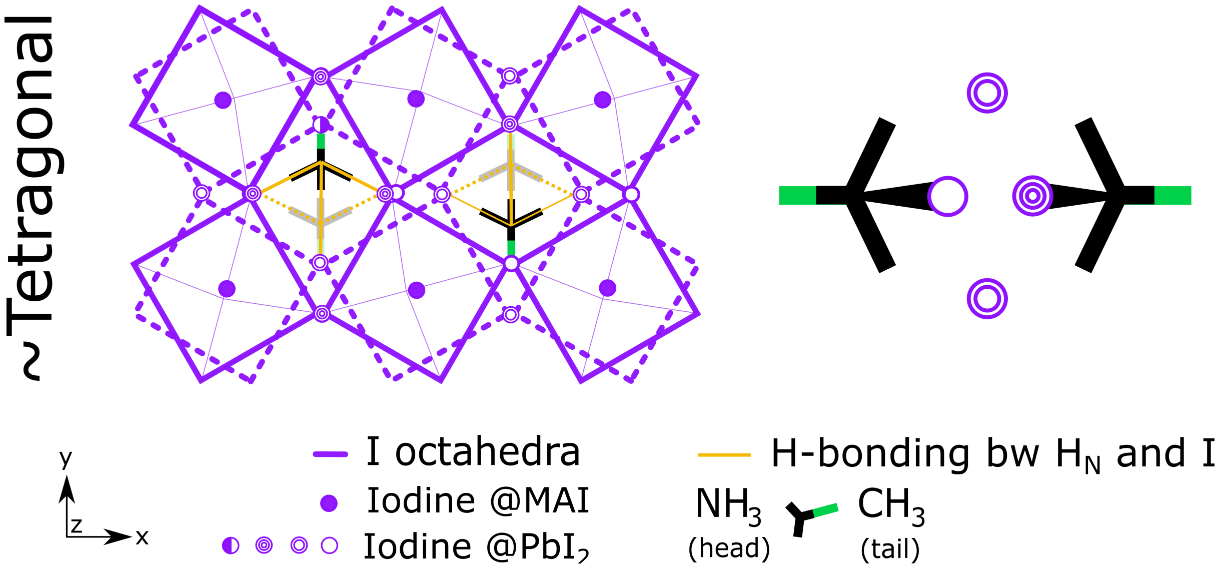

Figure 3.7: The hydrogen bonding scheme in Pseudo-Tetragonal-3D system. For a MA molecule, it makes three hydrogen-bonding connections with Iodines present in PbI_2 layers. This is contract to the tetragonal system which has H-I connections in MAI layer. Two of these three H-I connections are in the same PbI_2 layer, and makes a closed ring of hydrogen bonds with an adjascent MA. The third hydrogen bonds made by these two MA are in different planes above and below the PbI_2 layer with the closed ring.

3.4.2 Tetragonality

The tetragonal crystal system consists of a crystal with two sides of equal length and a third side perpendicular to them. The ratio of the length of the third side to the length of the equal sides is referred to as tetragonality. The tetragonality for each of the tetragonal systems, as well as the closely related Pseudo-Tetragonal-3D configurations, is outlined in Table 3.4.

Table 3.4: Table for the change in tetragonality in tetragonal and Pseudo-Tetragonal-3D systems with 96 atoms having Glazer Notation $a^0a^0c^-$.

System	a (Å)	c/a	change in c (%)
Tetra A	12.365	1.043	4.27
Tetra B	12.384	1.039	3.95
Tetra C	12.387	1.038	3.80
Tetra D	12.399	1.037	3.71
Tetra E	12.393	1.038	3.82
Tetra n	12.377	1.039	3.90
Pseudo-Tetragonal-3D	12.415	1.023	2.31

In addition to the distinctive bonding scheme, this system also deviates in terms of tetragonality. For all the tetragonal systems A-E and n, the tetragonality is 4.0 (+/- 0.3)%, while that for the Pseudo-Tetragonal-3D system is 2.31%. We have named this system Pseudo-Tetragonal-3D because of these small differences in the tetragonality parameter and the bonding scheme. Also, a murnaghan fit of this Pseudo-Tetragonal-3D system with a cubic constraint gives a structure very close in energy to the fully relaxed one, and only slightly higher than the various tetragonals.

3.4.3 Pair-distribution function

The pair-distribution function (PDF) for various systems, including the tetragonal polymorphs (A-E, n), monomorphous, polymorphous and the Pseudo-Tetragonal-3D system, were computed and plotted. The computational methodology for obtaining these PDF is detailed in Section 2.2.2. It's important to note that during the PDF calculation, only the inorganic cage was taken into consideration. The resulting plots are presented in Figures 3.8 and 3.9. These plot span interatomic distances ranging from 2 to 8 Å. Peaks within the plot are indicative of specific interatomic distances, including Pb-I, I-I, Pb-I/Pb-Pb, and Pb-I, respectively.

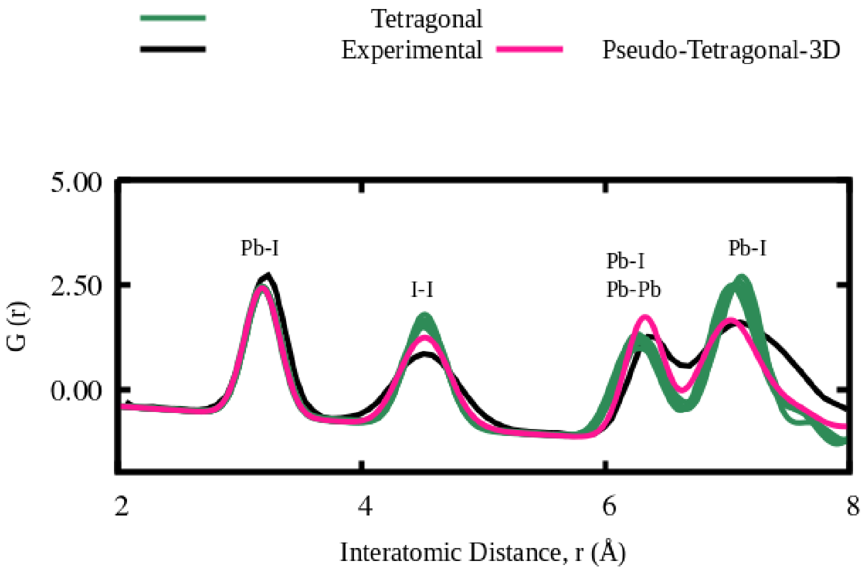

Figure 3.8: The calculated pair distribution function G(r) of the Pseudo-Tetragonal-3D (pink) and tetragonal forms (green) of $MAPbI_3$ as a function of interatomic distance (r). Experimental values represented in black are taken from [11].

In the first plot 3.8, the black line corresponds to the experimental PDF of the high-temperature cubic $MAPbI_3$ perovskite, sourced from [11]. The green lines represent the PDFs for the tetragonal polymorphs (A-E, n). These polymorphs exhibit minor differences among themselves but deviate from the experimental PDF, especially at the I-I and Pb-I peaks. The pink line corresponds to the Pseudo-Tetragonal-3D system, and notably, its PDF closely matches the experimental PDF of the high-temperature cubic $MAPbI_3$, especially at the I-I and Pb-I peaks.

In the second plot 3.9, the skyblue and blue lines correspond to the monomorphous and polymorphous cubic systems, respectively. The 1st, 3rd and 4th peaks for the polymorphous system are lower when compared to the experimental one, while the monomorphous cubic one appears to have three peaks between 7-8 Å. The Pseudo-Tetragonal-3D system, which is common in both the plots, appears to have a much better agreement compared to the others.

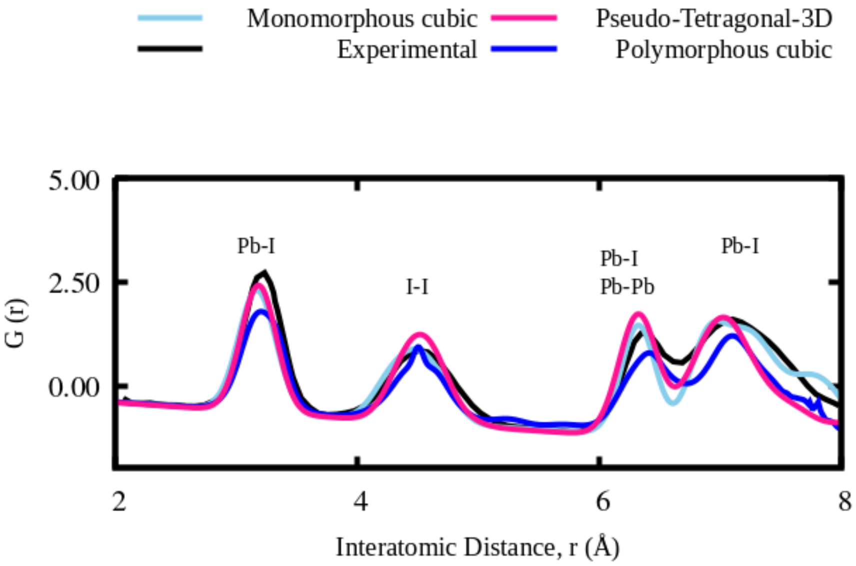

Figure 3.9: The calculated pair distribution function G(r) of the Pseudo-Tetragonal-3D (pink), monomorphous (sky-blue) and polymorphous (blue) forms of MAPbI$_3$ as a function of interatomic distance (r). Experimental values represented in black are taken from [11].

In conclusion, the PDF captures the structural characteristics in the inorganic cage of the various systems were studied. With this, we find an agreement between the inorganic cages of the high-temperature cubic MAPbI$_3$ [11] and the Pseudo-Tetragonal-3D system. This means that the persisting distortions in the experimental cubic system are reflected in the Pseudo-Tetragonal-3D system.

3.4.4 Energy

Despite its relatively small size, composed of 4 formula units (48 atoms), this system demonstrates a notable degree of polymorphism, with an energy difference of 0.1 eV per formula unit (fu) compared to the monomorphous form. In other words, this configuration possesses an energy that is lower by 0.1 eV for each formula unit. Notably, this level of stabilization is more substantial in comparison to the value of 67 meV/fu that was achieved through atomic randomization within the cubic system (refer to Table 3.1 for details). This means that even with a smaller supercell of 48 atoms, the gain in energy and the structural distortions can be realized. This is in contrast with the prediction of the requirement of a large supercell (384 atoms) to reveal distortions in the high-temperature cubic system at 0K by Zhao and coworkers [13].

3.5 Complex energy landscape

The potential energy landscape of MAPbI$_3$ reveals energy differences in meV/formula-unit. This is given in Figure 3.10. The energy differences are plotted as relative energy in meV/fu with respect to the orthorhombic phase against the distortion from cubic system in values of c/a ratio. The energy levels in the figure correspond to

- Orthorhombic (red): The phase corresponding to lowest energy. All the relative energies are referenced to this phase.
- Tetragonal (shades of green): These are about 50 meV/fu higher than the orthorhombic one. An expanded version of the tetragonal energy landscape is given in Figure 3.1.
- Cubic (shades of blue): Energies are depicted for a) monomorphous b) polymorphous c) Pseudo-Tetragonal-3D systems. The energy differences are provided in Table 3.1.

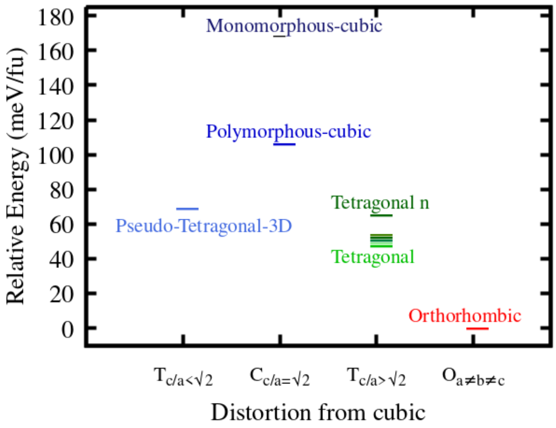

Figure 3.10: The complex relative energy plot of MAPbI$_3$ revealing its complex nature due to the high degree of freedom. The plot maps the relative energies of different phases of MAPbI$_3$ across three distinct crystallographic systems: Cubic (C), Tetragonal (T), and Orthorhombic (O). The c/a ratios correspond to the ratio of the cell parameter c with respect to a, which for an ideal cubic $\sqrt{2}\sqrt{2}1$ supercell should be $\sqrt{2}$. The relative energies (in meV/fu) on y axis are referenced to the most stable orthorhombic phase. The energies of O, T and C are in similar range as published earlier [19].

The potential energy surface of MAPbI$_3$, from the limited subset of atomic positions, is found to be complex and glassy-like. Changes in molecular orientations especially in the high energy cubic phase changed their energy level. However, this analysis does not encompass all the disorders associated with organic molecular orientations or tiltings within the inorganic cage, which fall beyond the scope of this thesis.

3.6 Charge Density

Charge density calculations provide valuable insights into the spatial distribution of electrons within molecules or crystal structures. After conducting bonding analysis, it was hypothesized that distinct bonding schemes could be discerned by visualizing the one-dimensional charge density profiles along the line connecting H$_N$ and I. In the realm of hydrogen bonding patterns, charge density assumes a pivotal role in distinguishing among diverse bonding arrangements. The electronic charge density map can unveil the likelihood of locating an electron at specific spatial coordinates. This information is crucial for elucidating the nature of chemical bonds and interactions.

To analyze this, the charge density between H$_N$ and I bonds for different polymorphs of MAPbI$_3$ along with that of the orthorhomic (O) phase and the Pseudo-Tetragonal-3D configutation were plotted. The corresponding plots are given in Figure 3.11. As expected, the electronic charge density between H$_N$ and I bonds can be seen to be higher on I than at H site while it diminishes in the centre with a noticeable bump towards I.

The charge density plots for the different tetragonal polymorphs do not exhibit much difference with each other. All of them show two H$_N$ and I bonds (in purple and in dashed-pink) that have the same charge density, since they connect the two equivalent a and b cell dimensions, and a third longer H$_N$ and I bond (in green) corresponding to the one connecting in the c direction. This holds true also for the new tetragonal form T$_n$ introduced in Section 3.1.4.

In contrast, the charge density and lengths of the three H-I bonds in the orthorhombic configuration are more consistent. A similar pattern is observed in the Pseudo-Tetragonal-3D form. However, the lengths of the H-I bonds in the orthorhombic configuration are distinct from those in the Pseudo-Tetragonal-3D arrangement because of the difference in length of the H$_N$-I bond which is on average about 2.62 in the orthorhombic and 2.74 in the Pseudo-Tetragonal-3D system. Hence we can say that the charge density does distinguish the different types of bonding schemes.

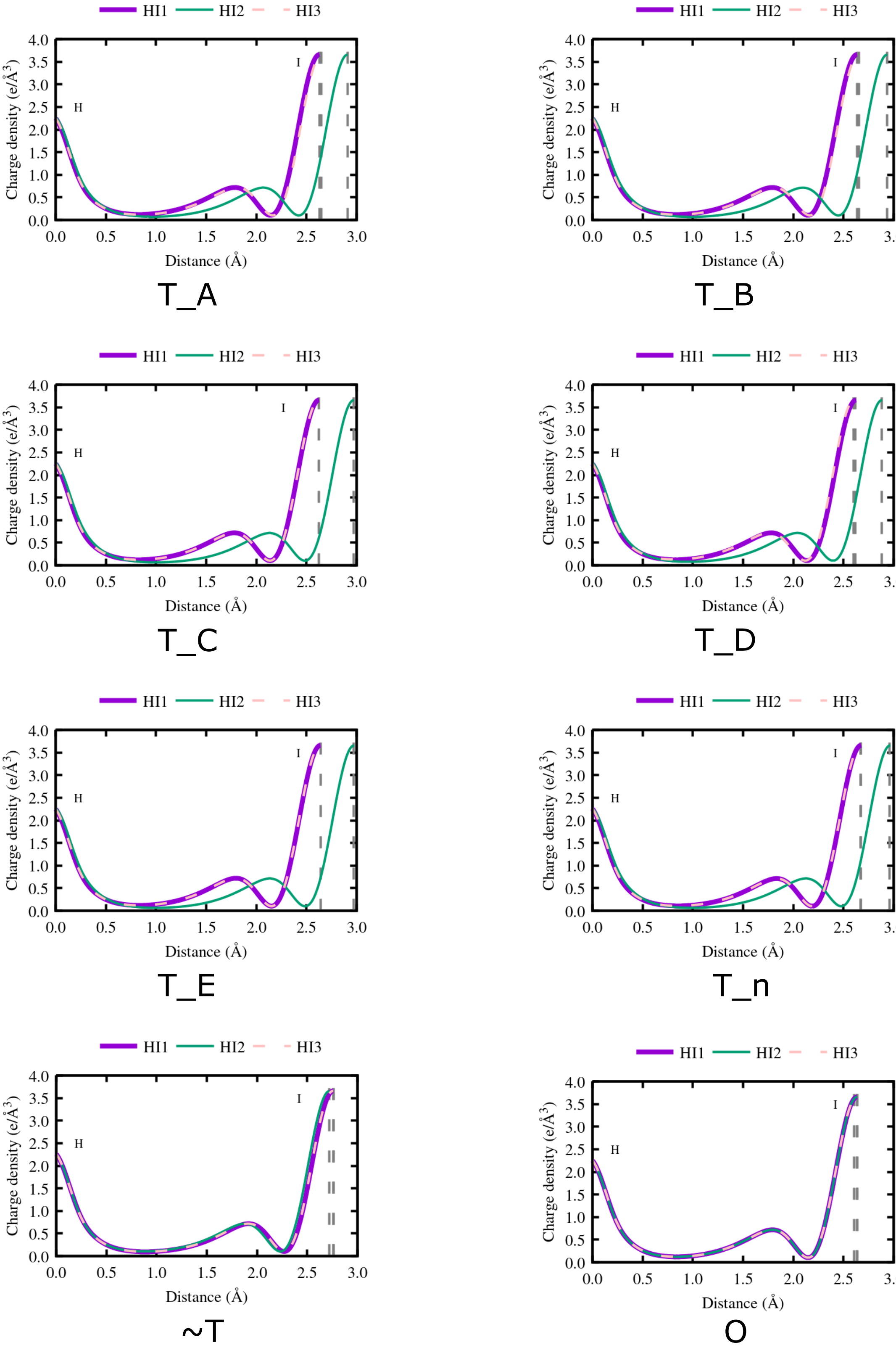

T_A

T_B

T_C

T_D

T_E

T_n

~T

O

Figure 3.11: The charge density plots for the different polymorphs of MAPbI$_3$ in the tetragonal phase along with that of the orthorhomic (O) phase and the Pseudo-Tetragonal-3D configuration $\sim$ T.

For the Pseudo-Tetragonal-3D 8 formula unit configuration, the bonding scheme makes a closed circuit where I are bi-connected with H_N on both sides. The charge density for this closed-circuit was analyzed and is presented in Figure 3.12. We start from one of the MA molecules for C-N and follow a bead-to-bead connection C-N-H-I-H-N-C, to reach the other organic molecule via I in the inorganic cage. Another possibility could be C-N-H-I-H-N-H-I, where instead of stopping at the next molecule, we go further to another hydrogen that directs the path to another hydrogen bonded iodine.

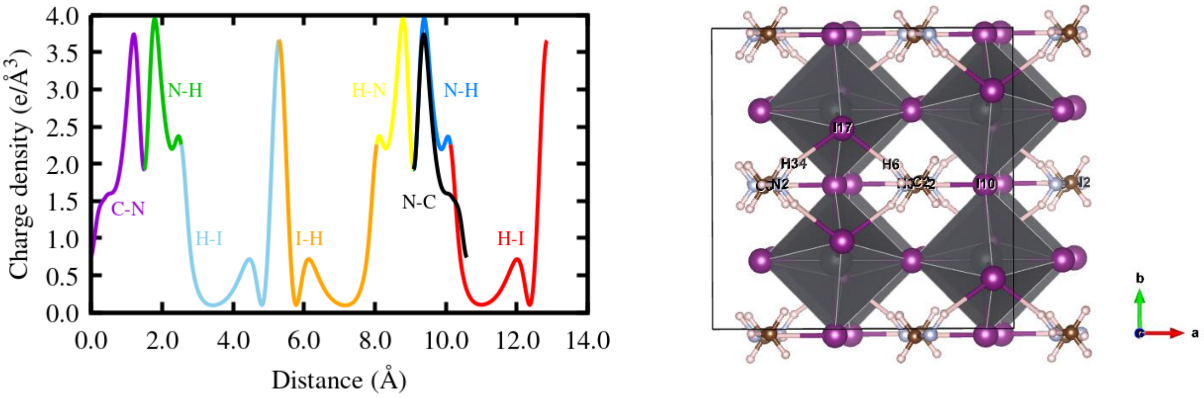

Figure 3.12: On the left, the charge density plot for Pseudo-Tetragonal-3D $MAPbI_3$. This distribution adheres to the pathway of linkages as delineated in the configuration illustrated on the right.

3.7 Computational Analysis of Energy Barriers using NEB

To obtain the energy barriers of phase transitions and study the associated changes in structural parameters, we employed the Nudged Elastic Band (NEB) method. Our investigation commenced with the Pseudo-Tetragonal-3D phase as the initial configuration, with the objective of determining the energy barrier for its transformation into one of the tetragonal phases. The intricate shift in the bonding scheme, elaborated earlier sections, is taken into account. The theoretical aspects of the NEB calculations are discussed in Section 2.2.3.

3.7.1 NEB Tests

We used NEB calculation to investigate the energy barrier involved in rotating one of the molecules in the unit cell. For this, the orientation of one of the molecules in the Pseudo-Tetragonal-3D form was changed by about 90 degrees as shown in Figure 3.13. In general, there are two types of molecular rotations that can be involved:

- Rotation about the molecular axis: This type of rotation involves the MA organic molecule rotating about its own axis without change in the positions of C-N. The rotation results in the establishment of a C3 point group symmetry.
- Rotation of the molecular axis: This type of rotation involves the orientation of the molecular axis itself being changed while keeping the molecular structure intact.

While following the path depicted here, the possibility of all three orientations of the molecule based on C3 space group are considered. This means that any of the three H atoms attached to C/N would be present in the rotated molecule. These are considered by taking three cases: clockwise (type A), anti-clockwise (type C) or inversion (type B) corresponding to rotations with respect to the position of organic molecules about the molecular axis. For each of the cases, the number of image for the NEB calculations was restricted to 7.

The graph for activation energies is presented in Figure 3.14. From the graph, it is evident that the activation energy required for the rotational movement of a single MA is lower for type A/C rotations (clockwise/anti-clockwise) when compared to type B inversion via 180° rotation about the C-N axis. While this inversion was achieved, a closer examination of the accompanying images reveals structural instability and molecular breakage along this path. This instability is mirrored in the activation energy plot, manifesting as a high activation energy and a significant dip for type B rotation. This could have been corrected using more number of images but we did not expect it to give an activation energy less than type A/C.

In addition to the above-mentioned tests, another investigation was carried out to examine the effect of changing the number of images. In this particular test, the number of images was varied from 7 to 15, using the type A molecular orientation. The observed result showed a minimal change in activation energy, decreasing from 0.13 to 0.12 eV.

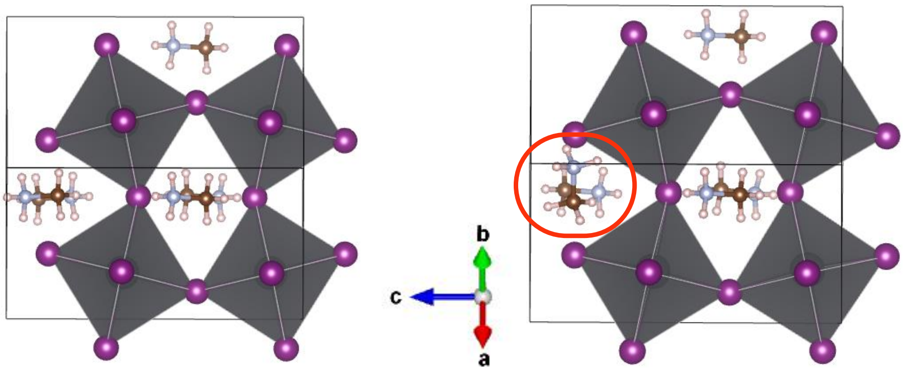

Figure 3.13: Configuration of the Pseudo-Tetragonal-3D form on the left along with the corresponding configuration with one of the rotated molecules on the right.

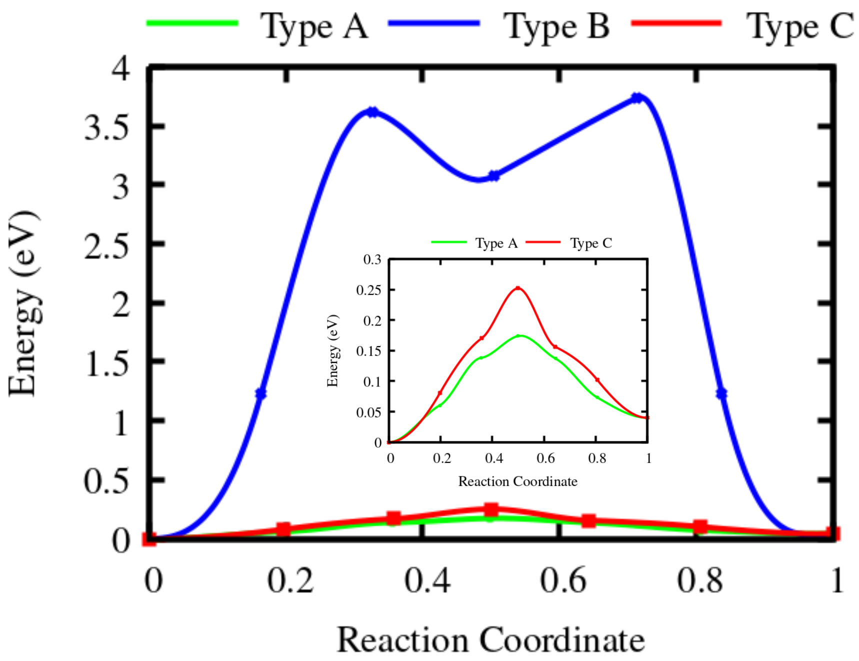

Figure 3.14: The activation energy plot for the three different types of rotations about the molecular axis represented by type A, B and C. The type A and C correspond to clockwise and anti-clockwise rotation of the organic molecule respectively with reference to the Nitrogen side. These are enlarged in the inset for better visibility of the activation energy.

3.7.2 Between two orientations of the Pseudo-Tetragonal-3D form

The Pseudo-Tetragonal-3D form of $MAPbI_3$, initially consisting of 4 formula units, can be transformed into an 8 formula unit system by applying a 45-degree rotation in the ab plane. This rotation leads to the expansion of the supercell, resulting in the desired configuration. Conversely, it is also possible to downsize or contract the system by reversing the 45-degree rotation of the supercell. By doing so, we can obtain the same 4 formula unit system depicted as the top layer within the green box in Figure 3.15. But additionally, we could also obtain another system which is the upper half of the supercell represented in the dashed blue box. Both of these systems are fundamentally similar, but individually, they lack the crucial tiltings required to accurately define the glazer notation in at least one direction. These 4 formula unit orientations are represented in the Figure 3.15 on the left and right, with the 8 formula unit expansion in the centre. We do the NEB analysis for the two 4 formula unit systems to test if the inorganic cage can reframe itself to obtain the tiltings in the other orientation.

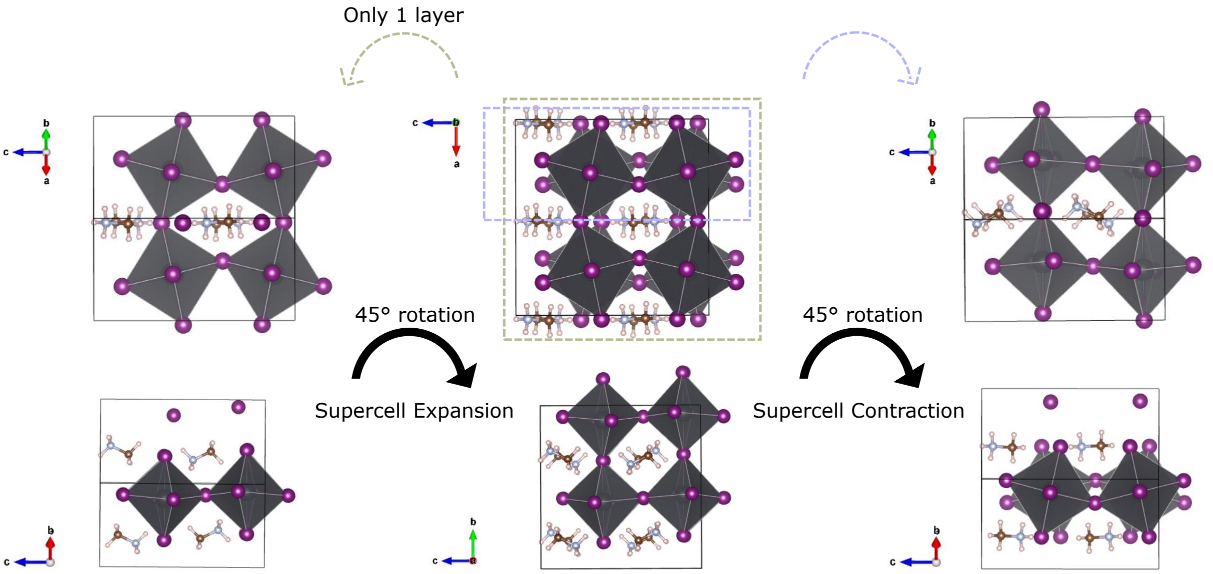

Figure 3.15: The two orientations of the Pseudo-Tetragonal-3D form of MAPbI$_3$ in 4 formula units on the left and right, with the expanded 8 formula unit system in the centre.

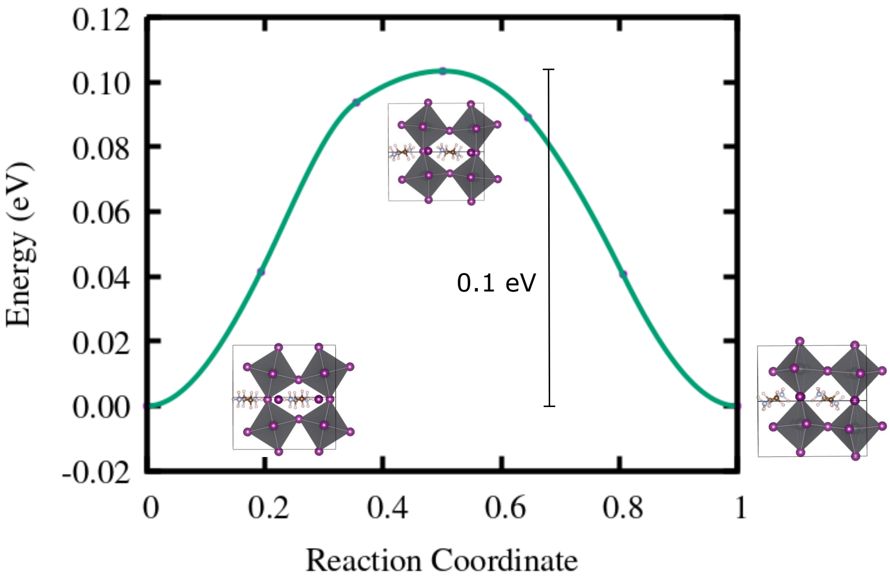

Figure 3.16: Energy vs reaction coordinate graph depicting the activation energies for the phase transformation between two orientations of the Pseudo-Tetragonal-3D form of MAPbI$_3$. The calculation was done on 4 formula unit systems.

The energy of both of these systems is determined to be the same. To examine the interchangeability of the two systems consisting of four formula units, we assess the energy barrier necessary for switching the tiltings and molecular orientation between the two. In this analysis, we designate the atomic positions in the two systems as the initial and final positions, respectively, and limit the entire connecting pathway to seven images. The obtained minimum energy pathway is illustrated in Figure 3.16. The plot reveals a low activation energy of 0.1 eV for the path. This is 4 times the thermal energy at room temperature (25 meV). This implies that this switch of the octahedra could be possible via thermal contributions.

3.7.3 Between Pseudo-Tetragonal-3D system and a tetragonal polymorph

This NEB computation explored the transition between the cubic and one of the tetragonal forms (polymorph D in Figure 3.1. For the initial structure, the 8 formula unit system obtained via a 45 degree rotation of the 4 formula unit Pseudo-Tetragonal-3D form, depicted in the centre of the Figure 3.15 was used. Also, to facilitate a meaningful comparison with the tetragonal form, the initial configuration of the system which featured a Glazer notation of $a^0b^-c^0$, was subsequently altered to $a^0b^0c^-$. This is done by switching the y and z axis. This adjustment in the Glazer notation allowed for a direct and pertinent assessment between the two configurations since their c/a ratio is close in this configuration of Pseudo-Tetragonal-3D (refer to Section 3.4.2). The initial and final systems are depicted in Figure 3.17. To fulfil the criteria of same cell dimentions for NEB , the Pseudo-Tetragonal-3D system was relaxed with cell dimentions of the tetragonal polymorph. The transition path between these two comprised of a sequence of 25 distinct images. Again, this analysis involving the Pseudo-Tetragonal-3D and tetragonal forms necessitated a dual transformation: firstly, the manipulation of the molecule's orientation through the rotation of C-N about its own axis, and secondly, the reorientation of the C-N axis itself. In this context, of the total 8 molecules involved, a subset of 2 and 4 molecules demanded a repositioning of the C-N axis by approximately 120° and 90°, respectively. Conversely, the remaining 2 molecules exclusively mandated a 60° rotation about the C-N axis, encompassing both clockwise and anti-clockwise possibilities. Therefore, for the two molecules, four pathways were considered with a combination of clockwise and anti-clockwise rotations about C-N axis.

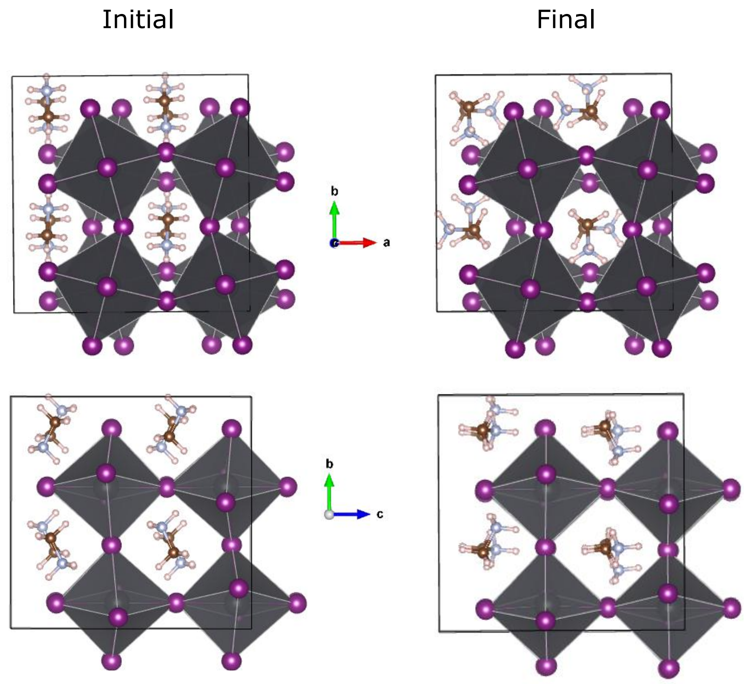

Figure 3.17: Initial and final configurations for the NEB calculation between Pseudo-Tetragonal-3D and tetragonal system, respectively. The lower figures depict the identical configuration but viewed from an alternate perspective.

Table 3.5: Table for the activation energy of the phase transformation from Pseudo-Tetragonal-3D to tetragonal $MAPbI_3$. Forward and backward activation energies are represented by E_{af} and E_{ab}.

Direction	E_{af} (eV)	E_{ab} (eV)
AA	0.65	0.74
CC	0.48	0.57
CA	0.44	0.53
AC	0.42	0.51

The NEB outcomes corresponding to the four permutations of clockwise and anti-clockwise rotations are tabulated in Table 3.5, denoting ’A’ for anti-clockwise and ’C’ for clockwise orientations. Remarkably, the derived activation energies, ranging from 0.42 to 0.74, exhibit similarity, albeit marginally higher for the AA combination. This means that the other molecules involved in the reorientation of the molecular control the activation energy. These activation energy values, however, tend to surpass the thermal energy threshold at room temperature (25 meV), implying considerable energy barriers. The corresponding activation energy plot is depicted in Figure 3.18.

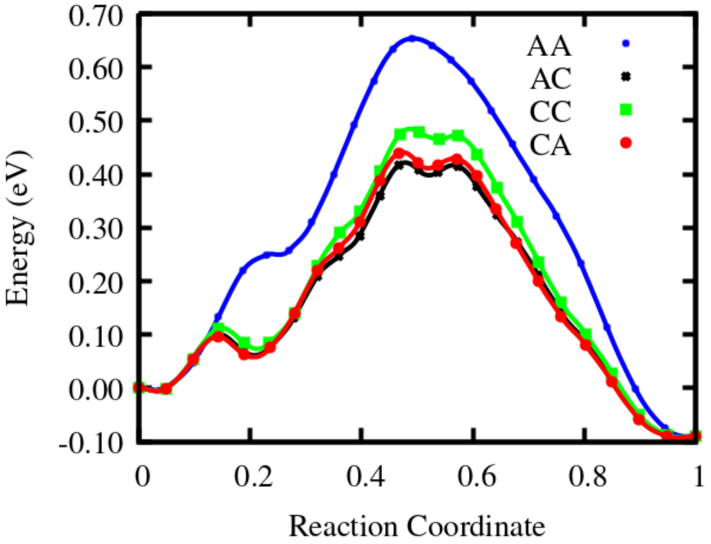

Figure 3.18: Energy vs reaction coordinate graph depicting the activation energies for the phase transformation from Pseudo-Tetragonal-3D to tetragonal $MAPbI_3$. The calculation was done using 8 formula unit cells. Clockwise and anti-clockwise rotation of the organic molecules is represented by A and C, respectively.

The discernible minima in the activation energy plot could potentially be attributed to three underlying factors:

- Constriction due to size: Imposed size constraints might influence the reorientation process as molecules strive to adjust spatially.
- Disruption of charge equilibrium: Inequitable rotations as seen in the intermediate images produced could disturb the delicate charge equilibrium within the system.
- Shifting weak connections: The repositioning of the H-I weak linkage to an alternate iodine site could induce these fluctuations.

These combined influences likely contribute to the observed activation energy fluctuations and structural dynamics within the system.

3.7.4 Between Pseudo-Tetragonal-3D system and a new tetragonal polymorph

Following the bonding scheme of the tetragonal $MAPbI_3$ as discussed in Section 3.1.4 and in Figure 3.3, we derived a new polymorph of the tetragonal form. This new tetragonal polymorph is shown in Figure 3.19 along with the bonding scheme. This new tetragonal form corresponds well with the 8 formula unit Pseudo-Tetragonal-3D form having glazer notation $a^0a^0c^-$. The Pseudo-Tetragonal-3D form needs just a rotation of C-N about its own axis, without any reorientation of the C-N axis itself to reach the configuration of the new tetragonal form, hence making the transition between the two easier. The initial and final structures of this NEB pathway are provided in Figure 3.20. To fulfil the criteria of same cell dimentions for NEB , the Pseudo-Tetragonal-3D system was relaxed with cell dimentions of the new tetragonal polymorph. Nine images were considered sufficient for this activation energy pathway, which appears smooth as seen in the activation energy plot in Figure 3.21). The resulting activation energy obtained is 44 meV for the forward reaction and 61 meV for the backward reaction. This value is close to the thermal energy at room temperature (25 meV).

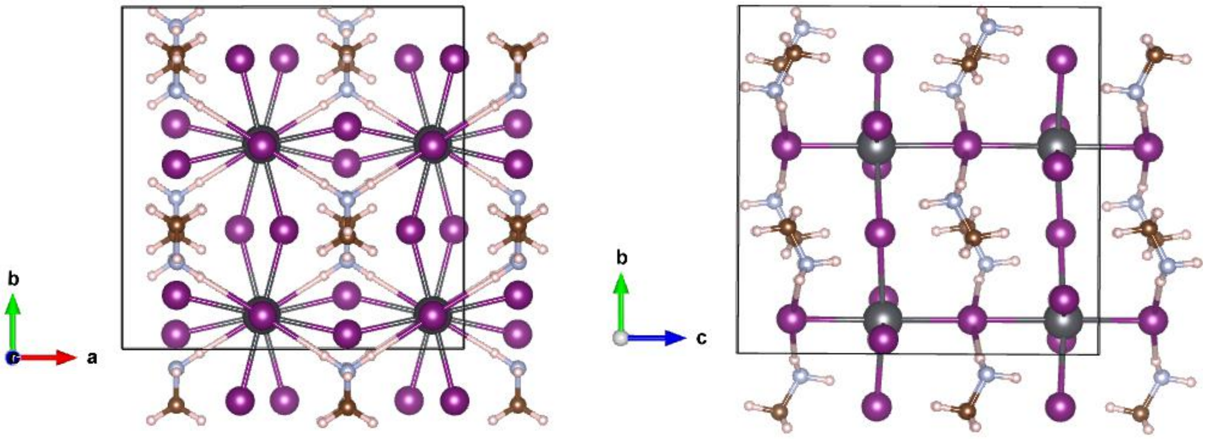

Figure 3.19: A new tetragonal form that follows the bonding scheme of the tetragonal systems as presented in Figure 3.3.

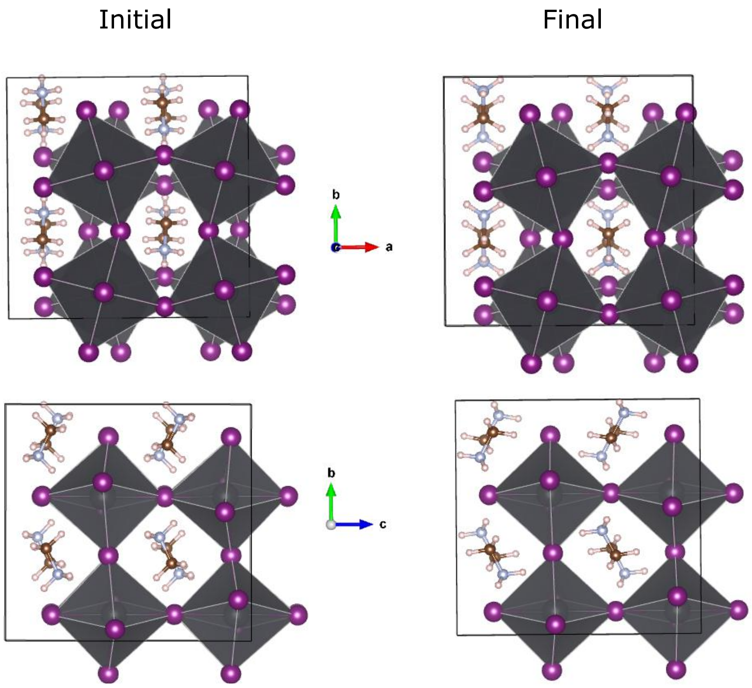

Figure 3.20: Initial and final configurations for the NEB calculation between Pseudo-Tetragonal-3D and the new tetragonal polymorph, respectively. The lower figures depict the identical configuration but viewed from an alternate perspective.

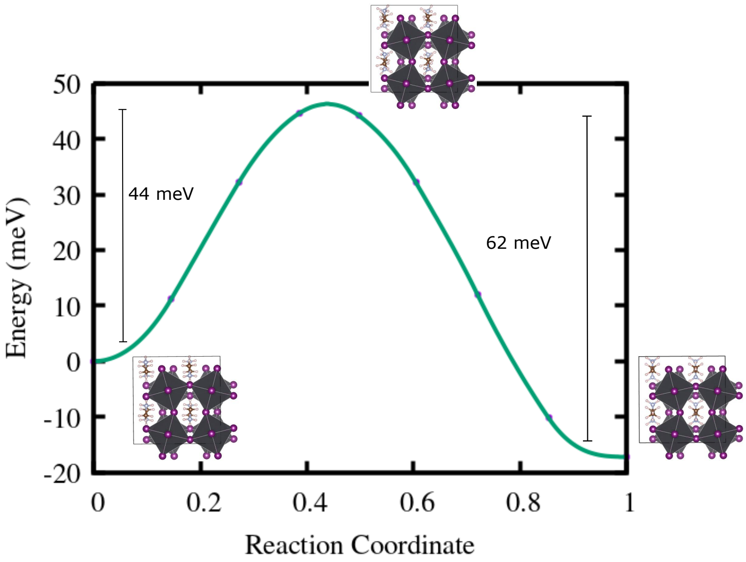

Figure 3.21: Reaction pathway for the Pseudo-Tetragonal-3D form to the new tetragonal form displaying a low activation energy of 44 meV.

3.8 Conclusion

In conclusion, this chapter has taken a dive into unraveling the intricate structure of the complex MAPbI$_3$ system, characterized by a high degree of freedom stemming from both the molecular composition and the surrounding cage. Our exploration has meticulously examined the fundamental hydrogen-bonding scheme present in all three known phases of the system. Building upon this foundation, our analysis has extended to encompass the newly discovered polymorphous network, leading to the identification of potential structures associated with both the cubic and tetragonal phases. Notably, the Pseudo-Tetragonal-3D system sets itself apart through distinct characteristics discerned via pair-distribution function and charge density analyses within the hydrogen bonding network. Significantly, our findings demonstrate the feasibility of attaining a cubic system with an energy level approximately 100 meV lower than its 'monomorphous' counterpart, even in the absence of random distortions, and with a smaller supercell consisting of only 4 formula units (48 atoms). The energy landscape of this system, as partially unveiled, is undeniably complex and glassy-like.

Furthermore, our investigation has shed light on the phase transformations between these phases, involving substantial rotations either about the C-N axis or the C-N axis itself. The selection of initial and final configurations, as well as the establishment of an optimal transition path through intermediate images, emerges as a crucial factor in determining the activation energy barrier for these transitions. Our observations suggest that it is primarily the rotation of the C-N axis itself drive the high activation energy, whereas rotations about the C-N axis have a relatively minor impact on the activation energy profiles. Our research reveals the significance of identifying an appropriate tetragonal phase with a distinct I-H$_N$ bonding scheme, closer in resemblance to the Pseudo-Tetragonal-3D system. This discovery allows for a remarkably low activation energy barrier of just 44 meV during the cubic to tetragonal transformation, making it feasible at room temperature due to the rotation about the C-N axis. These findings hold particular importance as the transformation occurs within the operational temperature range of photovoltaic devices.

REFERENCES

[1] P An and S Thomson. Observing phase transitions in a halide perovskite using temperature dependent photoluminescence spectroscopy observing phase transitions in a halide perovskite using temperature dependent photoluminescence spectroscopy. *Edinburgh Instruments*, pages 1–4, 2018. pages 74, 76, 78

[2] Tianran Chen, Benjamin J Foley, Bahar Ipek, Madhusudan Tyagi, John RD Copley, Craig M Brown, Joshua J Choi, and Seung-Hun Lee. Rotational dynamics of organic cations in the $CH_3NH_3PbI_3$ perovskite. *Physical chemistry chemical physics*, 17(46):31278–31286, 2015. pages 74, 76, 78

[3] Anthony M Glazer. The classification of tilted octahedra in perovskites. *Acta Crystallographica Section B: Structural Crystallography and Crystal Chemistry*, 28(11):3384–3392, 1972. pages 74, 84

[4] Jung-Hoon Lee, Nicholas C Bristowe, Paul D Bristowe, and Anthony K Cheetham. Role of hydrogen-bonding and its interplay with octahedral tilting in $CH_3NH_3PbI_3$. *Chemical Communications*, 51(29):6434–6437, 2015. pages 74

[5] Wen-Yi Tong, Jin-Zhu Zhao, and Philippe Ghosez. Missed ferroelectricity in methylammonium lead iodide. *arXiv preprint arXiv:2204.00421*, 2022. pages 75

[6] Constantinos C Stoumpos, Christos D Malliakas, and Mercouri G Kanatzidis. Semiconducting tin and lead iodide perovskites with organic cations: phase transitions, high mobilities, and near-infrared photoluminescent properties. *Inorganic chemistry*, 52(15):9019–9038, 2013. pages 76

[7] Roderick E Wasylishen, Osvald Knop, and J Bruce Macdonald. Cation rotation in methylammonium lead halides. *Solid state communications*, 56(7):581–582, 1985. pages 76, 78

[8] Dominik J Kubicki, Daniel Prochowicz, Albert Hofstetter, Peter Pechy, Shaik M Zakeeruddin, Michael Gratzel, and Lyndon Emsley. Cation dynamics in mixed-cation $MA_xFA_{1-x}PbI_3$ hybrid perovskites from solid-state nmr. *Journal of the American Chemical Society*, 139(29):10055–10061, 2017. pages 76, 77

[9] Guy M Bernard, Roderick E Wasylishen, Christopher I Ratcliffe, Victor Terskikh, Qichao Wu, Jillian M Buriak, and Tate Hauger. Methylammonium cation dynamics in methylammonium lead halide perovskites: a solid-state nmr perspective. *The Journal of Physical Chemistry A*, 122(6):1560–1573, 2018. pages 77

[10] Ryosuke Jinnouchi, Jonathan Lahnsteiner, Ferenc Karsai, Georg Kresse, and Menno Bokdam. Phase transitions of hybrid perovskites simulated by machine-learning force fields trained on the fly with bayesian inference. *Physical review letters*, 122(22):225701, 2019. pages 77

[11] Alexander N Beecher, Octavi E Semonin, Jonathan M Skelton, Jarvist M Frost, Maxwell W Terban, Haowei Zhai, Ahmet Alatas, Jonathan S Owen, Aron Walsh, and Simon JL Billinge. Direct observation of dynamic symmetry breaking above room temperature in methylammonium lead iodide perovskite. *ACS energy Letters*, 1(4):880–887, 2016. pages 8, 9, 77, 80, 87, 88

[12] Xie Zhang, Jimmy-Xuan Shen, Mark E Turiansky, and Chris G Van de Walle. Minimizing hydrogen vacancies to enable highly efficient hybrid perovskites. *Nature Materials*, 20(7):971–976, 2021. pages 78

[13] Xin-Gang Zhao, Gustavo M Dalpian, Zhi Wang, and Alex Zunger. Polymorphous nature of cubic halide perovskites. *Physical Review B*, 101(15):155137, 2020. pages 80, 82, 88

[14] Asma A Medjahed, Tao Zhou, Juan Camilo Alvarez Quiceno, Pia Dally, Pascal Pochet, Tobias U Schülli, David Djurado, Peter Reiss, and Stéphanie Pouget. Microstructure of methylammonium lead iodide perovskite thin films: A comprehensive study of the strain and texture. *Advanced Energy Materials*, 12(19):2103627, 2022. pages 8, 83

[15] Wei Liu, Yang Liu, Ju Wang, Cuncun Wu, Congyue Liu, Lixin Xiao, Zhijian Chen, Shufeng Wang, and Qihuang Gong. Twin Domains in Organometallic Halide Perovskite Thin-Films. *Crystals*, 8(5):216, May 2018. Number: 5 Publisher: Multidisciplinary Digital Publishing Institute. pages 83

[16] Marek Szafrański and Andrzej Katrusiak. Mechanism of Pressure-Induced Phase Transitions, Amorphization, and Absorption-Edge Shift in Photovoltaic Methylammonium Lead Iodide. *The Journal of Physical Chemistry Letters*, 7(17):3458–3466, September 2016. pages 83

[17] Joachim Breternitz, Michael Tovar, and Susan Schorr. Twinning in $MAPbI_3$ at room temperature uncovered through Laue neutron diffraction. *Scientific Reports*, 10(1):16613, October 2020. Number: 1 Publisher: Nature Publishing Group. pages 83

[18] Mathias Uller Rothmann, Wei Li, Ye Zhu, Udo Bach, Leone Spiccia, Joanne Etheridge, and Yi-Bing Cheng. Direct observation of intrinsic twin domains in tetragonal $CH_3NH_3PbI_3$. *Nature Communications*, 8:14547, February 2017. pages 83

[19] José A Flores-Livas, Daniele Tomerini, Maximilian Amsler, Ariadni Boziki, Ursula Rothlisberger, and Stefan Goedecker. Emergence of hidden phases of methylammonium lead iodide $CH_3NH_3PbI_3$ upon compression. *Physical Review Materials*, 2(8):085201, 2018. pages 9, 89

Chapter 4

Journey into the Void: Exploring Vacancies in MAPbI_3

> Crystals are like people, it is the defects in them which tend to make them interesting.
>
> Colin Humphreys

In this chapter, we present a comprehensive investigation of vacancy defects in MAPbI_3 and provide detailed findings. We begin by discussing defect formation energy calculations for the tetragonal and Pseudo-Tetragonal-3D forms. We then proceed to analyze the results of positron annihilation lifetime calculations, comparing them with relevant literature. Furthermore, we include electron-positron charge density maps, allowing for a visual representation of the charge distribution. To enhance our understanding, we also present the results of the Voronoi volume analysis, which correlates with the findings from the positron annihilation lifetime measurements. Finally, we conclude this chapter by summarizing the key outcomes of our study.

4.1 Defect Formation Energy of vacancy defects

The defect formation energy, serving as an indicator of the stability and viability of the defect formation process, has been computed. The details for the calculation of defect formation energy are given in Section 2.3.2. These are calculated based on the chemical potential in different regions of Pb-poor, Pb-medium and Pb-rich conditions 2.3.1. The different regions are depicted in the thermodynamic stability diagram presented in Figure 4.1.

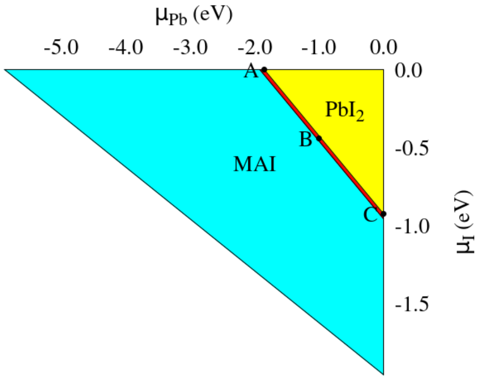

Figure 4.1: The thermodynamic stability diagram of MAPbI$_3$ with the different regions labelled based on their chemical potential: Pb-poor (A), Pb-medium (B), and Pb-rich (C) conditions.

4.1.1 Tetragonal polymorphs of MAPbI$_3$

To assess the defect formation energies in the five distinct polymorphs of the tetragonal form in MAPbI$_3$ [1], we specifically focused on calculating the energies associated with the V^{-}_{MA} and V^{2-}_{Pb} defects. The notations depict the charge of the vacancy in superscript and vacancy type in subscript. These specific defects result in the formation of a negative open void that facilitates the localization and trapping of the positron and result in a meaningful positron annihilation lifetime result. In contrast, the positron does not exhibit any interaction with the positively charged defects rendering the positron annihilation calculation on them inconsequential [2]. Therefore, conducting positron annihilation calculations on positively charged defects would be futile as they do not contribute to the annihilation process.

For the defect formation energy calculations, we utilized an 8 formula unit supercell for each of the tetragonal polymorphs as described in Tong et al. [1]. The calculations were performed using the gamma K-point sampling.

The results of the defect formation energy calculations for the Pb-rich, medium, and poor conditions in the tetragonal polymorphs are presented in Figure 4.2, and the corresponding equation used for calculating the defect formation energy is given by Equation 2.24. The plots illustrate the change in defect formation energy with respect to the Fermi level. The values for V_{MA}^{-} and V_{Pb}^{2-} are depicted in red and blue, respectively. The obtained values align with the trend reported in the literature [3, 4].

We remind that the slope of the curves in Figure 4.2 reflect the charge state of the respective defects. The slope of the V_{Pb}^{2-} curve is steeper compared to V_{MA}^{-}. This is because of the greater magnitude of the negative charge carried by V_{Pb}^{2-}, resulting in a more pronounced effect on the defect formation energy. The defect formation energy of the V_{MA}^{-} vacancy defect is consistently higher than that of V_{Pb}^{2-} in all three conditions. This could be due to the electrostatic interaction between the MA^{+} molecular cation and the inorganic framework.

The defect formation energy of V_{Pb}^{2-} is higher in lead-rich conditions. Pb-rich condition implies that the chemical potential of Pb is relatively low. Even if the vacancies are formed, there might be a higher probability of vacancies being filled by neighboring atoms due to the abundance of available atoms. Therefore, in Pb-rich conditions, the defect formation energy of V_{Pb}^{2-} increases.

An interesting observation in the defect formation energy plot is that the charge transition levels are not the same in the different polymorphs. In Figure 4.3, the defect formation energy is represented differently, showcasing the relationship between the defect formation energy and the region on the x-axis, with the Fermi level positioned at the Valence Band Minimum (VBM). The letters A, B and C correspond to the Pb poor, medium and rich conditions. The range of difference in the DFE for the different polymorphs is within 0.6 eV. V_{MA}^{-} has a lower formation energy in Tetra C polymorph while V_{Pb}^{2-} has a lower formation energy in Tetra D polymorph.

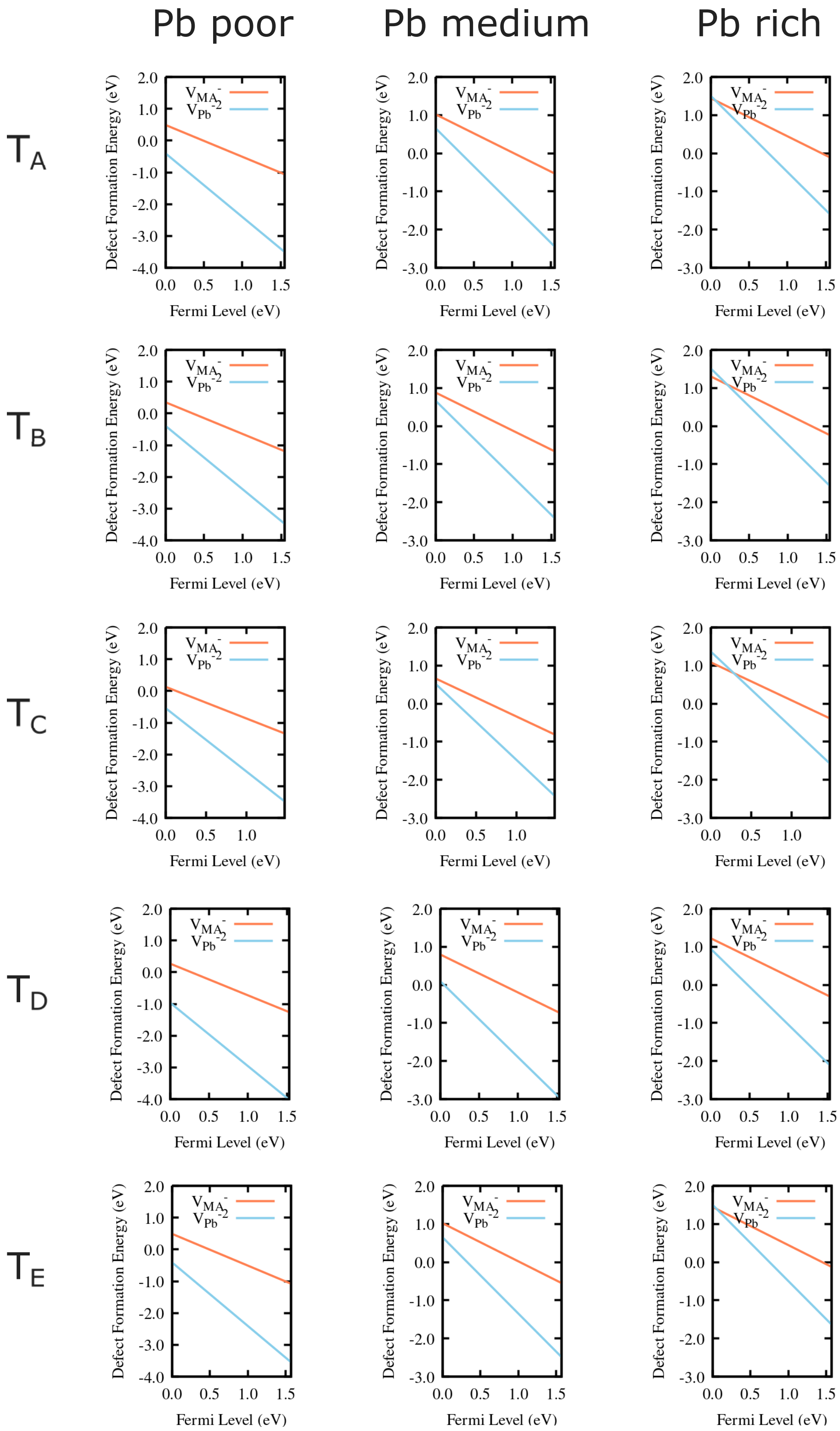

Figure 4.2: Plots illustrating the relationship between defect formation energy and Fermi level for the various tetragonal polymorphs [1]. The analysis covers three distinct scenarios, namely Pb-poor, Pb-medium, and Pb-rich conditions.

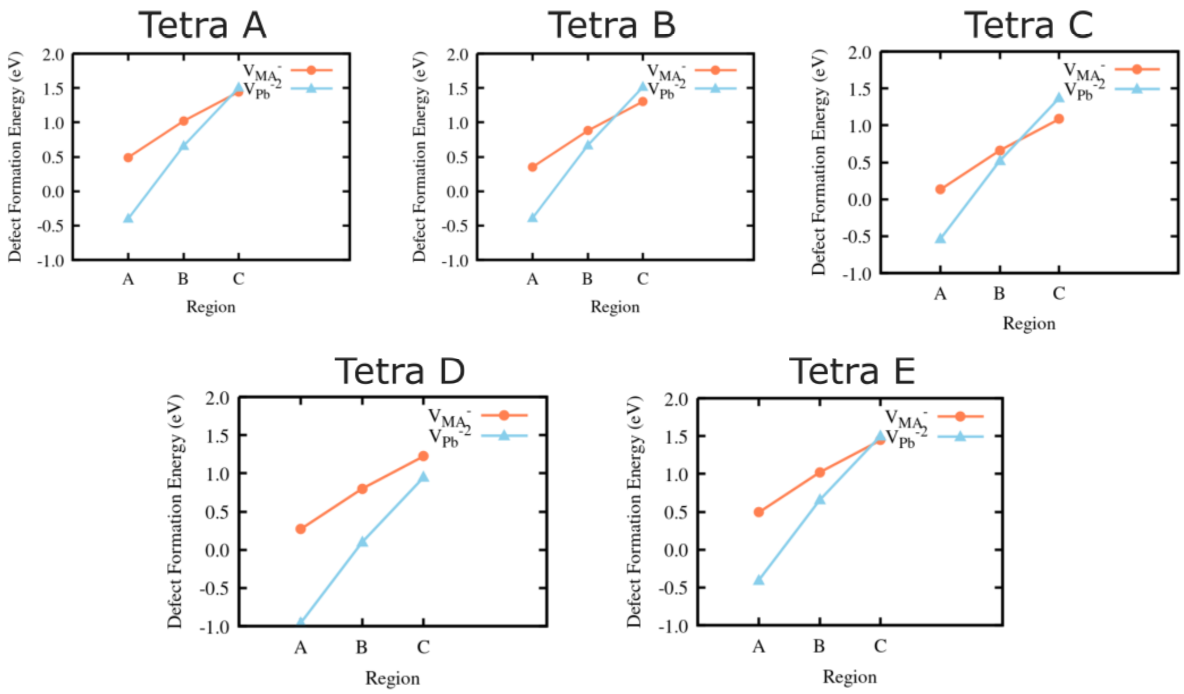

Figure 4.3: Plots illustrating the relationship between defect formation energy and the different regions (A=Pb poor, B= Pb medium and C= Pb rich) for the various tetragonal polymorphs [1].

4.1.2 Pseudo-Tetragonal-3D

The defect formation energy was also calculated for the Pseudo-Tetragonal-3D form of the material. In this calculation, the defect formation energy was determined for the MA, Pb, and the three iodine vacancies in MAPbI$_3$ corresponding to the neutral charge state. The reason for considering these specific atoms is that they have different types of hydrogen bonding connections with the inorganic cage: I^a does not exhibit any hydrogen bonding with the MA molecule, I^b forms two different hydrogen bonds with MA molecules, and I^c forms a single hydrogen bond with one MA molecule. Upon relaxation of the single I vacancies added to the pristine system, it was observed that I^a, where no bond was broken, had a slightly lower formation energy compared to I^b and I^c. The formation of I^b and I^c vacancies led to the disruption of their original hydrogen bonds. However, in the case of I^b, an additional reconstruction of MA molecular hydrogen bonding through rotation was observed. The corresponding plots illustrating the defect formation energies are shown in Figure 4.4. It can be observed that the defect formation energies for these single vacancy defects range between 0.5-2.5 eV. These values are close to the values obtained by Yin et al. [4] for the cubic phase of MAPbI$_3$ using the GGA functional, but they do not take into account the van-der-Waals contribution or the various iodines.

In Pb-poor conditions, the defect formation energy for iodine vacancies was found to be high. Although there was a slight difference in the formation energy among the three vacancy defects, it was not significantly large. According to the graph, the formation energy for MA and Pb vacancies should be low in Pb-poor conditions, indicating a higher likelihood of their formation. Conversely, in Pb-rich conditions, the formation of iodine vacancy defects should be favored.

For complex vacancies, MAI and PbI$_2$ were considered since they are the thermal decomposition products of MAPbI$_3$. Only MAI with iodine of type a and c was considered, while type b was excluded due to its bi-coordination with two MA molecules and the observation of MA rotation to restore the broken hydrogen bond in the case of I^b vacancy. The formation energies of these vacancy complexes under intermediate iodine chemical potential conditions were found to be lower than those of single vacancies. Even with different conditions, the formation energy exhibits minimal variation and remains within the range of 1-1.5 eV.

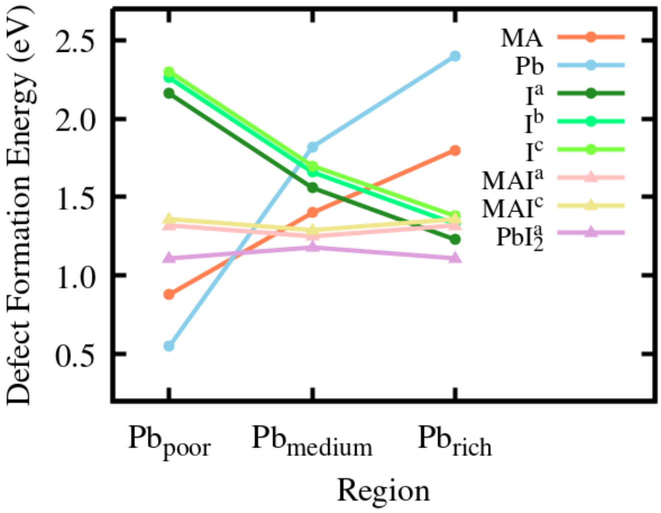

Figure 4.4: Plot of the defect formation energy for single vacancy defects (V$_{MA}^-$, V$_{Pb}^{-2}$, V$_I^+$) and complex vacancy defects (V$_{MAI}$, V$_{PbI_2}$) in Pb-poor, medium, and rich conditions.

Furthermore, the binding energy, which is calculated as the difference between the vacancy complex and its individual constituents, was determined and is presented in Figure 4.5. The results show that for all three cases tested, namely V$_{MAI^a}$, V$_{MAI^c}$, and V$_{PbI_2^a}$, the binding energy is positive. This indicates that these vacancy complexes are stable. PbI$_2$ exhibits a stronger binding energy compared to the MAI counterparts, primarily due to its higher charge and the resulting enhanced electrostatic interactions.

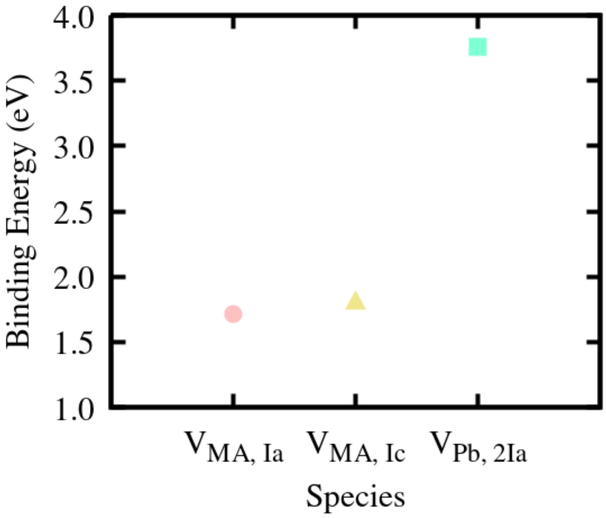

Figure 4.5: Plots for the binding energy of complex defects in deformation phases of MAPbI$_3$: MAI and PbI$_2$.

4.2 Positron annihilation lifetime calculations

Following the defect formation energy calculations, we present the results of the positron annihilation lifetime calculations conducted for $\mathrm{MAPbI_3}$. The positron annihilation lifetime calculations provide valuable insights into the behavior of positrons in the material and offer significant information about defects and their impact on the overall system. The obtained results are discussed in detail in the following subsections.

4.2.1 Electron-positron exchange correlation

To begin the investigation, a series of tests were conducted to examine the impact of modifying the alpha parameter on the positron annihilation lifetime. The resulting plot in given in Figure 2.13. Both the ATSUP and Quantum Espresso modes were employed for this purpose, as elaborated in 2.1.2. The obtained plot, depicted in Figure 4.6, showcases the positron annihilation lifetime for Teragonal A $\mathrm{MAPbI_3}$ on the y-axis and the alpha parameter on the x-axis. The two lines, colored blue and green, correspond to the positron annihilation lifetime values obtained using ATSUP with either an atomic superposition of atomic densities, or the Kohn-Sham self-consistent electron density for the solid (Quantum Espresso). It is evident that the positron annihilation lifetime exhibits a linear increase with the alpha parameter in both cases, with the latter demonstrating a slightly steeper slope. Also, the positron annihilation lifetime calculated using the latter stays, in general, higher than that obtained using the former one. Moreover, the obtained range of values underscore the significance of the alpha parameter as an adjustable factor. The study conducted by Barbiellini et al. [5, 6] put forward a recommended value of 0.22 for the alpha parameter which has been utilized in previous computations on $\mathrm{MAPbI_3}$ as well [7].

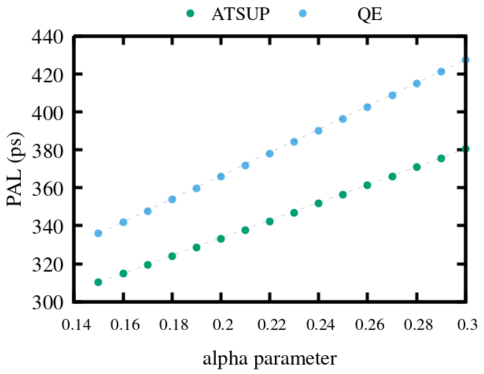

Figure 4.6: Plot depicting the correlation between the positron annihilation lifetime in tetragonal $MAPbI_3$ (A polymorph) and the Alpha Parameter 2.13

4.2.2 Positron Annihilation Lifetime results for pristine MAPbI$_3$ systems

The positron annihilation lifetime was computed for all phases of MAPbI$_3$, including the polymorphous structure. These results are illustrated in Figure 4.7 and the corresponding value are given in Table 4.1. The figure reveals a correlation between the positron annihilation lifetime and the volume variation with temperature. The abbreviations O, T, C, and P correspond to the orthorhombic, tetragonal, monomorphous cubic, and polymorphous cubic phases, respectively. The unit cells of the O, T and C phases along with the 32 formula unit polymorphous system were used to obtain the lifetime results.

Among these phases, the low-temperature orthorhombic phase, characterized by the smallest volume, exhibits the lowest positron annihilation lifetime. The calculated value for this phase is 352 ps. The tetragonal polymorphs, with similar volumes, display nearly identical positron annihilation lifetimes between 376 and 379 ps. In contrast, the high-temperature cubic phase, possessing the largest equilibrium volume, demonstrates the highest positron annihilation lifetime of 382 ps. Similarly, its polymorphous counterpart exhibits a comparable positron annihilation lifetime at 383 ps.

Based on the plot of the lifetimes, it appears evident that there is a distinct disparity in the positron annihilation lifetime between the orthorhombic phase and the tetragonal polymorphs. However, the variation in the lifetime values between these tetragonal polymorphs, as well as with the cubic phase, can hardly be appreciated. This observation suggests that the lattice structure plays a significant role in influencing the positron annihilation lifetime, particularly between different crystal structures, while the differences within polymorphs of the same crystal structure may not be as pronounced.

Table 4.1: Table for the values of Positron Annihilation Lifetime for the different phases using both a superposition of atomic densities and a fully self-consistent charge density of $MAPbI_3$.

Positron State	PAL (ps)	
	ATSUP	Quantum Espresso
Orthorhombic (O)	324.07	352.53
Tetragonal (T_A)	342.34	377.97
Tetragonal (T_B)	342.45	378.46
Tetragonal (T_C)	341.38	376.40
Tetragonal (T_D)	342.92	379.29
Tetragonal (T_E)	342.22	377.00
Monomorphous Cubic (C)	348.77	382.83
Polymorphous Cubic (P)	348.57	383.41

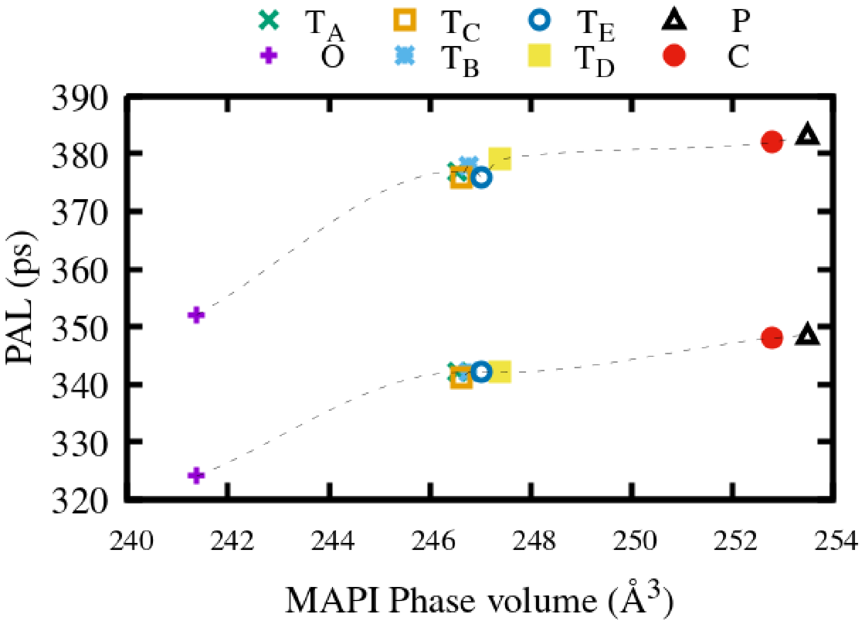

Figure 4.7: Plot for the correlation between positron annihilation lifetime and phase volume of $MAPbI_3$ for the different phases of $MAPbI_3$: Orthorhombic (O), Tetragonal (T) and Cubic (C:monomorphous cubic, P: polymorphous cubic). The lower and upper values correspond to the use of a superposition of atomic densities (ATSUP) and a fully self-consistent charge density (Quantum Espresso), respectively, for the PAL calculation.

4.2.3 PAL results for defective systems

Following the positron annihilation calculations on pristine systems, further calculations were conducted on systems containing single defects of V_{Pb}^{2-} and V_{MA}^{-}. To ensure consistency with previous studies, the 2×2×1 (192 atoms) supercell of the tetragonal phase (A polymorph) was utilized for these calculations. The obtained results are presented in Table 4.2. The values of positron annihilation lifetime computed using ATSUP, previously known as MIKA, is comparable to literature values [7].

The positron annihilation lifetime is significantly influenced by the lattice structure of a material. The specific atomic-level lattice structure achieved depends on the relaxation parameters utilized in the calculation, including the functional employed. In the case of ABINIT calculations, GGA functional along with PAW pseudopotentials were employed, while in our study, we used a GGA functional (optB86b+vdW) that includes van-der-Waals interactions along with ultrasoft (US) pseudopotentials. Van-der-Waals forces are vital in order to take into account the interaction between the organic and inorganic parts [8, 9, 10]. Moreover, the electron-positron correlation functional used in the ABINIT calculations was parametrized by Boronski and Nieminen which is designed for use with LDA [11], whereas we consistently applied the Arponen and Pajanne parameterization (also used for MIKA calculations). These discrepancies in the choice of methodology may account for the observed differences in the obtained positron annihilation lifetime results.

Table 4.2: : Table for the comparison of the positron annihilation lifetime calculation results using self-consistent electron densities for the tetragonal phase of $MAPbI_3$ with literature.

Positron State	PAL (ps)			
(Tetragonal)	ATSUP	MIKA [7]	QE	ABINIT [7]
Perfect Lattice	342	353	378	342
V_{Pb}^{2-}	347	369	398	360
V_{MA}^{-}	374	401	568	414

4.2.4 Effect of supercell size on the Positron Annihilation Lifetime

To investigate the impact of supercell size on positron annihilation lifetime (PAL), we conducted additional calculations using a smaller supercell consisting of 96 atoms. A comparison of the results obtained from the two supercell sizes is presented in Table 4.3.

In the perfect supercells, no difference in the lifetime was observed. However, when comparing the positron annihilation lifetime in the two defective states, namely the V_{Pb}^{2-} vacancy and V_{MA}^{-} vacancy, there were noticeable differences. The lifetime for the V_{Pb}^{2-} vacancy exhibited a small increase of 6 ps, whereas that for the V_{MA}^{-} vacancy showed a larger increase of 20 ps. However, in both cases, the lifetime was found to be larger in the larger supercell in the presence of defects. The underlying reason for this behavior could be attributed to the relaxation of the atoms around the defect, which could depend on the supercell size, although without any definite trend.

Table 4.3: : Table for the comparison of the positron annihilation lifetime calculation results for the tetragonal phase of $MAPbI_3$ with literature.

Positron State (Tetragonal A polymorph)	PAL (ps)	
	96 atom	192 atom
Perfect Lattice	378	378
V_{Pb}^{2-}	392	398
V_{MA}^{-}	548	568

4.3 Electron-Positron Charge Density

Visualizing the charge densities of electrons and positrons can provide valuable insights for understanding the electron-positron interactions. For this, electron and positron charge densities can be generated with Quantum Espresso [12] and ATSUP [13], respectively. However, in the limit of the diluted positron, the positron density is rather low when compared to the electron density in the system. But for the sake of visualization in 3D using Xcrysden, they need to be treated in the same way. Therefore, appropriate scaling factor is applied to serve the purpose of enhancing the visualization of the positron density. By employing a negative scaling factor, we visualize the electron and positron densities with contrasting signs, facilitating a straightforward comparison of their distributions in a system. The isovalue used for visualization is 0.52 which is less than two-thirds of the maximum value 0.93.

4.3.0.1 Pristine tetragonal systems

The densities of the pristine tetragonal polymorphs were visualized first. The 3D representations for these densities are given in Figure 4.8. The electron density is depicted in red and the positron density in blue. The scaling factor for each of the tetragonal polymorphs is provided in the figure.

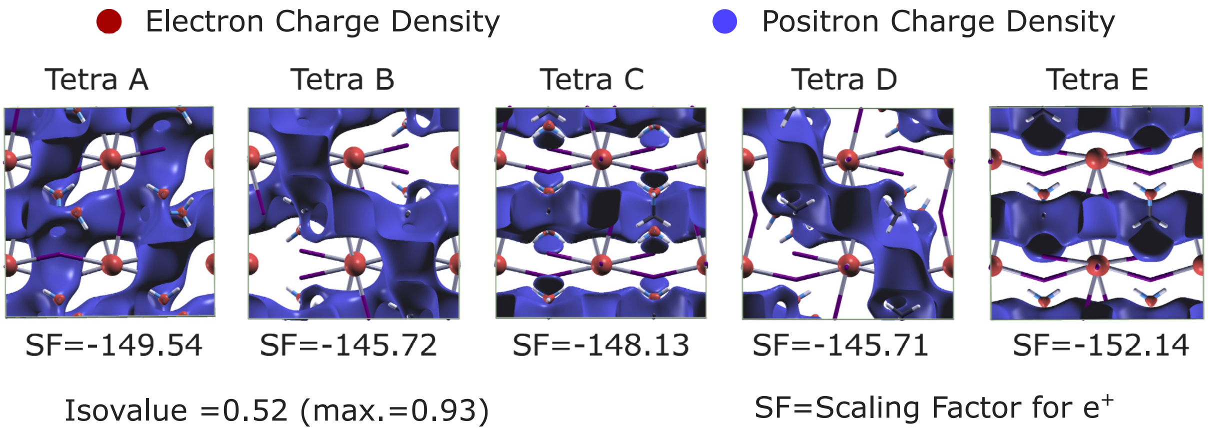

Figure 4.8: 3D representations of the electron-positron charge densities in the pristine tetragonal polymorphs. The electron density is depicted in red and the positron density in blue. The positron density is multiplied by a scaling factor (SF) so that its maximum absolute value equals the maximum of the electron density, and the sign is the opposite. The isosurfaces for densities equal to 56% of their maximum are shown.

It can be seen that the electron density is localized on the Pb and N atoms while the positron density is delocalized in the voids. For I, the electronic density is even more strongly localised than Pb or N, but it is not visible in the figure because the choice of isovalue is such that is closer to iodine atoms than the size of the sphere used to represent them. The positron density exhibits a notable concentration towards the carbon (C) side of the MA molecule, while it is comparatively lower or absent towards the nitrogen (N) side. Another observation is that the positron density has a two-dimentional lamellar appearence in at least some of the tetragonal systems.

4.3.0.2 Defective tetragonal systems

Here, we present the densities for the V_{MA}^{-} and V_{Pb}^{2-} defects in the tetragonal polymorphs. Due to the introduction of defects, a void is created, attracting and trapping positrons within it. This phenomenon of positron trapping within the vacancy can be observed in Figure 4.9.

The binding energies with respect to the pristine counterpart following the equation 2.11 are also presented alongside. The binding energy of the V_{MA}^{-} at a value of about 0.43 eV is observed to be greater than that of V_{Pb}^{2-} at an average of about 0.29 eV. A higher binding energy of the positron in the V_{MA}^{-} suggests a stronger interaction between the positron and the surrounding atoms or lattice in the V_{MA}^{-}, making it more difficult for the positron to escape or annihilate with an electron. This indicates that the positron is more localized and confined within the V_{MA}^{-}, resulting in a higher positron density in that region. The longer lifetime of the positron, as indicated by the value of the positron annihilation lifetime in Figure 4.9, further supports this notion. The longer lifetime suggests that the positron spends a significant amount of time within the V_{MA}^{-} before eventually annihilating with an electron.

In the case of vacancies, a much smaller scaling factor is used for visualization compared to that for pristine systems. This is because the positron density is concentrated at the defect site, while in pristine systems, it was delocalized.

	T$_A$	T$_B$	T$_C$	T$_D$	T$_E$
PAL (ps)	392	394	398	393	397
SF	-16.67	-16.82	-15.69	-17.30	-15.62
E$_b$ (eV)	0.27	0.28	0.32	0.25	0.31

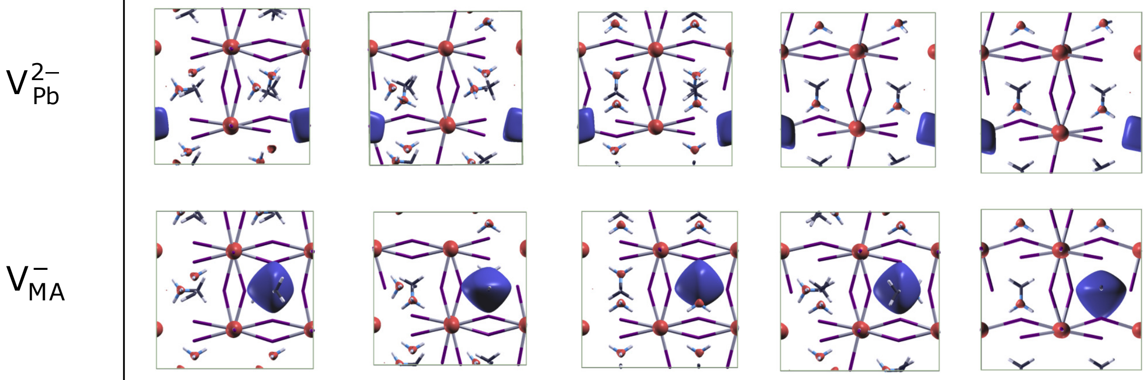

	T$_A$	T$_B$	T$_C$	T$_D$	T$_E$
PAL (ps)	548	548	550	544	551
SF	-17.93	-18.02	-17.92	-17.83	-17.73
E$_b$ (eV)	0.43	0.43	0.43	0.42	0.44

Figure 4.9: 3D representations of the charge densities in the tetragonal polymorphs of MAPbI$_3$ with V$_{MA}^{-}$ and V$_{Pb}^{2-}$ single defects. The binding energies are given alongside in eV. The isosurfaces for densities are taken equal to 56% of their maximum value.

A similar electron-positron density map was obtained for the 2×2×1 supercell of the tetragonal MAPbI$_3$ (A polymorph), along with the corresponding single defects of V$_{MA}^{-}$ and V$_{Pb}^{2-}$. On the left side of the Figure 4.10, the pristine system exhibits a delocalized positron density. This is because the positron is free to explore the empty space within the material before undergoing annihilation with an electron. As a result, the positron density is spread out and not confined to specific regions. Next to it, the same systems are displayed, but with single defects V$_{MA}^{-}$ and V$_{Pb}^{2-}$. In these systems, the positron density appears significantly more localized. This is due to the presence of the vacancy defects, which act as trapping sites for the positron. Consequently, the positron becomes confined within these vacancy defects, leading to a higher density in those specific regions. Smaller value of the scaling factor is an indirect measure of the localization of the positron, which is clear from the Figure 4.10.

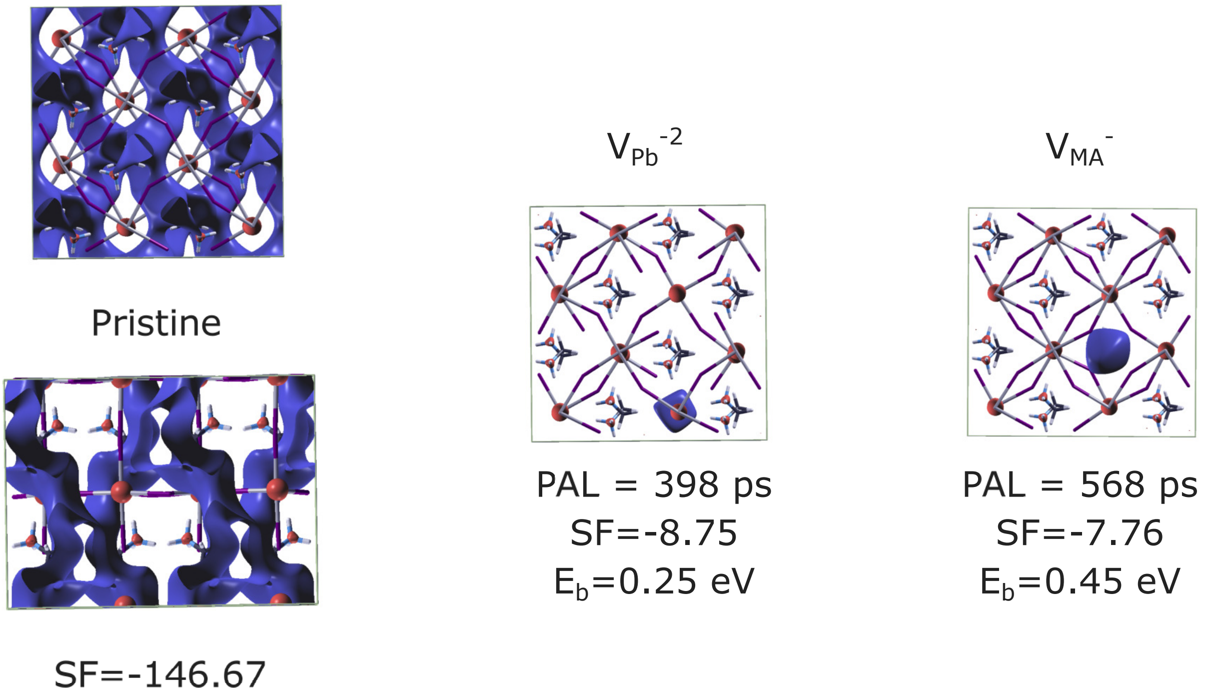

Figure 4.10: The electron-positron charge density illustration for tetragonal MAPbI$_3$ (A polymorph) in the 2×2×1 supercell without vacancy (left), with Pb^{+2} vacancy (centre) and MA$^-$ vacancy (right). The isosurfaces for densities are equal to 56% of their maximum value.

4.3.0.3 Polymorphous system

The electron-positron density maps were generated for the polymorphous form of MAPbI$_3$. In order to provide a visual comparison, the monomorphous cubic form consisting of 384 atoms($2\sqrt{2}\times2\sqrt{2}\times4$) was also included. This is given in Figure 4.11).

In the case of the monomorphous form, a delocalized positron density is observed. Conversely, in the polymorphous form, the positron density appears to be slightly less delocalized. This can be attributed to the local disorder within the system, which leads to a slight localization of the positron. The binding energy of the positron with the lattice in this polymorphous cubic system, relative to the monomorphous cubic system, is 0.02 eV.

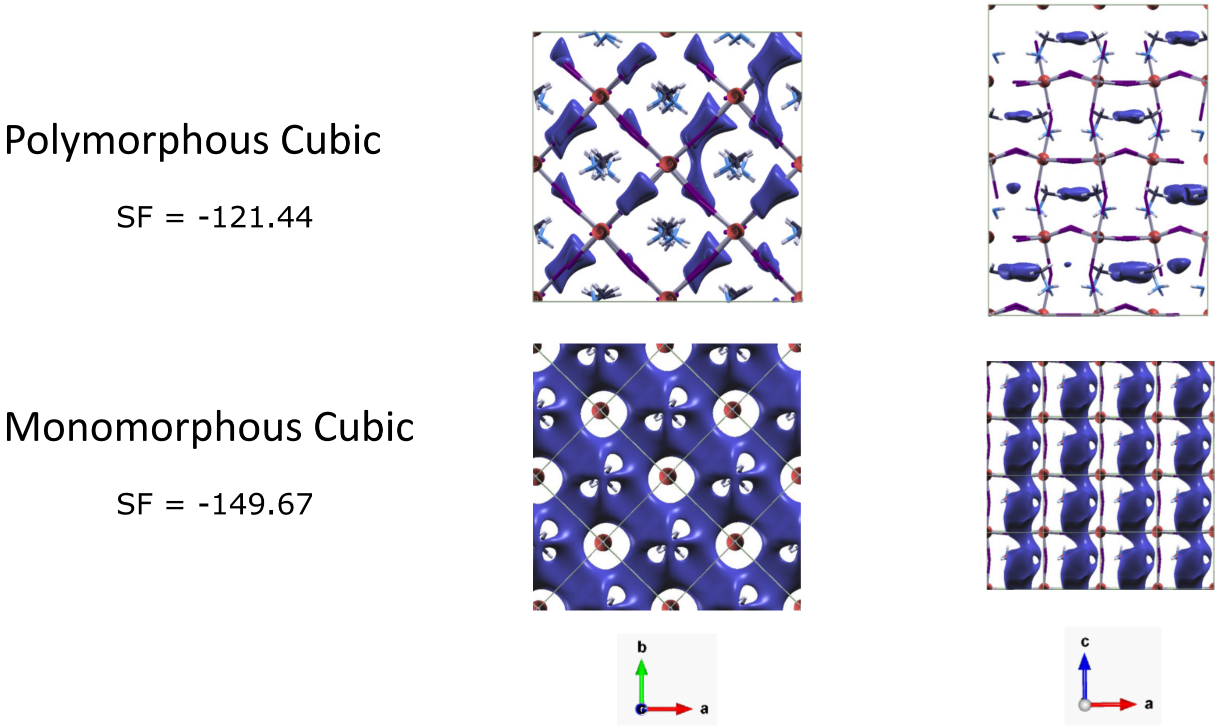

Figure 4.11: The electron-positron charge density map for the polymorphous and monomorphous cubic $MAPbI_3$. The isosurfaces for densities are equal to 56% of their maximum value.

4.4 Voronoi volume analysis

We have discussed the calculation of positron annihilation lifetimes and the associated electron and positron charge density maps. Now, we will discuss a qualitative approach that could enable us to estimate the size of the open volume based on the PAL, or vice versa.

4.4.1 Void size and lifetime relationship

As mentioned in section 2.3.3, the positron annihilation lifetime τ is expected to be a monotonically increasing function of the size of the vacancy or open volume defect [14]. But the relationship could be complex. According to previous studies, between the positron annihilation lifetime and vacancy cluster size, a direct proportional relation is observed for Si [15]. On the contrary, this does not hold true for GaAs, for which it is reported that the size dependency is not linear [16].

To verify the relationship between the Voronoi volume and the positron annihilation lifetime for our system, we calculated the Voronoi volume for the tetragonal system (polymorph A). This was done for its pristine form, as well as with vacancies of Pb^{+2}, MA^{+}, H^{+}, C^{0} and N^{0}. The figure 4.12 depicts the plot of positron annihilation lifetime versus void volume in the tetragonal system, revealing a parabolic relationship between the positron annihilation lifetime and the Voronoi volume. The corresponding values are given in table 4.4.

Table 4.4: :Table for the positron annihilation lifetime and the corresponding Voronoi volume for MAPbI_3 tetragonal system with and without single vacancy defects

System	Positron annihilation lifetime (QE)	Voronoi volume
Perfect Lattice	378	22.5
V_{N}^{0}	378	22.9
V_{C}^{0}	379	24.3
V_{H}^{1-}	380	23.2
V_{Pb}^{2-}	398	30
V_{MA}^{-}	568	58

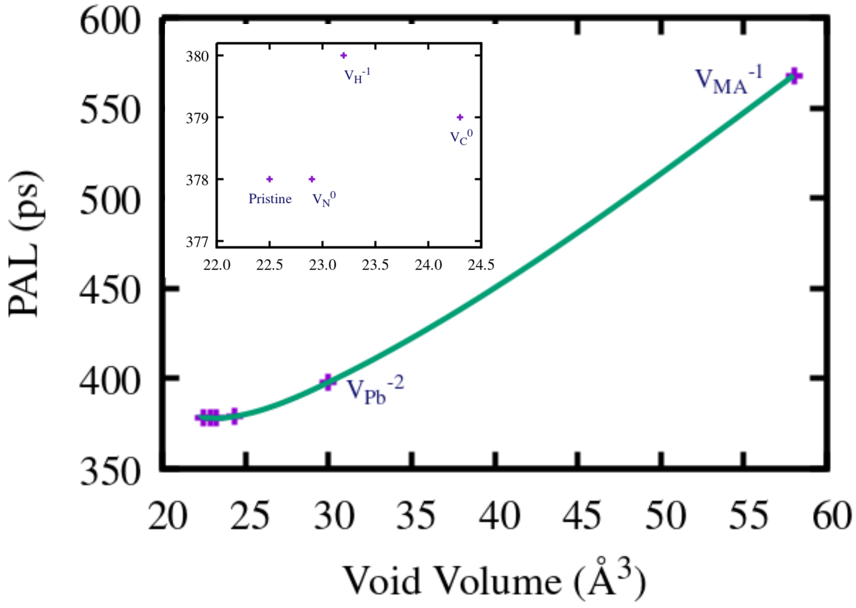

Figure 4.12: Positron annihilation lifetime versus void volume plot for tetragonal MAPbI$_3$ with and without single vacancy defects.

4.4.2 Voronoi volume in Tetragonal polymorphs

We compared the Voronoi volume in the different tetragonal polymorphs. Figure 4.13 presents the plot of void volume for each of the tetragonal unit cells (96 atoms) [1], with and without a defect. The MA (red) an Pb (blue) represent the voronoi volume of MA and Pb respectively in the pristine system; V^{-}_{MA} (orange) and V^{2-}_{Pb} (sky-blue) represent the defected system after relaxation. This plot facilitates a visual comparison of the Void Volume across different forms and highlights the effects of relaxation around defects on the Voronoi volume.

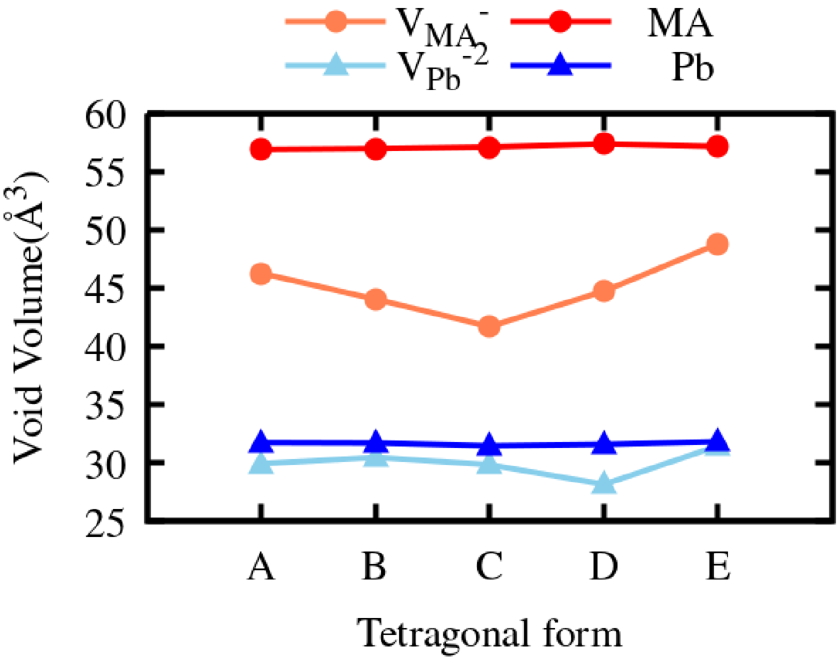

Figure 4.13: Plot of Void Volume for each of the tetragonal polymorphs, with and without a defect. The MA (red) an Pb (blue) represent the voronoi volume of MA and Pb respectively in the pristine system; V^{-}_{MA} (orange) and V^{2-}_{Pb} (skyblue) represent the defected system after relaxation.

Key observations regarding the plot are:

- The unrelaxed Voronoi volumes of MA and Pb remain consistent across the different tetragonal polymorphs.
- Following defect relaxation, the Voronoi volume shrinks as the neighboring atoms adjust their positions to fill the void created by the defect.

- The relaxation effect is more pronounced in the case of the MA vacancy compared to the Pb vacancy. The decrease in volume for Pb and MA vacancies is upto 4 and 16 Å^3, respectively. This difference can be attributed to the size disparity between MA and Pb, as Pb is smaller in size compared to the MA molecule.
- The relaxation is slightly different between the tetragonal polytypes with a range of upto 3.5 and 7 Å^3 for Pb and MA, respectively.

4.4.3 Void volume in Pseudo-Tetragonal-3D

For the Pseudo-Tetragonal-3D system, we calculated the void volumes for both single (MA, I, Pb) and complex vacancies (MAI, PbI_2) in a 32 formula unit supercell (384 atoms). These void volumes after relaxation are presented in plot 4.14.

The void volumes for single vacancies are found to be 29, 33 ± 1, and 58 Å^3 for Pb, I, and MA respectively. The high value obtained for MA is reasonable given its larger molecular size compared to Pb and I. Also, the MA void volume obtained for this system is about 20 Å^3 larger than the relaxed MA void in the tetragonal system, based on the relaxation of the nearest neighbor atoms. The volume of the MAI complex is comparable to that of MA, while PbI_2 void volume is obtained to be even lower at 41 Å^3 but greater than the single vacancies of Pb and I.

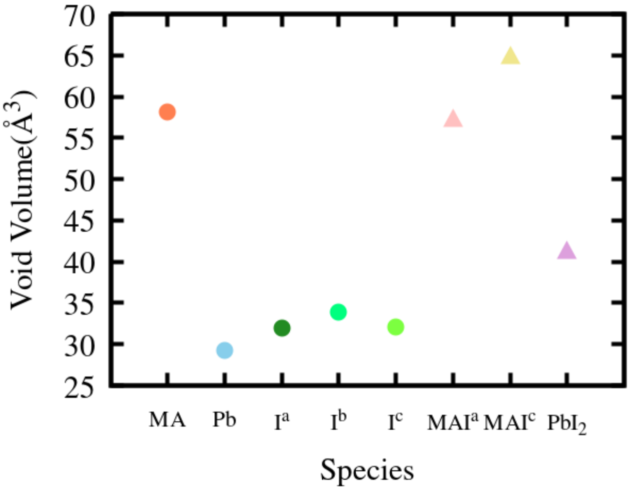

Figure 4.14: Plot for the void volume of different vacancies in the Pseudo-Tetragonal-3D form of $MAPbI_3$.

4.5 Hydrogen Vacancy

According to a previous report by Zhang et al. [17], hydrogen vacancies, particularly those associated with the nitrogen atom in the methylammonium (MA) molecule, can negatively impact the performance of MAPbI$_3$ by inducing non-radiative recombination. Ceratti et al. also report the contribution of hydrogen diffusion in MAPbI$_3$, leaving behind hydrogen vacancies [18]. Building upon these studies, we aimed to investigate the effect of a V$_H^-$ defect in the 2×2×1 supercell of tetragonal MAPbI$_3$ (polymorph A) on the positron annihilation lifetime. A low migration barrier between 1-2 eV is predicted for a proton [19].

Using Quantum Espresso for electronic relaxation and ATSUP for additional positron calculations, we obtained a positron annihilation lifetime of 380 ps for the system containing the V$_H^-$ vacancy. This value is slightly greater than the pristine form, which exhibited a lifetime of 378 ps, with a difference of 2 ps. It is challenging to draw conclusive distinctions between the pristine state and the V$_H^-$ vacancy solely based on this small difference in positron annihilation lifetime.

Furthermore, the binding energy associated with the V$_H^-$ vacancy was found to be small, measuring 0.12 eV. While this information provides some insight, it is not sufficient to unambiguously differentiate between the two states.

The electron and positron charge densities can be visualized in Figure 4.15, with the localized electron density represented in red and the slightly delocalized positron density shown in blue.

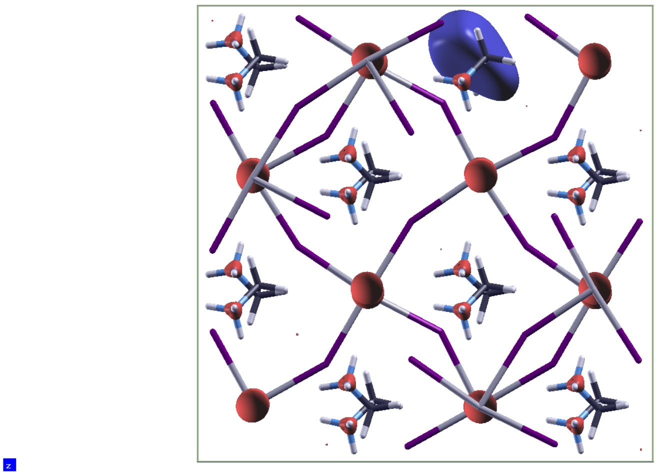

Figure 4.15: Visualization of the charge density of electron and positron in tetragonal MAPbI$_3$ with a vacancy of Hydrogen atom connected to the Nitrogen in Methylammonium molecule.

4.6 Conclusion

In summary, in this chapter we delved into an extensive examination of positron states within MAPbI$_3$ through the utilization of the ATSUP software. We accounted for electron density using both the atomic superposition method and density functional theory for the calculation of positron annihilation lifetime.

First we did the analysis of defect formation energy in different tetragonal polymorphs to find that V$_{Pb}^{2-}$ generally exhibits a lower formation energy than V$_{MA}^{-}$. Although minor variations in defect formation energy were observed among different tetragonal systems, this pattern emerged.

Hereafter, we explored the positron annihilation lifetime for different MAPbI$_3$ systems, both pristine and defective. Crystal structure variations was observed to change the positron annihilation lifetimes, while differences within polymorphs of the same crystal structure (tetragonal) were comparatively subtle. In defective systems, we observed a localization of positron density at the defective sites, whereas in pristine systems, the positron density remained delocalized in the bulk. We visualized these electron and positron densities using charge density maps. The values of the positron annihilation lifetime for Pb^{+2} vacancy is closer to the pristine system with a difference of 20 ps. Additionally, the analysis of positron binding energy in the polymorphous system indicated a marginal deviation of 0.02 eV from the monomorphous system, but the positron density seems to be more localized due to the local motifs in the charge density map.

We also conducted a comprehensive Voronoi volume analysis to establish a correlation between positron annihilation lifetime and void size in MAPbI$_3$. This analysis encompassed both tetragonal polymorphs and the Pseudo-Tetragonal-3D system. Lastly, we examined the intriguing case of hydrogen vacancies, which have recently garnered attention, and found that they yielded a positron annihilation lifetime closely resembling that of the pristine system.

REFERENCES

[1] Wen-Yi Tong, Jin-Zhu Zhao, and Philippe Ghosez. Missed ferroelectricity in methylammonium lead iodide. *npj Computational Materials*, 8(1):165, 2022. pages 10, 108, 110, 127

[2] Filip Tuomisto and Ilja Makkonen. Defect identification in semiconductors with positron annihilation: Experiment and theory. *Reviews of Modern Physics*, 85(4):1583, 2013. pages 108

[3] Daniele Meggiolaro, Silvia G Motti, Edoardo Mosconi, Alex J Barker, James Ball, Carlo Andrea Riccardo Perini, Felix Deschler, Annamaria Petrozza, and Filippo De Angelis. Iodine chemistry determines the defect tolerance of lead-halide perovskites. *Energy & Environmental Science*, 11(3):702–713, 2018. pages 109

[4] Wan-Jian Yin, Tingting Shi, and Yanfa Yan. Unusual defect physics in $\mathrm{CH_3NH_3PbI_3}$ perovskite solar cell absorber. *Applied Physics Letters*, 104(6):063903, 2014. pages 109, 112

[5] B Barbiellini, Martti J Puska, T Korhonen, A Harju, T Torsti, and Risto M Nieminen. Calculation of positron states and annihilation in solids: A density-gradient-correction scheme. *Physical Review B*, 53(24):16201, 1996. pages 114

[6] B Barbiellini, Martti J Puska, T Torsti, and Risto M Nieminen. Gradient correction for positron states in solids. *Physical Review B*, 51(11):7341, 1995. pages 114

[7] David J Keeble, Julia Wiktor, Sandeep K Pathak, Laurie J Phillips, Marcel Dickmann, Ken Durose, Henry J Snaith, and Werner Egger. Identification of lead vacancy defects in lead halide perovskites. *Nature Communications*, 12(1):5566, 2021. pages 114, 118

[8] Jingrui Li and Patrick Rinke. Atomic structure of metal-halide perovskites from first principles: The chicken-and-egg paradox of the organic-inorganic interaction. *Physical Review B*, 94(4):045201, 2016. pages 118

[9] David A Egger and Leeor Kronik. Role of dispersive interactions in determining structural properties of organic-inorganic halide perovskites: insights from first-principles calculations. *The journal of physical chemistry letters*, 5(15):2728–2733, 2014. pages 118

[10] Miguel A Perez-Osorio, Aurelie Champagne, Marios Zacharias, Gian-Marco Rignanese, and Feliciano Giustino. Van der waals interactions and anharmonicity in the lattice vibrations, dielectric constants,

effective charges, and infrared spectra of the organic-inorganic halide perovskite $CH_3NH_3PbI_3$. *The Journal of Physical Chemistry C*, 121(34):18459–18471, 2017. pages 118

[11] E Boroński and RM Nieminen. Electron-positron density-functional theory. *Physical Review B*, 34(6):3820, 1986. pages 118

[12] Paolo Giannozzi, Stefano Baroni, Nicola Bonini, Matteo Calandra, Roberto Car, Carlo Cavazzoni, Davide Ceresoli, Guido L Chiarotti, Matteo Cococcioni, Ismaila Dabo, et al. Quantum espresso: a modular and open-source software project for quantum simulations of materials. *Journal of physics: Condensed matter*, 21(39):395502, 2009. pages 120

[13] Tuomas Torsti, M Heiskanen, MJ Puska, and RM Nieminen. Mika: Multigrid-based program package for electronic structure calculations. *International journal of quantum chemistry*, 91(2):171–176, 2003. pages 120

[14] J de Vries. Positron lifetime technique with applications in materials science. 1987. pages 125

[15] W Fuhs, U Holzhauer, S Mantl, FW Richter, and R Sturm. Annihilation of positrons in electron-irradiated silicon crystals. *physica status solidi (b)*, 89(1):69–75, 1978. pages 125

[16] MJ Puska and C Corbel. Positron states in si and gaas. *Physical Review B*, 38(14):9874, 1988. pages 125

[17] Xie Zhang, Jimmy-Xuan Shen, Mark E Turiansky, and Chris G Van de Walle. Minimizing hydrogen vacancies to enable highly efficient hybrid perovskites. *Nature Materials*, 20(7):971–976, 2021. pages 129

[18] Davide Raffaele Ceratti, Arava Zohar, Roman Kozlov, Hao Dong, Gennady Uraltsev, Olga Girshevitz, Iddo Pinkas, Liat Avram, Gary Hodes, and David Cahen. Eppur si muove: proton diffusion in halide perovskite single crystals. *Advanced Materials*, 32(46):2002467, 2020. pages 129

[19] David A Egger, Leeor Kronik, and Andrew M Rappe. Theory of hydrogen migration in organic-inorganic halide perovskites. *Angewandte Chemie International Edition*, 54(42):12437–12441, 2015. pages 129

Chapter 5

Conclusion and Future perspectives

> Nothing in life is to be feared, it is only to be understood. Now is the time to understand more, so that we may fear less.
>
> Marie Salomea Skłodowska-Curie

This chapter outlines the general conclusion and discusses many interesting future research directions that expand on the findings and methodology described in this thesis. These directions have the potential to increase our understanding of the investigated systems while also opening up new avenues for study and discovery.

5.1 General Conclusion

In this thesis, we have studied the intricate structure, phase transformations and defects in the MAPbI$_3$ system, a pivotal material in the field of next-generation photovoltaic devices. First and foremost, we study the fundamental hydrogen-bonding scheme across all known phases to introduce new cubic and tetragonal phases. We identify a new-bonding scheme that is intermediate between the orthorhombic and tetragonal phases to obtain the Pseudo-tetragonal-3D system, having an energy lower than the monomorphous cubic system by $\sim$ 100 meV/fu. The energy landscape we have uncovered is complex and glassy-like.

Furthermore, we used NEB for studying the phase transformations. We have identified the methylammonium ion rotation as a reasonable mechanism to navigate between the phases at and above room temperature. The discovery of yet another tetragonal polytype closely resembling the Pseudo-Tetragonal-3D structure has significant implications, as it presents a low activation energy barrier, making the transformation between the two mentioned structures feasible at room temperature.

In the second part of our study, we delved into positron states within MAPbI$_3$ using the ATSUP software. Our research has provided valuable insights into defect formation energies, with a consistent pattern of lower formation energy for V$_{Pb}^{2-}$ compared to V$_{MA}^{-}$ across the various phases. We explored positron annihilation lifetimes for the various MAPbI$_3$ phases and observed changes in crystal structure affecting these lifetimes, both in pristine and defective systems. We provide the electron-positron charge densities to visualize the 2D-like delocalization of positron density in the bulk of the pristine system and its localization at defective sites. There is a correlation between positron annihilation lifetime and void size, as revealed by Voronoi volume analysis. Lastly, we end this part with the examination of hydrogen vacancies, a topic of recent interest, and found their positron annihilation lifetime to closely resemble that of the pristine system.

In summary, this research enhances our comprehension of MAPbI$_3$ at the atomic level and its phase transformations, which could contribute to the development of more efficient and stable photovoltaic devices. Our investigation of defects and positron states adds further details to the understanding of vacancy defects, offering potential pathways for further research and optimization.

5.2 Possible directions for future research

One intriguing area for future investigation involves the incorporation of dynamic disorder into our modeling framework using Molecular Dynamics (MD) simulations and simultaneous pair-distribution function (PDF) analysis with tools like PDFgui as discussed in this thesis [1, 2, 3]. Dynamic disorder takes into account the temporal fluctuations in the atomic positions with temperature. By coupling MD with PDF analysis, we can gain insights into how dynamic disorder influences the properties of MAPbI_3 perovskite [4, 5, 6].

Secondly, while our current method of calculating the activation energies for phase transformation has yielded valuable insights, it does not fully account for subtle differences in cell-dimensions between tetragonal and cubic supercells. A promising direction for future research is the implementation of the Variable Cell-NEB (VC-NEB) method, as exemplified in the USPEX software and supported by Quantum Espresso [7]. This approach has been successfully applied in the study of phase transformations in inorganic perovskites [8]. By adopting VC-NEB calculations, we can more accurately investigate phase transitions and better understand the underlying structural changes in our material.

In the course of our investigation, a striking resemblance between our Pseudo-Tetragonal-3D system with dipoles and the Shastry-Sutherland lattice spin model has been observed [9]. Further research is warranted to comprehensively explore and understand this similarity. Investigating the implications of this resemblance could potentially uncover novel physical phenomena and connections between seemingly disparate systems.

Another intriguing avenue for future exploration involves utilizing Positron Doppler Broadening calculations for obtaining the momentum distribution of electrons, and hence the S-parameter depending on the vacancy defect density in MAPbI_3 [10]. This technique offers unique insights into the defects within materials by examining the behavior of positrons, which are sensitive to the presence of vacancies and other structural imperfections. While there have been experimental investigations into this phenomenon [11, 12, 13] for MAPbI_3 perovskite, no computational reports have come to our attention as of now.

Lastly, it was observed that introduction of iodine vacancy defect in the Pseudo-Tetragonal-3D system resulted in the organic molecular orientation similar to those in the tetragonal system. Thus the role of Iodine vacancy to induce a phase transition in MAPbI_3 can be explored.

In conclusion, these prospective future study avenues carry the possibility of expanding our knowledge. By pursuing these avenues, we can address current limitations and uncover new dimensions within the domain of hybrid perovskites.

REFERENCES

[1] M Ibrahim Dar, Gwénolé Jacopin, Simone Meloni, Alessandro Mattoni, Neha Arora, Ariadni Boziki, Shaik Mohammed Zakeeruddin, Ursula Rothlisberger, and Michael Grätzel. Origin of unusual bandgap shift and dual emission in organic-inorganic lead halide perovskites. *Science advances*, 2(10):e1601156, 2016. pages 137

[2] A Mattoni, Alessio Filippetti, MI Saba, and P Delugas. Methylammonium rotational dynamics in lead halide perovskite by classical molecular dynamics: the role of temperature. *The Journal of Physical Chemistry C*, 119(30):17421–17428, 2015. pages 137

[3] CL Farrow, P Juhas, JW Liu, D Bryndin, ES Božin, J Bloch, Th Proffen, and SJL Billinge. Pdffit2 and pdfgui: computer programs for studying nanostructure in crystals. *Journal of Physics: Condensed Matter*, 19(33):335219, 2007. pages 137

[4] Xia Liang, Johan Klarbring, William J Baldwin, Zhenzhu Li, Gábor Csányi, and Aron Walsh. Structural dynamics descriptors for metal halide perovskites. *The Journal of Physical Chemistry C*, 2023. pages 137

[5] Claudio Quarti, Edoardo Mosconi, and Filippo De Angelis. Structural and electronic properties of organo-halide hybrid perovskites from ab initio molecular dynamics. *Physical Chemistry Chemical Physics*, 17(14):9394–9409, 2015. pages 137

[6] Ryosuke Jinnouchi, Jonathan Lahnsteiner, Ferenc Karsai, Georg Kresse, and Menno Bokdam. Phase transitions of hybrid perovskites simulated by machine-learning force fields trained on the fly with bayesian inference. *Physical review letters*, 122(22):225701, 2019. pages 137

[7] Guang-Rui Qian, Xiao Dong, Xiang-Feng Zhou, Yongjun Tian, Artem R Oganov, and Hui-Tian Wang. Variable cell nudged elastic band method for studying solid-solid structural phase transitions. *Computer Physics Communications*, 184(9):2111–2118, 2013. pages 137

[8] Sittichain Pramchu, Atchara Punya Jaroenjittichai, and Yongyut Laosiritaworn. Effects of bromine substitution for iodine on structural stability and phase transition of CsPbI_3. *Applied Surface Science*, 496:143593, 2019. pages 137

[9] B Sriram Shastry and Bill Sutherland. Exact ground state of a quantum mechanical antiferromagnet. *Physica B+ C*, 108(1-3):1069–1070, 1981. pages 137

[10] Ilja Makkonen, M Hakala, and Martti J Puska. Modeling the momentum distributions of annihilating electron-positron pairs in solids. *Physical Review B*, 73(3):035103, 2006. pages 137

[11] Joydeep Dhar, Sayantan Sil, Arka Dey, Dirtha Sanyal, and Partha Pratim Ray. Investigation of ion-mediated charge transport in methylammonium lead iodide perovskite. *The Journal of Physical Chemistry C*, 121(10):5515–5522, 2017. pages 137

[12] Joydeep Dhar, Sayantan Sil, Arka Dey, Partha Pratim Ray, and Dirtha Sanyal. Positron annihilation spectroscopic investigation on the origin of temperature-dependent electrical response in methylammonium lead iodide perovskite. *The Journal of Physical Chemistry Letters*, 8(8):1745–1751, 2017. pages 137

[13] Sayantan Sil, Sudipta Moshat, Partha Pratim Ray, Joydeep Dhar, and Dirtha Sanyal. Investigating the effect of applied bias on methylammonium lead iodide perovskite by electrical and positron annihilation spectroscopic studies. *Journal of Physics D: Applied Physics*, 54(46):465502, 2021. pages 137